

# FMCW-SAR SYSTEM FOR NEAR DISTANCE IMAGING APPLICATIONS

by

JUI WEN TING

A thesis submitted in partial fulfillment of the requirements for the degree of

Master of Science

in

Electromagnetics and Microwaves

Department of Electrical and Computer Engineering

University of Alberta

© JUI WEN TING, 2017

# Abstract

A combination of frequency-modulated continuous-wave (FMCW) technology with synthetic aperture radar (SAR) principles is a highly sought after method as it leads to a compact and cost effective high resolution near distance imaging system. However, there are a few design issues associated with FMCW radar systems that need to be addressed in order to design an optimal FMCW SAR imaging system. One of the limiting factors of FMCW radars is that the ramp signal modulates the received signal, which limits the minimum achievable range resolution. In addition, the voltage controlled oscillator (VCO) adds a certain degree of phase noise and nonlinearity to the transmitted signal that degrades the signal-to-noise ratio (SNR), range accuracy and image resolution. To resolve these issues, a multitude of hardware and software approaches have been proposed for the suppression of phase noise and nonlinearity of the transmitted signal. However, these approaches resolve only individual issues, limiting their applicability in the design of FMCW SAR imaging systems.

This work seeks to overcome the three design issues mentioned above through the development of simulation platforms, which has been shown to be well-suited for the comprehensive study of these effects. A signal processing procedure with system calibration methods to mitigate the effects of deramp, phase noise and nonlinearity of the VCO on the beat spectrum is proposed. Additionally, the effect of bandwidth, integration angle and phase noise of the received pulses on the SAR image resolution in both range and cross-range directions are comprehensively studied. To improve the range accuracy, different calibration methods are also comprehensively studied.

To demonstrate the effectiveness and versatility of the proposed signal processing procedure, an S-band FMCW radar system, using off-the-shelf components, is designed for near distance target imaging using linear and circular SAR techniques. The reconstructed images

show the improvement of image quality and accuracy in the target position. Finally, several avenues of further study and applications are suggested.

# Preface

This thesis is an original work by Jui wen Ting.

Chapter 4 of this thesis has been accepted for publication as: Jui wen Ting, Daniel Oloumi, and Rambabu Karumudi, “A Miniaturized Broadband Bow-Tie Antenna with Improved Cross-Polarization Performance,” *International Journal of Electronics and Communications Elsevier*, Dec. 2016. It is currently pending for satisfactory resolution of reviewer comments. I was the lead investigator, responsible for all major areas of simulation, fabrication, measurement and analysis, as well as manuscript composition. Daniel Oloumi assisted in manuscript edits. Dr. Rambabu Karumudi was the supervisory author on this project and was involved throughout the project in concept formation and manuscript composition.

D. Oloumi, Jui Wen Ting, K. Rambabu, ”Design of pulse characteristics for near-field UWB-SAR imaging,” *IEEE Trans. on Microwave Theory and Techniques*. vol.64, no.8, pp.2684-2693, Aug. 2016. I was responsible for parts of the manuscript composition and assisted in measurements.

# Acknowledgements

I would like to begin by expressing my sincere gratitude to my supervisor, Prof. Rambabu Karumudi, for his continuous support, patience and confidence in me. Through his training, mentorship and guidance, I have developed a greater understanding for radar imaging systems, electromagnetics and their related topics. I consider myself very fortunate in being able to work with such a considerate and encouraging professor like him.

I would also like to thank my committee members, Dr. Kambiz Moez and Dr. Yindi Jing, for their time and efforts in the process and for their insightful comments and suggestions.

Next, I am grateful to my colleagues, Kevin Chan and Daniel Oloumi for the collaborations and stimulating conversations. Despite their busy schedules, their support with some of the simulations and measurements has been phenomenal and very much appreciated.

Finally, I would like to thank my family - my mother, father and my amazing husband James for their support over the length of this endeavor, and through all its ups and downs. For this, I am truly grateful.

# Contents

<b>1</b>	<b>Introduction</b>	<b>1</b>
1.1	Motivation . . . . .	1
1.2	Background . . . . .	3
1.2.1	Radar . . . . .	3
1.2.2	FMCW Radar Principles and Architectures . . . . .	3
1.2.3	Mathematical Modelling . . . . .	5
1.2.4	Performance Metrics . . . . .	9
1.2.5	System Noise . . . . .	10
1.2.6	Phase Noise . . . . .	11
1.2.7	Frequency Selection . . . . .	16
1.2.8	Applications . . . . .	17
1.3	Thesis Contribution and Layout . . . . .	19
<b>2</b>	<b>ADS System Simulation</b>	<b>21</b>
2.1	Literature Review . . . . .	21
2.2	Ideal FMCW Radar System Simulation . . . . .	22
2.3	Ramp Circuit Parametrization . . . . .	24
2.4	VCO Parametrization . . . . .	27
2.5	PA Parametrization . . . . .	33
2.6	LNA Parametrization . . . . .	35
2.7	MIX Parametrization . . . . .	36

2.8	Summary of the Study . . . . .	38
2.9	Nonideal FMCW Radar System Simulation . . . . .	39
<b>3</b>	<b>Hardware Design</b>	<b>43</b>
3.1	Overview of FMCW Radar System . . . . .	43
3.2	Tx Signal Chain . . . . .	43
3.2.1	Ramp Circuit . . . . .	43
3.2.2	VCO . . . . .	45
3.2.3	LPF . . . . .	48
3.2.4	Coupler . . . . .	49
3.2.5	PA . . . . .	50
3.3	Rx Signal Chain . . . . .	50
3.3.1	LNA . . . . .	50
3.3.2	MIX . . . . .	51
3.3.3	Active LPF . . . . .	52
3.4	Baseband Signal Processing Unit . . . . .	53
3.4.1	ADC . . . . .	53
3.5	Overall System Specifications . . . . .	55
3.5.1	Time Domain Characterization . . . . .	55
<b>4</b>	<b>Antenna Design</b>	<b>60</b>
4.1	A Miniaturized Broadband Bow-Tie Antenna with Improved XP Performance	60
4.2	Introduction . . . . .	61
4.3	Antenna Design . . . . .	62
4.4	Results and Discussion . . . . .	66
4.4.1	Frequency Domain Characteristics . . . . .	66
4.4.2	Time Domain Characteristics . . . . .	69
4.5	Conclusion . . . . .	72

<b>5</b>	<b>Software Simulation</b>	<b>77</b>
5.1	Overview of Software Simulation . . . . .	77
5.2	Pre-processing . . . . .	78
5.2.1	Spectral Estimation . . . . .	78
5.2.2	Effect of Deramp Processing on Beat Spectrum . . . . .	79
5.2.3	Deconvolution Method . . . . .	84
5.2.4	Spectral Envelope and Impulsization Method . . . . .	84
5.3	Post-processing . . . . .	86
5.3.1	LSAR Image Reconstruction . . . . .	86
5.3.2	CSAR Image Reconstruction . . . . .	89
5.4	FMCW Radar Resolution . . . . .	90
5.4.1	Range Resolution . . . . .	91
5.4.2	Cross-Range Resolution . . . . .	92
<b>6</b>	<b>Measurement Results</b>	<b>97</b>
6.1	Calibration Of Target Location . . . . .	97
6.1.1	Removing Background Noise . . . . .	98
6.1.2	Removing Propagation Delay . . . . .	99
6.2	Reconstruction of SAR Image . . . . .	100
6.3	LSAR Image Reconstruction . . . . .	101
6.4	CSAR Image Reconstruction . . . . .	103
<b>7</b>	<b>Conclusion</b>	<b>105</b>
7.1	Summary . . . . .	105
7.2	Future Work . . . . .	106
<b>A</b>	<b>Datasheets</b>	<b>115</b>
A.1	VCO: ROS-3800-119+ . . . . .	115
A.2	PA: GALI-84+ . . . . .	116

A.3 PA: ZX60-8008E . . . . .	117
A.4 LNA: ZX60-6013E . . . . .	118
A.5 MIX: MCA1T-60LH . . . . .	119
A.6 ADC: USB-6351 . . . . .	120

# List of Symbols

$B$	Bandwidth
$c$	Speed of light
$c_r$	Chirp rate
$f_b$	Beat frequency
$R$	Target range
$T_{ramp}$	Sweep period
$\tau_d$	Time delay
$\omega_0$	Carrier frequency
$\epsilon$	Phase due to nonlinearity
$\psi$	Phase noise
$\Delta f_b$	Beat frequency resolution
$\Delta R$	Range resolution
$\Delta f$	Frequency offset from carrier frequency
$\Delta\omega$	Frequency offset from carrier frequency
$\mathcal{L}$	Phase noise
$\lambda$	Wavelength

# List of Acronyms

1-D	One-dimensional
2-D	Two-dimensional
3-D	Three-dimensional
ADC	Analog to digital converter
BPF	Band pass filter
CL	Conversion loss
CSAR	Circular synthetic aperture radar
CW	Continuous-wave
DANL	Displayed average noise level
dB	Decibels
DR	Dynamic range
EM	Electromagnetic
FFT	Fast Fourier transform
FMCW	Frequency-modulated continuous-wave
FSPL	Free space path loss
GBP	Global backprojection
GHz	Gigahertz ( $10^9$ Hz)
IID	Independent and identically distributed
IF	Intermediate frequency
ISM	Industrial, scientific and medical
kHz	Kilohertz ( $10^3$ Hz)
LO	Local oscillator
LPC	Linear prediction coefficient
LPF	Low pass filter

LNA	Low noise amplifier
LSAR	Linear synthetic aperture radar
m	Meter
MDS	Minimum detectable signal
MHz	Megahertz ( $10^6$ Hz)
MIX	Mixer
ms	Milliseconds ( $10^{-3}$ s)
mV	Millivolts ( $10^{-3}$ V)
NF	Noise figure
NFL	Noise floor level
ns	nanosecond ( $10^{-9}$ s)
P1dB	1 dB Gain compression
PA	Power amplifier
PSD	Power spectral density
RBW	Resolution bandwidth
RF	Radio frequency
Rx	Receiver
SA	Spectrum analyzer
SAR	Synthetic aperture radar
SNR	Signal to noise ratio
SSB	Single side band
Tx	Transmitter
$\mu$ s	Microsecond ( $10^{-6}$ s)
UWB	Ultra-wideband
VCO	Voltage controlled oscillator
VNA	Vector network analyzer

# List of Figures

1.1	Simplified block diagram of the homodyne FMCW radar system. . . . .	4
1.2	Linear sweep functions. . . . .	5
1.3	VCO phase noise illustration . . . . .	13
1.4	Feedback amplifier model for characterizing oscillator phase noise. . . . .	14
1.5	Lesson's phase noise model . . . . .	15
2.1	Ideal FMCW radar simulation . . . . .	23
2.2	Radar simulation with aperiodic sweep period . . . . .	24
2.3	Radar simulation with voltage noise in ramp signal . . . . .	25
2.4	Radar simulation with voltage clamp in ramp signal . . . . .	25
2.5	Radar simulation with non-instantaneous falling edge ramp signal . . . . .	26
2.6	Radar simulation with switch circuit . . . . .	26
2.7	Radar simulation with fluctuating power output chirp signal . . . . .	27
2.8	Radar simulation with phase noise added to a narrowband VCO . . . . .	29
2.9	Radar simulation with phase noise added to a wideband VCO (time) . . . . .	29
2.10	Radar simulation with phase noise added to a wideband VCO (frequency) . . . . .	29
2.11	MATLAB curve fitted plot . . . . .	31
2.12	Radar simulation with 2nd harmonics varied for the VCO . . . . .	31
2.13	Radar simulation with NF varied for the PA . . . . .	34
2.14	Radar simulation with P1dB varied for the PA . . . . .	34
2.15	Radar simulation with NF varied for the LNA . . . . .	36
2.16	Radar simulation with CL varied for the MIX . . . . .	37
2.17	Radar simulation with min. LO drive level varied for the MIX . . . . .	37
2.18	Nonideal FMCW radar simulation . . . . .	42
3.1	S-band FMCW hardware . . . . .	44

3.2	Ramp circuit schematic. . . . .	46
3.3	Ramp circuit PCB layout and photograph . . . . .	47
3.4	Ramp circuit measurement results. . . . .	47
3.5	VCO measurement results . . . . .	48
3.6	Stepped impedance LPF . . . . .	49
3.7	LPF simulation and measurement results . . . . .	49
3.8	Coupler measurement results. . . . .	49
3.9	PA measurement results . . . . .	50
3.10	LNA measurement result. . . . .	51
3.11	MIX measurement result. . . . .	51
3.12	Active LPF . . . . .	52
3.13	LabVIEW interface. . . . .	53
3.14	LabVIEW schematic. . . . .	54
3.15	Time domain system measurement results at various locations. . . . .	58
3.16	Time domain system measurement results to show changing frequency. . . . .	59
4.1	Antenna geometry . . . . .	63
4.2	H-plane RG simulation . . . . .	64
4.3	Photograph of the antenna . . . . .	64
4.4	Simulated and measured S11 and gain . . . . .	67
4.5	Current vector distribution at 5 GHz . . . . .	67
4.6	Current density distribution across frequency . . . . .	68
4.7	Conventional vs. modified simulated radiation patterns . . . . .	73
4.8	Slots vs. no-slots simulated radiation patterns . . . . .	73
4.9	Simulated vs. measured radiation patterns . . . . .	74
4.10	VNA setup . . . . .	74
4.11	VNA pulse measurements . . . . .	75
4.12	Antenna transfer functions . . . . .	75

4.13	CST antenna simulation . . . . .	76
5.1	Signal processing procedure. . . . .	78
5.2	MATLAB simulation of windowing technique . . . . .	80
5.3	CST simulation of ramp modulation . . . . .	81
5.4	MATLAB simulation of calibrated beat signals . . . . .	82
5.5	Two targets simulation . . . . .	83
5.6	Block diagram of the deconvolution method. . . . .	85
5.7	Spectrum after deconvolution . . . . .	85
5.8	Block diagram of the spectral envelope and impulsization method. . . . .	86
5.9	Spectrum after spectral envelope and impulsization method . . . . .	86
5.10	LSAR cartesian coordinates system. . . . .	88
5.11	LSAR MATLAB simulation . . . . .	88
5.12	CSAR cylindrical coordinate system. . . . .	90
5.13	CSAR MATLAB simulation . . . . .	90
5.14	Beat signal range profile (range) . . . . .	91
5.15	LSAR measurement setup. . . . .	93
5.16	Beat signal range profile (cross-range) . . . . .	94
5.17	Cross-range resolution for various phase noise and integration angle values. . . . .	95
6.1	Measurement range profiles for the calibration target at 20 cm and 30 cm. . . . .	98
6.2	Measurement range profiles for the calibration target at 30 cm . . . . .	99
6.3	The actual vs. measured range . . . . .	100
6.4	SAR image reconstruction validation . . . . .	101
6.5	LSAR image scene . . . . .	102
6.6	LSAR image . . . . .	103
6.7	CSAR image scene . . . . .	104
6.8	CSAR image . . . . .	104

# List of Tables

1.1	IEEE Standard RF Letter-Band Nomenclature . . . . .	18
2.1	ADS Phase Noise Modulation Parameters and Results . . . . .	30
2.2	Relation of Phase Noise and Jitter . . . . .	30
2.3	Relation of Voltage Noise and Jitter . . . . .	30
2.4	Relation of Phase Noise and Range Accuracy for Various Target Ranges . . . . .	32
2.5	Relation of Component Parameters and System Performances . . . . .	38
2.6	Component Parameters for the Nonideal FMCW Radar System . . . . .	41
3.1	Ramp Signal Measurement Results . . . . .	45
3.2	Comparison of Different VCOs Capable of S-Band Operation. . . . .	47
3.3	Specifications of the FMCW Radar Components . . . . .	56
3.4	Specifications of the FMCW Radar System . . . . .	56
4.1	E- and H-planes XP level . . . . .	69
5.1	Range Resolution for Various Phase Noise and Bandwidth Values . . . . .	92
5.2	Cross-Range Resolution for Various Phase Noise and Integration Angle Values . . . . .	93
5.3	Cross-Range Resolution Equation . . . . .	96

# Chapter 1

## Introduction

### 1.1 Motivation

Since World War II, radars have been extensively used for civilian and military applications in the form of impulse radars or continuous wave (CW) radars. One preferred class within CW radars is the frequency-modulated continuous wave (FMCW) radar. The FMCW radar operates by modulating the carrier in frequency and uses deramp processing (or stretch processing, dechirp) to display the target distance in the form of beat frequency (or intermediate frequency). FMCW radars are not only limited to military applications but also applied to commercial tasks such as snow thickness measurement [1], terrain displacement monitoring [2, 3], through-wall detection [4], piston localization in hydraulic cylinder [5], gaseous media fluctuation detection [6], and life activity monitoring [7], as well as automotive applications in collision avoidance [8], adaptive cruise control [9], and all weather cruise control [10]. Furthermore, FMCW radars are extensively used in imaging applications.

The combination of FMCW technology with the synthetic aperture radar (SAR) principle [11] leads to a low cost and miniaturized high resolution imaging sensor. Several SAR techniques have been adapted for FMCW radars in [12–15]. However, there are a few design

issues associated with FMCW radar systems that need to be addressed in order to design an optimal FMCW SAR imaging system. The prominent design issues include the modulation of the beat signal, the phase noise of the transmitted signal and its sweep distortion. To resolve these issues, hardware and software approaches have been proposed in [16–21]. Nonetheless, these approaches resolve only individual issues, which limit their applicability in the design of FMCW SAR imaging systems.

Radar system simulations provide insightful information about the effects of component parameters on the overall system performance. Accurate system simulations prevent the design of over-specified systems and provide an understanding of the trade-offs between component parameters on system level for the beat signal. Several FMCW radar system simulations have been proposed in [22–25]. However, these simulations generally suffer from the lack of a comprehensive model and range accuracy performance analysis. Furthermore, a study on the effect of VCO phase noise on SAR image resolution was missing in the literature.

This thesis aims to develop an S-band homodyne FMCW-SAR system, using off-the-shelf components, for near distance imaging applications. This will be accomplished with the development of a FMCW radar system, signal processing procedure and system calibration techniques. In order to validate the performance of the FMCW radar, near distance targets are imaged using linear SAR (LSAR) and circular SAR (CSAR) techniques.

## 1.2 Background

### 1.2.1 Radar

Radars use electromagnetic (EM) waves to detect and localize the targets. The main types of radars are the impulse radar and the CW radar, each with its own merits [26]. The CW radar transmitter consists of a single oscillator operating at a constant frequency, and the receiver consists of a mixer to process the reflected signals from a moving target. The velocity of the moving target results in a Doppler frequency shift ( $f_D = 2v/\lambda$ ). However, the CW radar is unable to measure range. As the technology advanced, the impulse radar [27–29] and the FMCW radar were developed [30, 31], both of which are capable of measuring the target range and velocity. Nevertheless, the FMCW radar imposes less constraints on the component specifications compared to the impulse radar, which translates to a low cost and miniaturized system design. Therefore, FMCW radar is an important class of radar that is able to measure the target range and velocity, while simultaneously maintain the advantages of a CW radar. FMCW radar has several significant advantages over impulse radar: lower peak power, less susceptible to interception, lower cost, lower sampling rate, highly system integrative and minimum target distance.

### 1.2.2 FMCW Radar Principles and Architectures

In order to determine the target range, a timing reference should be applied to the CW transmission signal that allows the time of transmission and reception to be recognized [32]. A frequency-modulation of the CW transmission signal across time has been shown to be successful, where the timing reference is established by the change in frequency. After the deramp processing, the target distance is in the form of beat frequency.

The main architectures of FMCW radars are the heterodyne and the homodyne. In general, heterodyne architecture is achieved with an additional oscillator to generate a new

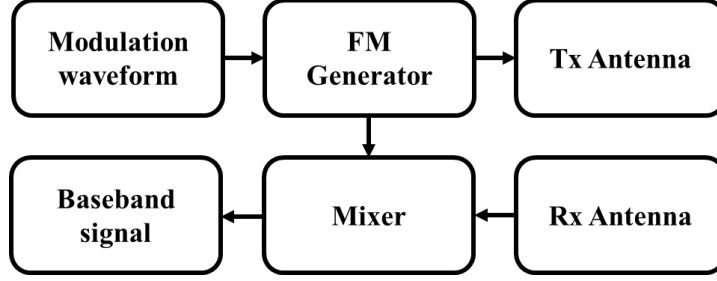


Figure 1.1: Simplified block diagram of the homodyne FMCW radar system.

frequency at the local oscillator (LO) port of the mixer for deramp processing. In [33–35], FMCW radars with heterodyne transceiver architecture are used to implement range gate based on narrow-band filters. In [36], a FMCW radar with heterodyne transceiver architecture is used to eliminate the low-frequency self-mixing spectrum by filtering the up-converted baseband signal. On the other hand, the homodyne architecture is achieved with a direct copy of the transmitted signal at the LO port of the mixer for deramp processing. In [37,38], FMCW radars with homodyne transceiver architecture are implemented for simplicity, low cost and miniaturized system design.

A simplified block diagram of the homodyne FMCW radar system is shown in Fig. 1.1, and can be described as follows: First, a periodic waveform is used to modulate the transmitter (Tx) signal. Several periodic waveforms can be considered for Tx signal modulation, but the most popular are the ramp sweep (or asymmetrical sweep) and the triangular sweep (or symmetrical sweep), as shown in Fig. 1.2. For the same target distance, a triangular sweep will result in a beat frequency approximately two times higher than the beat frequency generated by a ramp sweep [39]. Therefore, the ramp sweep is selected to reduce the sampling rate requirements. The output of the FM generator (or VCO) is a chirp signal, which is radiated by a Tx antenna. The reflected signal is received by a receiver (Rx) antenna and down-converts through a mixer. The output of the mixer is a beat frequency, which is proportional to the transit time between the Tx and Rx signals.

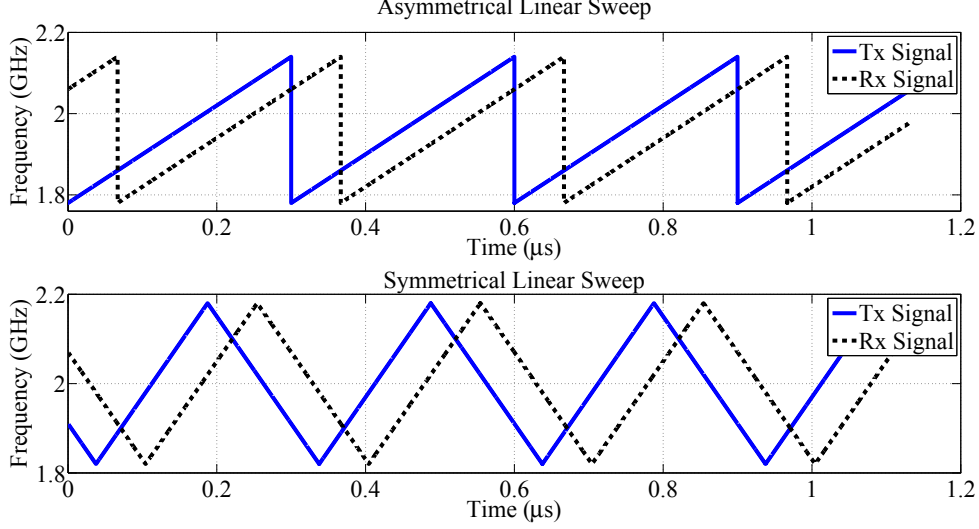


Figure 1.2: Linear sweep functions.

### 1.2.3 Mathematical Modelling

The mathematical equations to model the ideal and nonideal FMCW radar signals are presented here. First, an analysis of an ideal FMCW radar is shown below. The ideal transmitted and received signals can be represented by [40]

$$\begin{aligned}
 s_t^{ideal}(t) &= A_t \cos(\phi_t^{ideal}(t)) \\
 s_r^{ideal}(t) &= A_r \cos(\phi_r^{ideal}(t))
 \end{aligned}
 \tag{1.1}$$

where  $A_t$  and  $A_r$  are the amplitudes, and  $\phi_t^{ideal}(t)$  and  $\phi_r^{ideal}(t)$  are

$$\begin{aligned}
 \phi_t^{ideal}(t) &= 2\pi \int_0^t f_t^{ideal}(t) dt = 2\pi f_s t + \pi c_r t^2 + C \\
 \phi_r^{ideal}(t) &= 2\pi \int_0^t f_r^{ideal}(t) dt = 2\pi f_s (t - \tau_d) + \pi c_r (t - \tau_d)^2 + C
 \end{aligned}
 \tag{1.2}$$

where  $f_s$  is the starting frequency,  $c_r$  is the chirp rate,  $\tau_d$  is the time delay and  $C$  is the integration constant. For a homodyne Rx, some of the transmitted signal is coupled into the LO port of the mixer. The beat signal at the intermediate frequency (IF) port can be

represented by

$$s_b'^{ideal}(t) = s_t^{ideal}(t) \cdot s_r^{ideal}(t) \quad (1.3)$$

where the identity  $2\cos(x)\cos(y) = \cos(x+y) + \cos(x-y)$  is applied to evaluate (1.3), so the resultant beat signal can be represented by

$$s_b'^{ideal}(t) = \frac{A_t A_r}{2} \left[ \cos(4\pi f_s t + 2\pi c_r t^2 - 2\pi f_s \tau_d - 2\pi c_r \tau_d t + \pi c_r \tau_d^2) + \cos(2\pi f_s \tau_d + 2\pi c_r \tau_d t - \pi c_r \tau_d^2) \right] \quad (1.4)$$

The first term in (1.4) is a high frequency term that is attenuated by either the upper frequency limit of the IF port, or by the active low-pass filter (LPF) placed immediately after the IF port. Therefore, the beat signal can be simplified as

$$s_b^{ideal}(t) = \frac{A_t A_r}{2} \cos(2\pi f_s \tau_d + 2\pi c_r \tau_d t - \pi c_r \tau_d^2) \quad (1.5)$$

Let  $\phi_b^{ideal}(t)$  be:

$$\phi_b^{ideal}(t) = 2\pi f_s \tau_d + 2\pi c_r \tau_d t - \pi c_r \tau_d^2 \quad (1.6)$$

The beat frequency for an ideal FMCW radar can be represented by

$$f_b^{ideal}(t) = \frac{1}{2\pi} \frac{d}{dt} \phi_b^{ideal}(t) = c_r \tau_d \quad (1.7)$$

Then the range of the target can be represented by

$$R^{ideal} = \frac{c T_{ramp}}{2B} f_b^{ideal}(t) \quad (1.8)$$

where  $c$  is the speed of the pulse in the medium,  $T_{ramp}$  is the sweep duration of the ramp signal and  $B$  is the frequency bandwidth. If multiple targets are present, each individual target

will contribute to a beat frequency. Then the output of the mixer will be a superposition of beat frequencies represented by

$$s_b^{ideal}(t) = \frac{A_t A_r}{2} \sum_{i=1}^N \cos(2\pi c_r \tau_{di} t) \quad (1.9)$$

In order to model a more realistic FMCW radar, the nonlinearity inherent to a FM generator (or VCO) needs to be accounted for. Next, an analysis of a nonideal FMCW radar is shown below. The nonideal transmitted and received signals can be represented by [40]

$$\begin{aligned} s_t^{ideal}(t) &= A_t \cos(\phi_t^{ideal}(t)) \\ s_r^{ideal}(t) &= A_r \cos(\phi_r^{ideal}(t)) \end{aligned} \quad (1.10)$$

where  $A_t$  and  $A_r$  are the amplitudes, and  $\phi_t^{ideal}(t)$  and  $\phi_r^{ideal}(t)$  are

$$\begin{aligned} \phi_t^{ideal}(t) &= 2\pi \int_0^t f_t^{ideal}(t) dt = 2\pi f_s t + \pi c_r t^2 + \epsilon(t) + C \\ \phi_r^{ideal}(t) &= 2\pi \int_0^t f_r^{ideal}(t) dt = 2\pi f_s (t - \tau_d) + \pi c_r (t - \tau_d)^2 \\ &\quad + \epsilon(t - \tau_d) + C \end{aligned} \quad (1.11)$$

where  $\epsilon(t)$  is the phase due to distortion of the sweep generator and/or due to other components. Then the beat signal at the IF port can be represented by

$$\begin{aligned} s_b'^{ideal}(t) &= \frac{A_t A_r}{2} \left[ \cos(4\pi f_s t + 2\pi c_r t^2 - 2\pi f_s \tau_d - 2\pi c_r \tau_d t + \pi c_r \tau_d^2 + \epsilon(t) + \epsilon(t - \tau_d)) + \right. \\ &\quad \left. \cos(2\pi f_s \tau_d + 2\pi c_r \tau_d t - \pi c_r \tau_d^2 + \epsilon(t) - \epsilon(t - \tau_d)) \right] \end{aligned} \quad (1.12)$$

The beat signal can be further simplified as

$$s_b^{ideal}(t) = \frac{A_t A_r}{2} \cos(2\pi f_s \tau_d + 2\pi c_r \tau_d t - \pi c_r \tau_d^2 + \epsilon(t) - \epsilon(t - \tau_d)) \quad (1.13)$$

Let  $\phi_b^{ideal}(t)$  be:

$$\phi_b^{ideal}(t) = 2\pi f_s \tau_d + 2\pi c_r \tau_d t - \pi c_r \tau_d^2 + \epsilon(t) - \epsilon(t - \tau_d) \quad (1.14)$$

Therefore, the beat frequency for a nonideal FMCW radar can be represented by

$$f_b^{ideal}(t) = \frac{1}{2\pi} \frac{d}{dt} \phi_b^{ideal}(t) = c_r \tau_d + \beta'(t) - \beta'(t - \tau_d) \quad (1.15)$$

Next, Taylor's theory is applied to develop an expression for the nonlinear phase error term ( $\epsilon(t)$ ) shown below. According to Taylor's theory, any nonlinear function can be approximated using a finite number of Taylor series terms [41]. Then the nonlinear term in the Tx signal can be represented by

$$f_t^{ideal}(t) = \sum_{i=0}^{\infty} c_{ri} t^i \quad (1.16)$$

In general, a second-order approximation is sufficient to model the Tx nonlinearity [41]. Therefore, (1.16) can be simplified to

$$f_t^{ideal}(t) = c_{r0} + c_{r1}t + c_{r2}t^2 \quad (1.17)$$

This is compared to the nonideal Tx frequency expression, which can be represented by

$$f_t^{ideal}(t) = f_s + c_r t + \zeta(t) \quad (1.18)$$

Let  $\zeta(t)$  be:

$$\zeta(t) = c_{r2}t^2 \quad (1.19)$$

Then the instantaneous phase of the nonideal transmitted and received signals can be rep-

resented by

$$\begin{aligned}\phi_t^{nideal}(t) &= 2\pi \int_0^t f_t^{nideal}(t)dt = 2\pi f_s t + \pi c_r t^2 + \frac{2\pi}{3} c_{r2} t^3 + C \\ \phi_r^{nideal}(t) &= 2\pi \int_0^t f_r^{nideal}(t)dt = 2\pi f_s (t - \tau_d) + \pi c_r (t - \tau_d)^2 \\ &\quad + \frac{2\pi}{3} c_{r2} (t - \tau_d)^3 + C\end{aligned}\tag{1.20}$$

Then the instantaneous phase of the beat signal can be represented by

$$\begin{aligned}\phi_b^{nideal}(t) &= 2\pi f_s \tau_d + 2\pi c_r \tau_d t - \pi c_r \tau_d^2 + \frac{2\pi}{3} c_{r2} t^3 - \frac{2\pi}{3} c_{r2} (t - \tau_d)^3 \\ &\quad \stackrel{\tau_d \ll}{\approx} 2\pi f_s \tau_d + 2\pi c_r \tau_d t + 2\pi c_{r2} \tau_d t^2\end{aligned}\tag{1.21}$$

where if  $\tau_d$  is sufficiently small compared to the sweep time, then the higher order terms can be removed [42]. The nonideal beat frequency can be represented by

$$f_b^{nideal}(t) = \frac{1}{2\pi} \frac{d}{dt} \phi_b^{nideal}(t) = c_r \tau_d + c_{r2} \tau_d t^2\tag{1.22}$$

The beat frequency from (1.22) is a function of time. In other words, the nonlinearity from the VCO results in a nonstationary beat signal [43], which spreads the target energy and degrades the range accuracy and resolution.

## 1.2.4 Performance Metrics

The primary performance metrics of FMCW radars are the maximum range and the range resolution. The maximum range can be represented by [44]

$$R_{max} = \left[ \frac{P_{avg} G_{tx} A_{rx} \rho_{rx} \sigma e^{(2\alpha)}}{(4\pi)^2 k T_0 (NF) B_n \tau_{pulse} f_r (SNR_{min})} \right]\tag{1.23}$$

where  $P_{avg}$  is the average transmit power,  $G_{tx}$  is the Tx antenna gain,  $A_{rx}$  is the Rx antenna effective aperture,  $\rho_{rx}$  is the Rx antenna efficiency,  $\sigma$  is the target radar cross section (RCS),  $\alpha$  is the attenuation constant,  $k$  is the Boltzmann's constant ( $1.38 \cdot 10^{-23}$  J/°K),  $T_0$  is

the standard temperature (290°K),  $NF$  is the system noise figure,  $B_n$  is the system noise bandwidth,  $\tau_{pulse}f_r$  is the duty cycle and  $SNR_{min}$  is the minimum SNR requirement. It can be observed from (1.23) that range depends on the minimum detectable signal (MDS) strength, which can be represented by

$$MDS (dBm) = -174 dBm + 10 \log_{10}(B_{rx}) + NF (dB) + SNR_{min} (dB) \quad (1.24)$$

where  $B_{rx}$  is the receiver bandwidth.

The criterion for range resolution is that the peaks of the overlapped beat frequencies should be separated by at least half of their peak values [39]. For a homodyne FMCW radar, the range resolution can be represented by [45, 46]

$$\Delta_R = \frac{T_{ramp}c}{2B} \Delta f_b \quad (1.25)$$

where  $\Delta f_b$  is the beat frequency resolution.

## 1.2.5 System Noise

Noise is a well-known problem in the design of radar systems. The main types of noise are the internally generated noise and the externally generated noise. The internally generated noise includes thermal and flicker noise. Thermal noise (or Gaussian noise, Johnson noise) is generated by the random thermal motion of conduction electrons for materials above 0°K. The mean-square noise voltage from this thermal motion can be represented by

$$\begin{aligned} \overline{v_n^2(t)} &= \frac{1}{T} \int_0^T v_n^2(t) dt = 4kRTB \\ \overline{i_n^2(t)} &= \frac{1}{T} \int_0^T i_n^2(t) dt = \frac{4KTB}{R} \end{aligned} \quad (1.26)$$

where  $T$  is the temperature in Kelvins and  $R$  is the resistance. Furthermore, thermal noise has a nearly constant power spectral density (PSD) across the frequency spectrum and determines the noise floor level (NFL). On the other hand, flicker noise (or pink noise) is generated by the random fluctuations of carriers in active devices. Furthermore, flicker noise has a  $1/f$  PSD across the frequency spectrum and determines the phase noise level.

Externally generated noise includes power supply and radiation noise. Power supply noise is generated by the 50 Hz (or 60 Hz) AC frequency from the walls and can appear at the circuit. Nevertheless, this noise can be effectively suppressed with proper selection of bypass capacitors, RF chokes and filters. Radiation noise is generated by the propagation of radio frequency (RF) waves in the environment, which can couple into the circuit. Nonetheless, this noise can be effectively suppressed by proper placement and design of EM interference shields with metal enclosures or absorbers [47].

### 1.2.6 Phase Noise

Phase noise is a critical problem in the design of FMCW radar systems. It is inherent to a VCO and has shown to increase overall system NFL, decrease Rx sensitivity and degrade resolution [48, 49]. The mathematical equations and definitions to describe phase noise are presented here. First, the relation between frequency deviation and modulation sidebands is shown. The output signal of an ideal VCO fed with a single tuning voltage can be represented by [42]

$$s_{VCO}^{ideal} = V_c \cos(\omega_c t) \quad (1.27)$$

where  $\omega_c$  is the carrier frequency. The frequency spectrum of an ideal VCO output signal is a single delta function at the carrier frequency as shown in Fig. 1.3(a). However, the output

signal of a nonideal VCO fed with a single tuning voltage can be represented by

$$s_{VCO}^{ideal} = V_c(1 + \xi(t))\cos(\omega_c t + \psi(t)) \quad (1.28)$$

where  $\xi(t)$  and  $\psi(t)$  are the amplitude and phase noise respectively. Nevertheless, most VCO designs include signal limiters to suppress the amplitude noise [50]. As a result, the amplitude variations are well attenuated and controlled. Consequently, the VCO output spectrum is mainly dominated by phase noise and (1.28) can be simplified to

$$s_{VCO}^{ideal} = V_c\cos(\omega_c t + \psi(t)) \quad (1.29)$$

The frequency spectrum of a nonideal VCO output signal has a skirt of noise as shown in Fig. 1.3(b). Furthermore, small changes in the oscillator frequency can be represented by

$$\psi(t) = \frac{\Delta f}{f_m}\sin(\omega_m t) = \psi_p\sin(\omega_m t) \quad (1.30)$$

where  $\omega_m$  is the modulating frequency and  $\psi_p$  is the peak phase deviation. Then (Eq.1.30) is substituted into (Eq.1.29) and the VCO output spectrum can be represented by

$$s_{VCO}^{ideal} = V_c\cos(\omega_c t + \psi_p\sin(\omega_m t)) \quad (1.31)$$

where the identity  $\cos(x + y) = \cos x \cos y - \sin x \sin y$  is applied to evaluate (Eq.1.31) and the resultant VCO output spectrum can be further represented by

$$\begin{aligned} s_{VCO}^{ideal} &= V_c \left[ \cos(\omega_c t) \cos(\psi_p \sin(\omega_m t)) - \sin(\omega_c t) \sin(\psi_p \sin(\omega_m t)) \right] \\ &\stackrel{\psi_p \ll 1}{\approx} V_c \left[ \cos(\omega_c t) - \psi_p \sin(\omega_m t) \sin(\omega_c t) \right] \\ &\stackrel{\psi_p \ll 1}{\approx} V_c \left[ \cos(\omega_c t) - \frac{\psi_p}{2} \left[ \cos(\omega_c + \omega_m)t - \cos(\omega_c - \omega_m)t \right] \right] \end{aligned} \quad (1.32)$$

where for sufficiently small  $\psi_p$ , the small-argument expressions of  $\sin x \approx x$  and  $\cos x \approx 1$

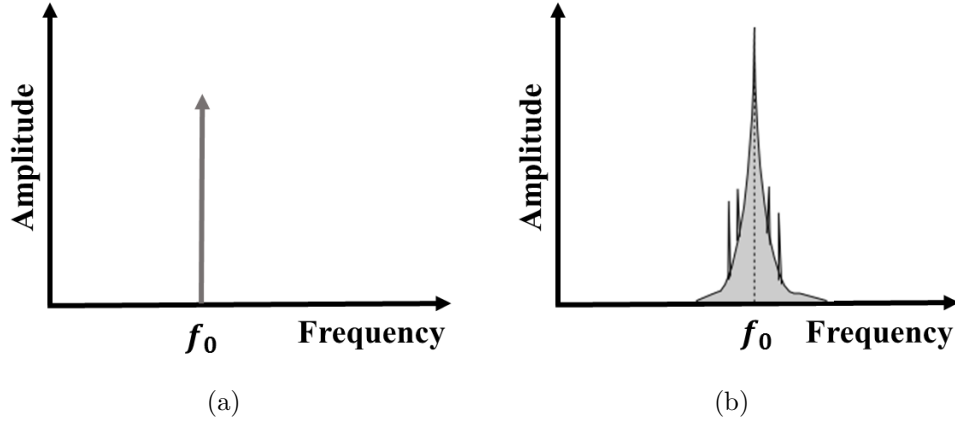


Figure 1.3: Frequency spectrum of: (a) ideal VCO output, and (b) nonideal VCO output.

can be applied. It can be observed from (Eq.1.32) that a small phase or frequency deviation in the VCO output results in modulation sidebands at  $\omega_c \pm \omega_m$  located on either side of the carrier frequency  $\omega_c$ .

Next, three definitions for the VCO phase noise are presented. First, the IEEE definition for phase noise can be represented by [51]

$$\mathcal{L}(f) = \frac{S_\psi(f)}{2} \quad (1.33)$$

where  $S_\psi$  is the phase PSD represented by

$$S_\psi(f) = \frac{\psi^2(f)}{B} \quad (1.34)$$

It can be observed from (1.33) that due to symmetry, only half of the phase PSD is considered, and the phase noise level is determined relative to the carrier frequency in a single-side-band (SSB) PSD of 1 Hz bandwidth.

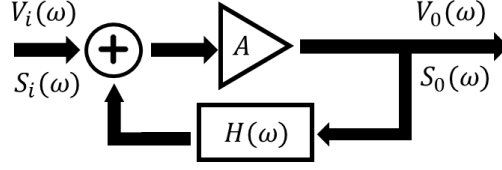


Figure 1.4: Feedback amplifier model for characterizing oscillator phase noise.

Second, phase noise can be characterized by Leeson's model [52], which begins by modelling the VCO as an amplifier with feedback shown in Fig. 1.4. The output voltage can be represented by

$$V_0(\omega) = AV_i(\omega) + AH(\omega)V_0(\omega) \quad (1.35)$$

where  $A$  is the voltage gain and  $H(\omega)$  is the feedback transfer function. Additionally, (Eq. 1.35) can also be represented by

$$V_0(\omega) = \frac{AV_i(\omega)}{1 - AH(\omega)} \quad (1.36)$$

Then  $H(\omega)$  for a Colpitts VCO can be represented by

$$H(\omega) = \frac{1}{1 + 2jQ_0\left(\frac{\Delta\omega}{\omega_c}\right)} \quad (1.37)$$

where  $Q_0$  is the quality factor,  $\omega_c$  is the carrier frequency and  $\Delta\omega$  is the frequency offset relative to the carrier frequency. Since the input and output PSD are related by the square of the magnitude of the voltage transfer function, the PSD transfer function can be represented by

$$S_0(\omega) \stackrel{A=1}{=} \left| \frac{1}{1 - H(\omega)} \right|^2 S_i(\omega) \quad (1.38)$$

Then (Eq. 1.37) is substituted into (Eq. 1.38), and the PSD transfer function can be repre-

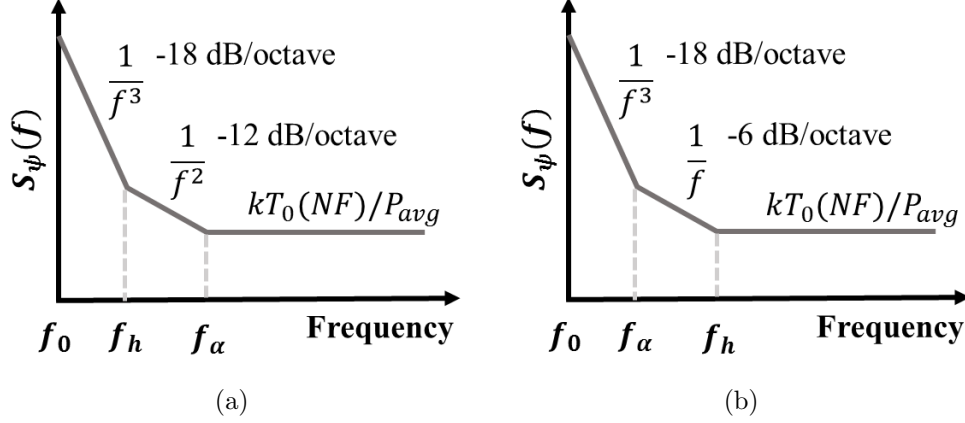


Figure 1.5: Output PSD response for: (a)  $\omega_h < \omega_\alpha$  (high Q), and (b)  $\omega_h > \omega_\alpha$  (low Q).

sented by

$$S_0(\omega) = \left(1 + \frac{\omega_h^2}{\Delta\omega^2}\right) S_i(\omega) \quad (1.39)$$

where  $\omega_h = \omega_c/2Q_0$  is the half-power bandwidth of the resonator. Since the input PSD consists mainly of thermal and flicker noise, the input PSD can be represented by

$$S_i(\omega) = \underbrace{\frac{kT_0(NF)}{P_{avg}}}_{\text{Thermal}} \left(1 + \underbrace{\frac{K\omega_\alpha}{\Delta\omega}}_{\text{Flicker}}\right) \quad (1.40)$$

where  $\omega_\alpha$  is the corner frequency of the flicker noise and  $K$  is the constant accounting for the strength of the flicker noise. Then (Eq. 1.40) is substituted into (Eq. 1.39), and the output PSD can be further represented by

$$S_0(\omega) = \frac{kT_0(NF)}{P_{avg}} \left( \frac{K\omega_\alpha\omega_h^2}{\Delta\omega^3} + \frac{\omega_h^2}{\Delta\omega^2} + \frac{K\omega_\alpha}{\Delta\omega} + 1 \right) \quad (1.41)$$

There are two solutions for (1.41), which depends on whether  $\omega_h$  or  $\omega_\alpha$  is greater, as shown in Fig. 1.5. As it can be seen, Leeson's model is able to characterize the phase noise roll-off with respect to a frequency offset from the carrier, which provides a more in-depth understanding on the overall phase noise performance.

Third, the VCO phase noise can also be modelled as time jitter. Phase noise and time jitter are related quantities, where phase noise is a frequency domain view of the noise spectrum around the oscillator signal, while jitter is a time domain measure of the timing accuracy of the oscillator period. The relationship between phase noise and time jitter can be represented by [53]

$$J_{RMS}(t) = \frac{\sqrt{2 \int_{f_1}^{f_2} L_\psi(f) df}}{2\pi f_c} \quad (1.42)$$

where  $f_c$  is the center frequency,  $f_1$  is the initial offset frequency,  $f_2$  is the cut-off offset frequency and  $L_\psi(f)$  is the single sideband phase noise spectrum, which can be represented by

$$L_\psi(f) = 10^{\frac{\chi}{10}} \quad (1.43)$$

where  $\chi$  is the phase noise power in dB relative to the carrier frequency.

### 1.2.7 Frequency Selection

The International Telecommunications Union has divided the microwave spectrum into sub-bands, and the IEEE has standardized the radar letter-band nomenclature, as shown in Table. 1.1. Transmission in the EM spectrum is regulated by government bodies, such as the Federal Communications Commission in United States and Industry Canada in Canada. A radio license is required to operate in most of the EM spectrum. However, notable exceptions are the industrial, scientific, and medical (ISM) band, which are 6765-6795 kHz, 433-435 MHz, 61-61.5 GHz, 122-123 GHz and 244-246 GHz in Canada [54], and the Ultra-wideband (UWB), which is 3.1-10.6 GHz in North America [55]. Though a license is not required, explicit rules exist for transmission in the ISM and UWB bands, especially related to the allowed power densities. Furthermore, Industry Canada has also allocated specific licensing

frequency bands for radar applications (e.g., radio-navigation and radio-location) [56].

It has been shown that the FMCW radar range resolution can improve with a wider bandwidth (see section 1.2.4). This attracts the use of high frequencies, since the frequency allocation for radar usage is quite fragmented. Therefore, a wider bandwidth is more easily obtained at higher frequencies. Also, higher frequencies translate to smaller antenna size, since the antenna size is usually related to the wavelength at  $\sim \lambda/4$ . Nevertheless, there are also advantages for using lower frequencies, such as lower cost and increase availability of components. Also, lower frequencies allow a better penetration capability for through-wall applications. In this thesis, a FMCW radar system operating at 1.9-3.7 GHz is designed. This frequency range falls approximately in the S-band and is a rather high frequency band. However, it is mainly chosen due to the cost and availability of the RF components.

## 1.2.8 Applications

In recent years, FMCW radars have attracted attention from both industry and academia for their advantages (see section 1.2.1). FMCW radars have been shown to be successful in applications such as snow thickness measurement, terrain displacement monitoring, through-wall detection, piston localization in a hydraulic cylinder, gaseous media fluctuation detection, life activity monitoring, as well as automotive applications in collision avoidance, adaptive cruise control and all weather cruise control. For example, Galin et al. [1] have mounted a S-C band FMCW radar on a helicopter to measure the snow thickness over East Antarctica. Iglesias et al. [2, 3] have used a ground based C- $K_u$  band FMCW radar, with interferometry SAR and persistent scatterer interferometry techniques, to monitor the different kinds of ground displacements. Charvat et al. [4] have implemented a S-band FMCW radar, with range gate capability based on narrow-band filters, to avoid the strong reflection from the wall that can

Table 1.1: IEEE Standard RF Letter-Band Nomenclature

Band Nomenclature	Nominal Frequency Range
HF	3 - 30 MHz
VHF	30 - 300 MHz
UHF	300 - 1000 MHz
L	1 - 2 GHz
S	2 - 4 GHz
C	4 - 8 GHz
X	8 - 12 GHz
$K_u$	12 - 18 GHz
K	18 - 27 GHz
$K_a$	27 - 40 GHz
V	40 - 75 GHz
W	75 - 110 GHz
mm	110 - 300 GHz

saturate the radar Rx. Ayhan et al. [5] have presented a K-band FMCW radar capable of localizing the piston position while submerged in an oil filled medium. Baer et al. [6] have used a W-band FMCW radar, with dielectric mixing equations, to detect the fluctuation of gases. Wang et al. [7] have developed a C-band FMCW radar for indoor positioning and life activity monitoring, based on transmitting a signal with linear and interferometry modes. Boukari et al., Polychronopoulos et al. and Russel et al. [8–10] have developed various radar architectures for automotive safety applications.

The radar concepts, mathematical models and noise relations establish an understanding for the radar nonlinearities.

## 1.3 Thesis Contribution and Layout

Chapter 2 describes the radar system simulation. A complete FMCW radar system simulation is implemented in ADS, to gain insightful information about the influence of component parameters on the overall system performance. First, an ideal FMCW radar is simulated. Then each component within the system is individually parametrized and systematically studied to understand its effect on SNR, range accuracy and range resolution. Next, the specifications of a practical off-the-shelf VCO is used for simulation, and a curve-fitted equation that estimates the range accuracy in relation to target range and phase noise is presented. Then a table that summarizes the relation between component parameters and system performances is provided. Finally, a nonideal FMCW radar, using off-the-shelf component specifications, is simulated for two-target detection with variation in RCS ratio.

Chapter 3 details the hardware design. An S-band homodyne FMCW radar system, using off-the-shelf components, is designed with low-frequency circuitry and high-frequency components. Different measurement procedures and equipment are used to characterize and compare the component performances with the manufacture and/or design specifications. Then a complete system measurement is carried out in the time domain, using real-time oscilloscope, to characterize the pulse distortion introduced by each component throughout the system. Also, a LabVIEW program is developed to digitize the beat signals and synchronize the Tx and Rx. Finally, tables that summarize the overall system specifications and performances are provided.

Chapter 4 presents the antenna design. A modified bow-tie antenna with low cross-polarization and miniaturization is designed to improve the radar image resolution by suppressing radiation in the orthogonal directions. The antenna's characteristics including return loss, gain and radiation pattern are measured, along with the time domain characteristics, and show reasonable agreement with the simulated results.

Chapter 5 presents the software simulation. An S-band homodyne FMCW radar system simulation is implemented with CST and MATLAB. A signal processing procedure is developed, which can be categorized into two parts: pre-processing and post-processing. The pre-processing stage consists of spectral estimation techniques and mitigation methods for deramp on the beat spectrum. Specifically, two mitigation methods are discussed: the deconvolution method, and the spectral envelope and impulsization method. Then the post-processing consists of either LSAR or CSAR processing, with a modified frequency domain global backprojection (GBP) algorithm for image reconstruction. Finally, the relation between radar resolution, frequency bandwidth, phase noise and aperture length are studied with a LSAR measurement setup.

Chapter 6 discusses the measurement results. The Rx pulse can be affected by scattering from the target(s) and nearby object(s), propagation delay due to the radar components, as well as mutual coupling between the antennas, especially when the antennas are placed in quasi-monostatic configuration. Therefore, system calibration techniques for background noise removal, and correction of time offset due to sweep distortion of the transmitted signal and group delay of the radar components are described. Then the validation of the proposed signal processing procedure using measurement data is presented. Finally, the LSAR and CSAR imaging results for various targets are shown and discussed.

To conclude, Chapter 7 summarizes the result of this work and highlights its key contributions. Furthermore, related incomplete studies are outlined, along with directions for future development for an improved FMCW SAR system.

# Chapter 2

## ADS System Simulation

### 2.1 Literature Review

Several FMCW radar system simulations have been proposed in the literature. For example, Dudek et al. [22,23] have presented the FMCW radar system simulations in ADS and studied the effects of Rx nonlinearity and VCO phase noise on the NFL for single target detection. Scheiblhofer et al. [24] have developed a FMCW radar system simulation in MATLAB and investigated the effects of external noise sources on the NFL for single target detection. Karnfelt et al. [25] have implemented a FMCW radar system simulation in ADS and studied the effects of different architectures and modulation waveforms for single target detection. However, these simulations generally suffer from the lack of a comprehensive model and range accuracy performance analysis.

This chapter presents a complete and practical FMCW radar system simulation in ADS to investigate the influence of component parameters on the overall system performance. The key parameters under study are the nonlinearities and/or nonideal behaviours of the ramp circuit, VCO, power amplifier (PA), low noise amplifier (LNA) and mixer (MIX).

## 2.2 Ideal FMCW Radar System Simulation

An ideal FMCW radar is simulated, as shown in Fig. 2.1(a). The FM signal (or chirp signal) is modelled by a VtPulse and VCO component. The VtPulse component generates a ramp signal, as shown in Fig. 2.1(b). Then the ramp signal feeds the VCO tuning port and outputs a chirp signal with sweep period of 5  $\mu$ s and sweep frequency of 2 to 4 GHz, as shown in Fig. 2.1(c). In the Tx path, the chirp signal propagates through a coupler then an amplifier before reaching the target scene. The target scene is modelled with an attenuator and a time delay component. The attenuator corresponds to the free-space path loss (FSPL), which can be represented by

$$FSPL = 10 \log_{10} \left( \frac{4\pi R}{\lambda\sigma} \right)^2 \quad (2.1)$$

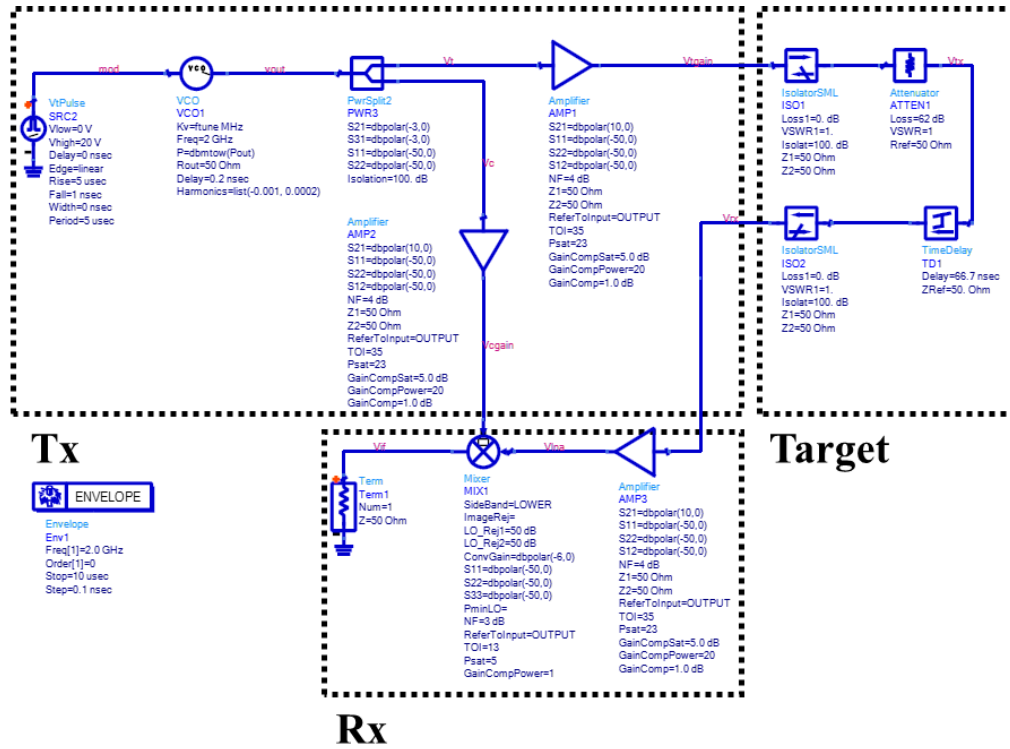
where  $R$  is the target distance and  $\lambda$  is the minimum wavelength of the Tx signal. The time delay component can be represented by

$$\tau_d = \frac{2R}{c} \quad (2.2)$$

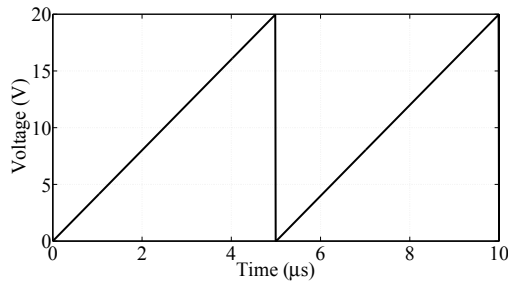
A point target at  $R = 10$  m is represented by a FSPL of 62 dB and time delay of 66.7 ns. In the Rx path, the reflected chirp signal propagates through a LNA and a MIX to output a beat signal at the IF port, as shown in Fig. 2.1(d). It is observed that the beat frequency is 26.6 MHz and is in agreement with the beat frequency of an ideal FMCW radar, which can be represented by (see section 1.2.3)

$$f_b^{ideal}(t) = \frac{2BR}{cT_{ramp}} \quad (2.3)$$

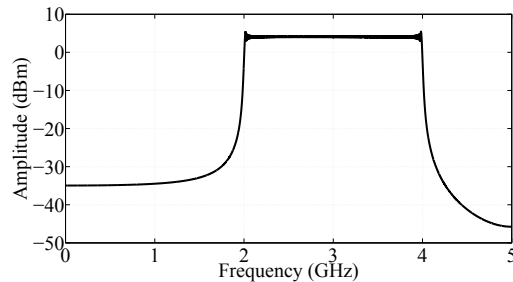
Therefore, the system simulation has been setup correctly. Additionally, the entire simulation is carried out using the circuit envelope simulator, which is a combination of the harmonic balance and transient simulators to simultaneously perform time-frequency analysis and



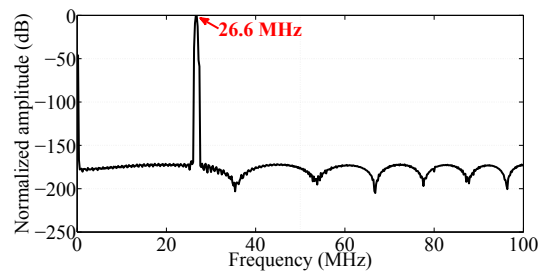
(a)



(b)



(c)



(d)

Figure 2.1: Ideal FMCW radar simulation: (a) Schematic. (b) Ramp signal. (c) VCO output spectrum. (d) Beat spectrum.

speed up the computational time.

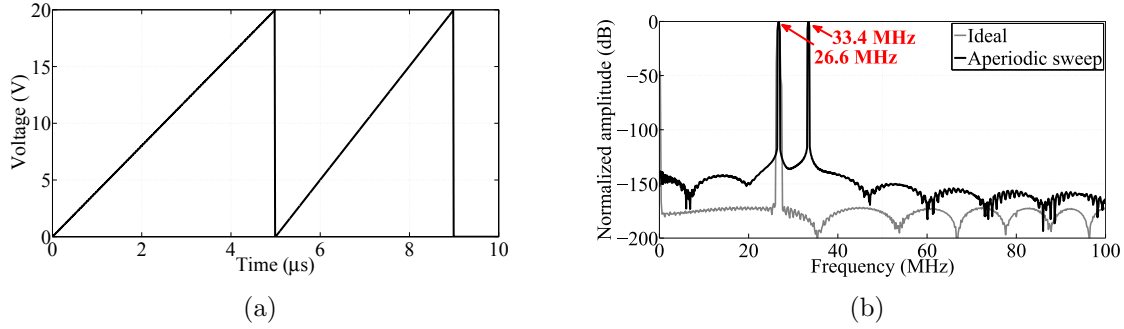


Figure 2.2: Radar simulation with aperiodic sweep period: (a) Ramp signal. (b) Beat spectrum.

## 2.3 Ramp Circuit Parametrization

The ramp circuit provides a linear voltage sweep for the VCO tuning port. Digital components can be used to design a ramp circuit; however, sufficient quantization is required to prevent the generation of harmonics that can appear as false alarms [57]. Such quantization requirements increase the complexity and cost of the circuit design. Therefore, analog components are used to design the ramp circuit. However, analog components have its imperfections that disturbs the ramp signal from its ideal behaviour. Therefore, the key parameters under study for the ramp signal are: sweep period, voltage noise, signal clamp and falling edge.

The sweep period of the ramp signal can be aperiodic due to component tolerances. In the ADS simulation, an aperiodic ramp signal with periods of  $4 \mu\text{s}$  and  $5 \mu\text{s}$  are fed to the VCO, as shown in Fig. 2.2(a). The simulation result of the beat spectrum is shown in Fig. 2.2(b). The expected beat frequency is 26.6 MHz; however, an additional beat frequency of 33.4 MHz is observed when there is only one target present. This distortion creates false alarm and increases the sampling requirement of the analog to digital converter (ADC). Nevertheless, this distortion can be reduced with a longer sweep period, in which a minor time offset in the sweep period will not create a distinct target indication in the beat spectrum.

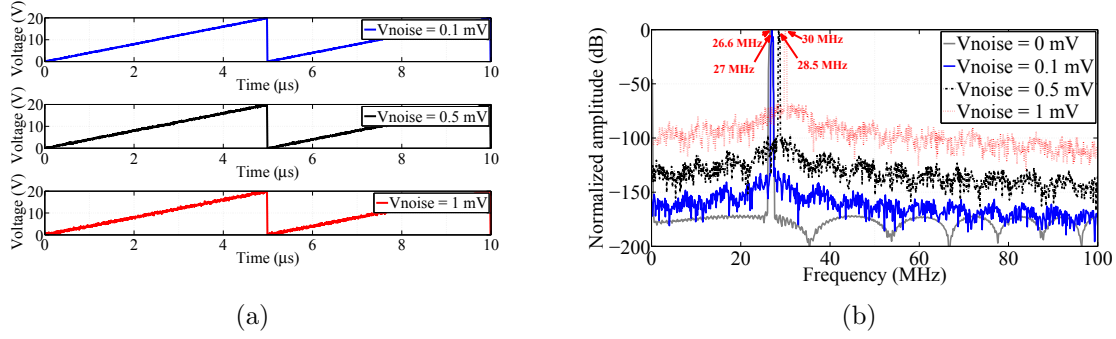


Figure 2.3: Radar simulation with voltage noise in ramp signal: (a) Ramp signal. (b) Beat spectrum.

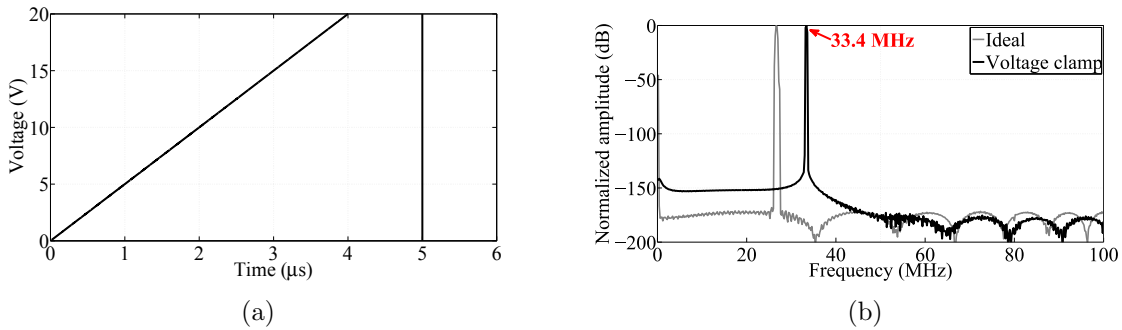


Figure 2.4: Radar simulation with voltage clamp in ramp signal: (a) Ramp signal. (b) Beat spectrum.

The ramp signal can be susceptible to noise coupling from the internal and external noise sources. In the ADS simulation, the voltage ripples can be modelled with a voltage noise source, as shown in Fig. 2.3(a). The simulation result of the beat spectrum is shown in Fig. 2.3(b). The expected beat frequency is 26.6 MHz. However, it is observed that voltage noise levels of 0.1 mV, 0.5 mV and 1 mV results in beat frequencies of 27 MHz, 28.5 MHz and 30 MHz, respectively. It is also observed that an increase in voltage noise widens the mainlobe width and raises the NFL, which degrades Rx sensitivity and dynamic range (DR). In other words, the voltage ripples add to the VCO phase noise to further degrade range accuracy and resolution. Nevertheless, this distortion can be reduced with proper EM shielding and/or adequate grounding.

The ramp voltage can be clamped due to inadequate component selections and tolerances.

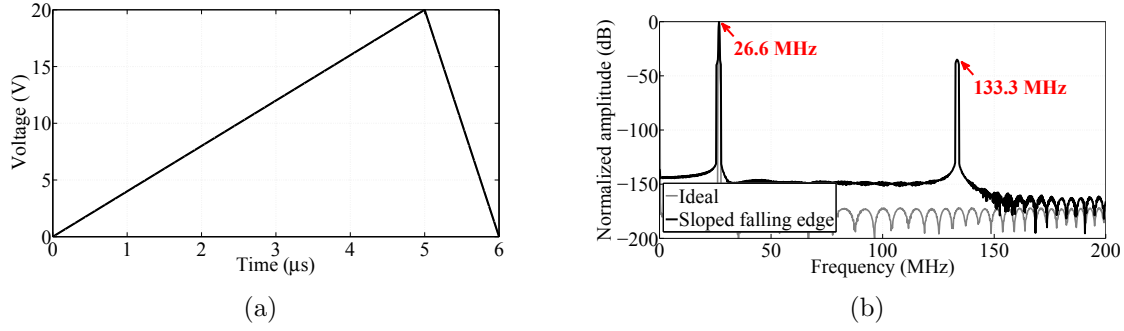


Figure 2.5: Radar simulation with non-instantaneous falling edge ramp signal: (a) Ramp signal. (b) Beat spectrum.

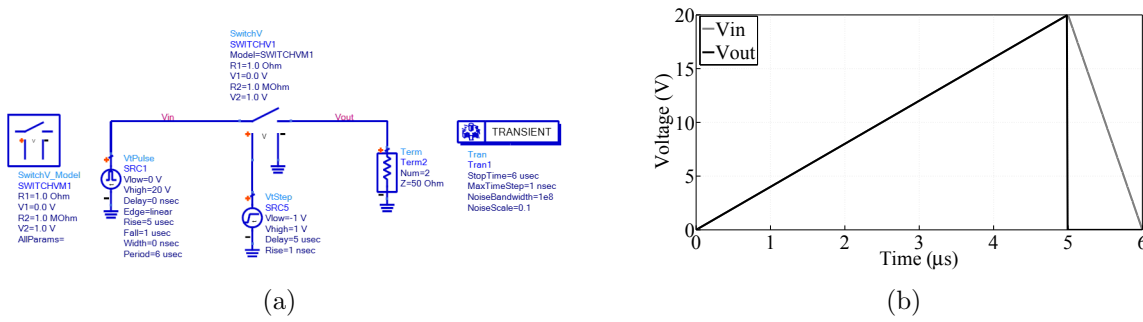


Figure 2.6: Radar simulation with switch circuit: (a) Schematic. (b) Ramp signal.

In the ADS simulation, a clamped ramp signal is shown in Fig. 2.4(a). The simulation result of the beat spectrum is shown in Fig. 2.4(b). The expected beat frequency is 26.6 MHz; however, a beat frequency of 33.4 MHz is observed. This distortion degrades range accuracy and increases the sampling requirement of the ADC. Nevertheless, this distortion can be reduced with careful circuit design and component selection.

The falling edge of the ramp signal may not be instantaneous due to the slew rate limit imposed by the op-amps. In the ADS simulation, the ramp signal has a  $0.5 \mu\text{s}$  fall time, which is 10% of the sweep period, as shown in Fig. 2.5(a). The simulation result of the beat spectrum is shown in Fig. 2.5(b). The expected beat frequency is 26.6 MHz; however, an additional beat frequency of 133.3 MHz is observed when there is only one target present. This distortion creates false alarm and increases the sampling requirement of the ADC. Nevertheless, this effect can be reduced with the use of high-frequency op-amps (e.g., LM318)

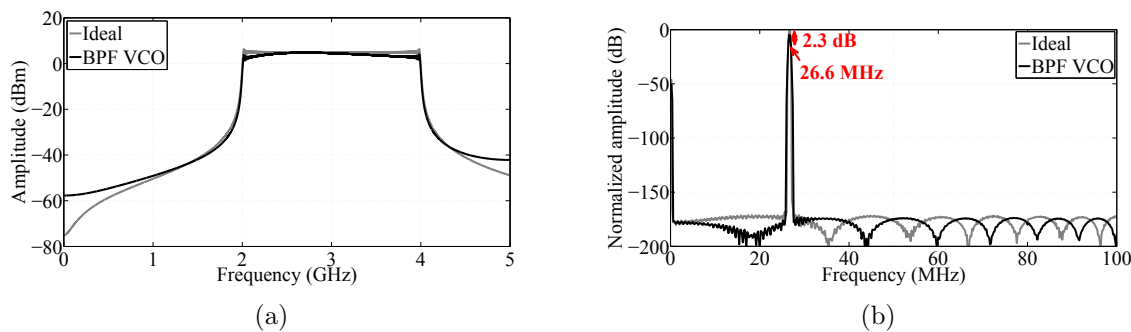


Figure 2.7: Radar simulation with fluctuating power output chirp signal: (a) VCO output spectrum. (b) Beat spectrum.

to achieve a sharp falling edge and/or a LPF to attenuate the higher-frequency signal. Alternatively, a switch circuit (e.g., silicon controlled rectifier diode switch) can be designed to provide an alternative path for the ramp signal to discharge. The schematic and simulation result of the switch circuit are shown in Fig. 2.6. In this manner, the VCO will only detect the voltage from the monotonic slope and is off during the duration of the falling edge.

## 2.4 VCO Parametrization

The ramp circuit is used with the VCO to output a chirp signal. The common VCO architectures are the Colpitts, Hartley and cross-coupled. At the core of most VCOs is a LC tank circuit used to generate the oscillations and an active nonlinear component (e.g., diode or transistor) used to sustain the oscillations. Then the frequency tuning is achieved by changing the capacitance or inductance values. Since nonlinear components are used, VCOs have its imperfections that disturb the chirp signal from its ideal behaviour. Therefore, the key parameters under study for the chirp signal are: power output, phase noise and second harmonics.

The power output of the chirp signal can fluctuate across the frequency due to frequency pulling and tuning sensitivity. In the ADS simulation, the power output fluctuation is modelled by a band-pass filter (BPF) with center frequency of 3 GHz, bandwidth of 1.7 GHz

and passband ripple of 0.1 dB. Then the BPF chirp spectrum is shown in Fig. 2.7(a). The simulation result of the beat spectrum is shown in Fig. 2.7(b). The expected beat frequency is 26.6 MHz with a normalized amplitude of 0 dB; however, a normalized amplitude of -2.3 dB is observed. This nonlinearity degrades Rx sensitivity and DR. Furthermore, this nonlinearity can create unexpected MIX behaviour as the LO drive level can drop below the minimum required LO drive level. Nevertheless, this effect can be reduced with an isolator placed in-between the oscillator output and the load, and/or with a lower tuning sensitivity VCO, and/or a filter with an inverse VCO transfer function to reshape the output spectrum.

The chirp signal can be affected by phase noise due to frequency pushing, tuning sensitivity, Q-factor of the resonator and the varactor and up-converted flicker noise from the oscillation of the transistors. In the ADS simulation, the phase noise of a single frequency tuned VCO (or narrowband VCO) can be modelled by a phase noise modulation component, as shown in Fig. 2.8(a). Then the SSB phase noise profile of the chirp spectrum after phase noise demodulation is shown in Fig. 2.8(b). Table. 2.1 shows the input parameters for the narrowband VCO to display its corresponding phase noise profile. However, in order to model the phase noise for a swept frequency VCO (or wideband VCO), a voltage noise source is used to model the phase noise in time domain as jitter (see section 1.2.6), as shown in Fig. 2.9(a). Table. 2.2 presents the relation of jitter and phase noise, for an off-the-shelf VCO component (see Appendix A), in which the total jitter is 1.5 ps. Then the VCO output signal with phase noise is shown in Fig. 2.9(b). At first glance, the ideal and phase noise added time domain VCO output signals appear the same. However, a zoom into the plot shows the variation due to phase noise. Table. 2.3 shows the relation of voltage noise and phase noise, in which a voltage noise value of 0.1 mV is used to model the off-the-shelf VCO component. The simulation result of the beat spectrum is shown in Fig. 2.10. The expected beat frequency is 26.6 MHz; however, a beat frequency of 27 MHz is observed. This nonlinearity degrades range accuracy, Rx sensitivity and DR. Nevertheless, this nonlinearity

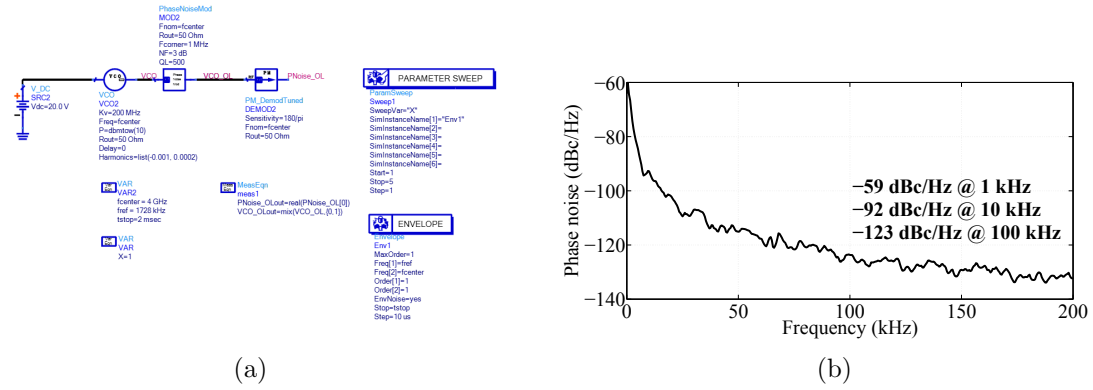


Figure 2.8: Radar simulation with phase noise added to a narrowband VCO: (a) Schematic. (b) SSB Phase noise.

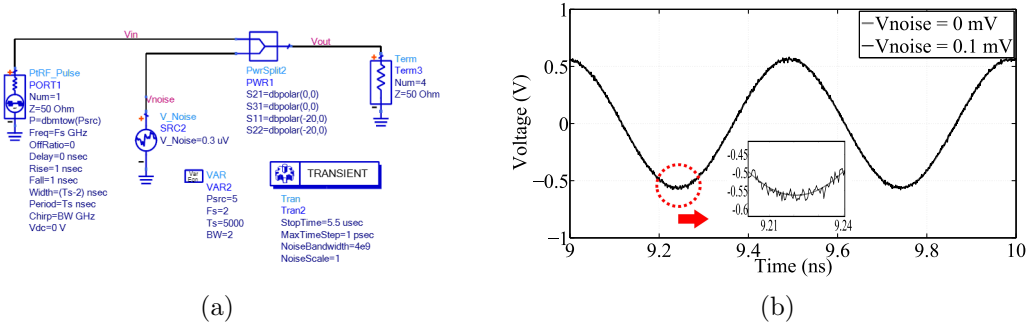


Figure 2.9: Radar simulation with phase noise added to a wideband VCO: (a) Schematic. (b) VCO output signal.

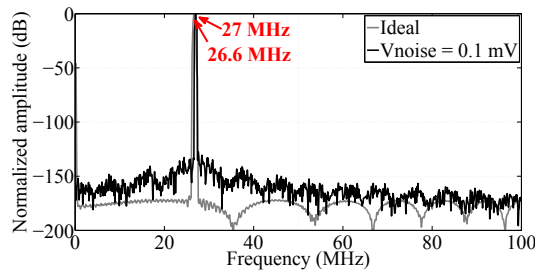


Figure 2.10: Radar simulation with phase noise added to a wideband VCO: Beat spectrum.

can be reduced with careful selection of VCO component, clean power supply, adequate RF grounding, proper load termination and short wire connections.

The effect of VCO phase noise on range accuracy is also studied. In the ADS simulation, three phase noise profiles using off-the-shelf VCO specifications are individually simulated

Table 2.1: ADS Phase Noise Modulation Parameters and Results

ADS Parameters		Results	
NF (dB)	QL	Freq. (kHz)	Phase Noise (dBc/Hz)
7	45	1	-58
7	45	10	-94
7	45	100	-125
8	45	1	-58
8	45	10	-95
8	45	100	-122
9	45	1	-59
9	45	10	-92
9	45	100	-123

Table 2.2: Relation of Phase Noise and Jitter

Freq. (kHz)	Phase Noise (dBc/Hz)	Jitter
1	-65	1.2 ns
10	-89	0.2 ps
100	-110	0.071 ps

Table 2.3: Relation of Voltage Noise and Jitter

Voltage Noise	Jitter
0 $\mu$ V	0 s
1 $\mu$ V	0.01 ps
10 $\mu$ V	0.12 ps
0.1 mV	1.5 ps

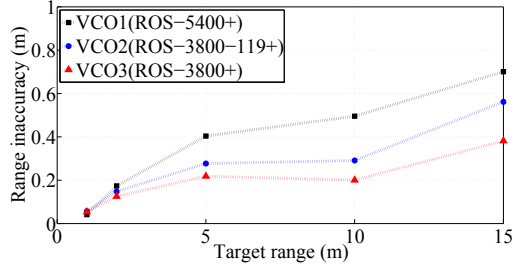


Figure 2.11: MATLAB curve fitted plot of target range and range accuracy for different VCOs.

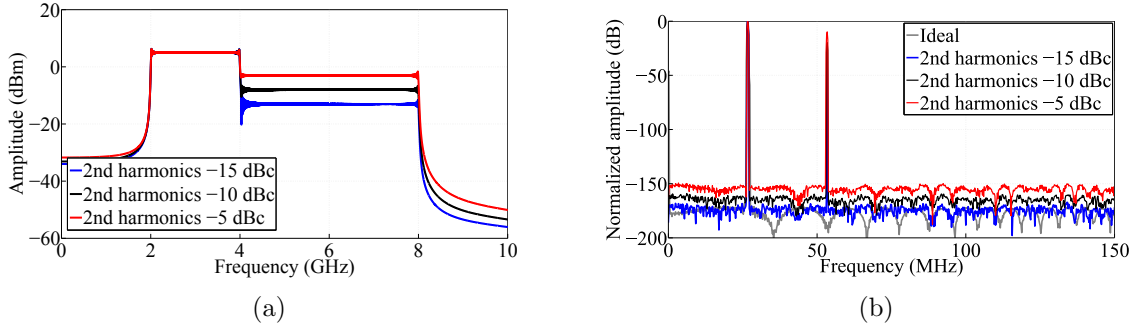


Figure 2.12: Radar simulation with 2nd harmonics: (a) Schematic. (b) VCO output signal.

to determine its effect on range accuracy. Table. 2.4 shows the results, while Fig. 2.11 plots the results. It can be observed that the range accuracy degrades as phase noise deteriorates. The relation of range and range accuracy for the VCO ROS-3800-119+ (see Appendix A) is curve fitted in MATLAB, using polynomial functions, and can be represented by

$$\Delta R_{accuracy} = 7.81 \times 10^{-4} R^3 - 1.83 \times 10^{-2} R^2 + 0.14R - 0.07 \quad (2.4)$$

This relation is specific to the VCO ROS-3800-119+ and valid for  $0 \leq R(m) \leq 15$ . Then an error analysis is performed, in which the average percentage error between ranges 1 to 5 m, 5 to 10 m and 10 to 15 m are 6.2 %, 12.8% and 16.1 %, respectively.

The chirp signal can generate second harmonics due to its nonlinear operation. In the ADS simulation, the second harmonics are modelled by combining two VCOs with fundamental and second harmonic frequencies. Additionally, the power levels of -5 dBc, -10 dBc and

Table 2.4: Relation of Phase Noise and Range Accuracy for Various Target Ranges

VCO	Target Range (m)	Beat Freq. (MHz)	Range Inaccuracy (m)
VCO1	1	2.6	0.025
VCO1	2	6	0.25
VCO1	5	12.3	0.39
VCO1	10	28	0.5
VCO1	15	41.8	0.7
VCO2	1	2.6	0.025
VCO2	2	6	0.25
VCO2	5	14	0.25
VCO2	10	27.5	0.31
VCO2	15	41.5	0.56
VCO3	1	2.72	0.02
VCO3	2	5.81	0.18
VCO3	5	13.84	0.19
VCO3	10	27.22	0.21
VCO3	15	41	0.38

VCO1(ROS-5400+) = -56 dBc/Hz @ 1 kHz, -83 dBc/Hz @ 10 kHz, - 104 dBc/Hz @ 100 kHz.

VCO2(ROS-3800-119+) = -65 dBc/Hz @ 1 kHz, -89 dBc/Hz @ 10 kHz, -110 dBc/Hz @ 100 kHz.

VCO3(ROS-3800+) = -72 dBc/Hz @ 1 kHz, -98 dBc/Hz @ 10 kHz, -119 dBc/Hz @ 100 kHz.

-15 dBc are applied to the second harmonic frequencies. Then the chirp spectrum is shown in Fig. 2.12(a). The simulation result of the beat spectrum is shown in Fig. 2.12(b). The expected beat frequency is 26.6 MHz; however, an additional beat frequency of 53.2 MHz is observed when there is only one target present. This nonlinearity creates false alarm, increases the NFL, degrades Rx sensitivity and DR. Nevertheless, this nonlinearity can be reduced with the use of an external LPF at the VCO output.

## 2.5 PA Parametrization

The PA is used to amplify the signal to provide sufficient power for transmission and/or to meet the minimum LO drive level for the MIX. The main classes of amplifiers are the A, B, AB and C class. At the core of most amplifiers is an impedance matching network used to maximize the power transfer and an active nonlinear component (e.g., diode or transistor) used to amplify the signals. Since nonlinear components are used, amplifiers have its imperfections that disturbs the amplifier output signal from its ideal behaviour. Therefore, the key parameters under study for the amplifier output signal are: NF and 1 dB gain compression point (P1dB).

The amplifier output signal can be affected by NF due to amplifier topology, bandwidth and gain. In general, a low NF can be achieved with a common-source topology at the compromise of a smaller bandwidth and lower gain. The NF can be represented by [42]

$$NF (dB) = 10 \log_{10} \left( \frac{SNR_i}{SNR_o} \right) \quad (2.5)$$

where  $SNR_i$  is the signal-to-noise ratio at the input and  $SNR_o$  is the signal-to-noise ratio at the output. In the ADS simulation, the NF values of 1 dB, 3 dB and 5 dB are applied to the PAs. The simulation result of the beat spectrum is shown in Fig. 2.13. The expected and observed beat frequencies are both 26.6 MHz and the NFL remains relatively the same. Given the NF values, this nonlinearity does not add noticeable defect to the system performance.

The amplifier output signal can be affected by P1dB due to the amplifier class. The difference between the classes of amplifiers lie in the bias current that determines the portion of the cycle the amplifier conducts. Furthermore, the amplifier class determines the theoretical

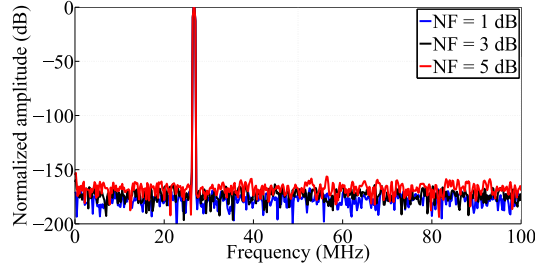


Figure 2.13: Radar simulation with NF varied for the PA: Beat spectrum.

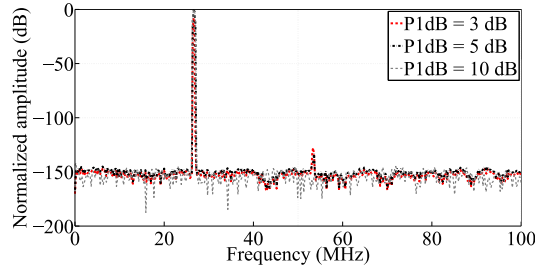


Figure 2.14: Radar simulation with P1dB varied for the PA: Beat spectrum.

maximum power efficiency ( $\eta_{max}$ ), which can be represented by [42]

$$\eta_{max} = \frac{P_{outmax}}{P_{DC}} = 0.25 \frac{2\vartheta - \sin(2\vartheta)}{\sin(\vartheta) - \vartheta \cos(\vartheta)} \quad (2.6)$$

where  $2\vartheta$  is the conduction angle. In general, a high P1dB can be achieved with class A PA at the compromise of a lower power efficiency. The P1dB can be represented by [42]

$$OP_{1dB} (dB) = IP_{1dB} (dB) + G_{PA} (dB) - 1 dB \quad (2.7)$$

In the ADS simulation, the P1dB values of 3 dB, 5 dB and 10 dB are applied to the PAs. The simulation result of the beat spectrum is shown in Fig. 2.14. The expected beat frequency is 26.6 MHz with a normalized amplitude of 0 dB. However, it is observed that P1dB values of 3 dB and 5 dB results in normalized amplitude values of -8 dB and -3 dB, respectively. It is also observed that an additional beat frequency at 53.4 MHz begins to emerge as P1dB drops. This nonlinearity creates false alarm, decreases Rx sensitivity and DR. Nevertheless, this nonlinearity can be reduced by operating the amplifier in the linear region.

## 2.6 LNA Parametrization

The LNA is used to amplify the received signal to improve the Rx SNR and sensitivity. The cascode inductively degenerated common source is a common LNA topology, in which the low NF is achieved by using an inductor for impedance matching and the improved gain and bandwidth is achieved by the cascode configuration. In general, it is not possible for an amplifier to simultaneously achieve maximum gain and minimum NF, due to the trade-offs enforced by the transistor drain current settings [58]. This can also be visualized by plotting the constant NF and gain circles on the smith chart. Similar to the above, since nonlinear components are also used for a LNA, LNAs have its imperfections that disturb the LNA output signal from its ideal behaviour. Since the LNA is the first building block of the Rx chain, its noise performance will dominate the overall system noise performance. Therefore, the key parameter under study for the LNA output signal is NF.

The NF of a cascaded Rx chain can be represented by [42]

$$NF (dB) = 10 \log(F_n) = 10 \log_{10} \left( F_1 + \frac{F_2 - 1}{G_1} + \frac{F_3 - 1}{G_1 G_2} + \dots + \frac{F_n - 1}{G_1 G_2 \dots G_n} \right) \quad (2.8)$$

where  $F$  is the NF in linear scale. In the ADS simulation, the NF values of 1 dB, 3 dB and 5 dB are applied to the LNA. The simulation result of the beat spectrum is shown in Fig. 2.15. The expected and observed beat frequencies are both at 26.6 MHz and the NFL increases with NF. This nonlinearity decreases the Rx sensitivity and DR. Nevertheless, this nonlinearity can be reduced with a low NF LNA, clean power supply, adequate RF grounding and short RF tracks.

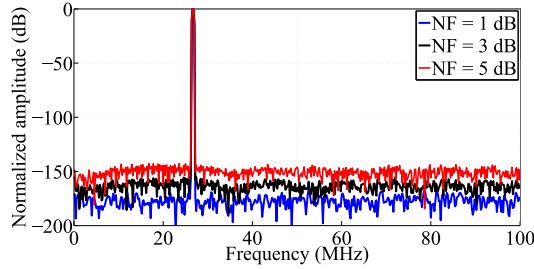


Figure 2.15: Radar simulation with NF varied for the LNA: Beat spectrum.

## 2.7 MIX Parametrization

MIX is used to down-convert the received signal to output a baseband beat signal. The common MIX topologies are the single-balanced and the double-balanced. At the core of most MIXs is an active nonlinear component (e.g., diode or transistor) used to provide frequency conversion by multiplying the received signal at the RF port with a copy of the transmitted signal at the LO port. The output of a mixer can be represented by [42]

$$f_{IF}^{beat} = \pm m f_{RF} \pm n f_{LO} \quad (2.9)$$

where  $m$  and  $n$  are integers. Since nonlinear components are used, MIXs have its imperfections that disturb the beat signal from the ideal behaviour. Therefore, the key parameters under study for the beat signal are: conversion loss (CL) and minimum LO drive level.

The beat signal can be affected by CL due to MIX topology, LO drive level and frequency pulling. The CL can be represented by [42]

$$CL (dB) = 10 \log_{10} \left( \frac{P_{RF}}{P_{IF}} \right) \quad (2.10)$$

In the ADS simulation, the CL values of 3 dB, 6 dB and 10 dB are applied to the MIX. The simulation result of the beat spectrum is shown in Fig. 2.16. The expected beat frequency is 26.6 MHz with a normalized amplitude of 0 dB; however, it is observed that the ampli-

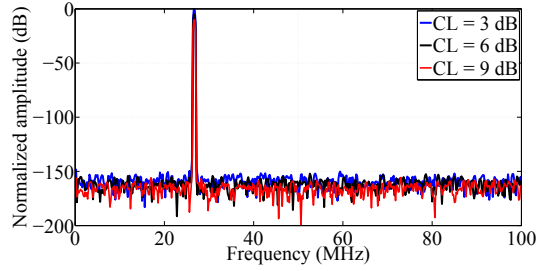


Figure 2.16: Radar simulation with CL varied for the MIX: Beat spectrum.

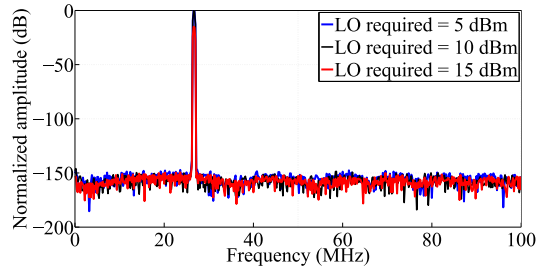


Figure 2.17: Radar simulation with minimum LO drive level varied for the MIX: Beat spectrum.

tude level decreases with increasing CL. This nonlinearity degrades Rx sensitivity and DR. Nevertheless, this nonlinearity can be reduced with a double-balanced topology, with proper the minimum LO drive level and with proper load terminations.

The beat signal can be affected by minimum LO drive level. The minimum LO drive level is the minimum power required to properly switch the active nonlinear components fully on and off to achieve minimum signal distortion. In the ADS simulation, the minimum LO drive levels of 5 dBm, 10 dBm and 15 dBm are applied to the MIX, while the LO signal amplitude is fixed at 10 dBm. The simulation result of the beat spectrum is shown in Fig. 2.17. The expected beat frequency is 26.6 MHz with a normalized amplitude of 0 dB; however, it is observed that the amplitude level decreases when the minimum LO drive level increases to 15 dBm. This nonlinearity degrades the Rx sensitivity and DR. Nevertheless, this nonlinearity can be reduced with sufficient LO drive level.

Table 2.5: Relation of Component Parameters and System Performances

<b>System Performance</b>	<b>Component Parameters</b>
Rx Sensitivity	Ramp circuit: voltage ripple VCO: phase noise, power output fluctuation, 2nd harmonics PA: P1dB LNA: NF MIX: CL, minimum LO drive level
DR	Ramp circuit: voltage ripple VCO: phase noise, power output fluctuation, 2nd harmonics PA: P1dB LNA: NF MIX: CL, minimum LO drive level
False Alarm	Ramp circuit: aperiodic sweep, sloped falling edge VCO: 2nd harmonics PA: P1dB
Range Accuracy	Ramp circuit: voltage ripple and voltage clamp VCO: phase noise
Range Resolution	Ramp circuit: voltage ripple VCO: phase noise
Sampling Rate	Ramp circuit: aperiodic sweep, voltage clamp, sloped falling edge

## 2.8 Summary of the Study

Table 2.5 summarizes the relation of individual component parameters on the overall system performance. This provides an understanding and guideline for the selection of components, and the system diagnosis to achieve a better system design.

## 2.9 Nonideal FMCW Radar System Simulation

A nonideal homodyne FMCW radar system is simulated, as shown in Fig. 2.18(a). The nonlinearities and/or nonideal component behaviours are included, using off-the-shelf component specifications, as shown in Table. 2.6. The system parameters for the simulation are sweep period of 5  $\mu$ s, sweep frequency of 2 to 4 GHz, phase noise of -65 dBc/Hz at 1 kHz, -89 dBc/Hz at 10 kHz, -110 dBc/Hz at 100 kHz and second harmonics of -15 dBc. The Tx path consists of two VtPulses, two VCOs, a power combiner, two power dividers and a BPF. A description of the Tx path is as follows: First, a Vtpulse generates a noise free ramp signal, while the other Vtpulse generates a noisy ramp signal with a 0.1 mV noise source to include the effects of phase noise and voltage ripple. Then the output of the two VCOs are combined to include the effects of second harmonics. Subsequently, a BPF is used to shape the chirp spectrum to include the effects of power output fluctuations. Finally, the chirp signal is passed to a power divider, where half of the power is coupled to PA1 for signal amplification before it is radiated by the Tx antenna, and the other half is passed to PA2 for signal amplification before it reaches the LO port of the MIXs. The target scene consists of two attenuators and two time delay components. A description of the two-target scene is as follows: The first point target at  $R_1 = 5$  m is represented by a FSPL of 56 dB and a time delay of 33.3 ns. The second point target is at  $R_2 = R_1 + \Delta R$ , where  $\Delta R$  is varied to determine the range resolution for RCS ratios of 0.1, 0.2, 0.5 and 1. The Rx path consists of two MIXs, two LNAs and a power combiner. A description of the Rx path is as follows: First, the two MIXs and two LNAs are used to separately down-convert the Rx signals from each of the targets. Then a power combiner is used to combine the beat signals. The simulation result of the beat spectrum is shown in Fig. 2.18(b). It is observed that target ranges of 5 m and 5.4 m results in beat frequencies of 13.3 MHz and 14.4 MHz, respectively. This represents that the minimum range resolution, given the system and simulation parameters, is 40 cm. Although the theoretical resolution should be 7.5 cm, the bottleneck lies in the number of simulation points (or computational time), which translates to a frequency resolution of 1.07

MHz. Then the simulation result of the beat spectrum with variation in RCS ratio is shown in Fig. 2.18(c). It is observed that the minimum range resolution of 0.4 m is only achievable for a RCS ratio  $\geq 0.2$ .

The ADS simulation study led to the design and selection of the radar components.

Table 2.6: Component Parameters for the Nonideal FMCW Radar System

Component	Parameter	Value
Ramp	Sweep period	5 $\mu$ s
	Sweep voltage	0-20 V
	Falling edge	0.001 $\mu$ s
	Voltage ripple	0.001 mV
VCO(see Appendix A)	Sweep frequency	2-4 GHz
	Power output	5 dBm -65 dBc @ 1 kHz
	Phase noise	-89 dBc @ 10 kHz -110 dBc @ 100 kHz
PA(see Appendix A)	Gain	20 dB
	$S_{11}$	30 dB
	$S_{22}$	20 dB
	NF	4 dB
	P1dB	20 dBm
LNA(see Appendix A)	Gain	14 dB
	$S_{11}$	15 dB
	$S_{22}$	21 dB
	NF	3 dB
	P1dB	12 dBm
MIX(see Appendix A)	CL	-6 dB
	$S_{11}^{LO}$	9.5 dB
	$S_{11}^{RF}$	9.5 dB
	NF	6 dB
	min. LO Drive	10 dBm

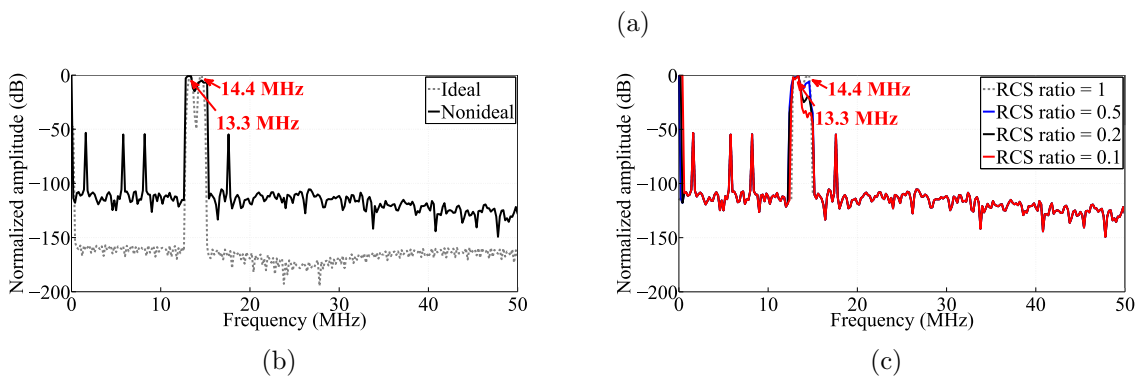
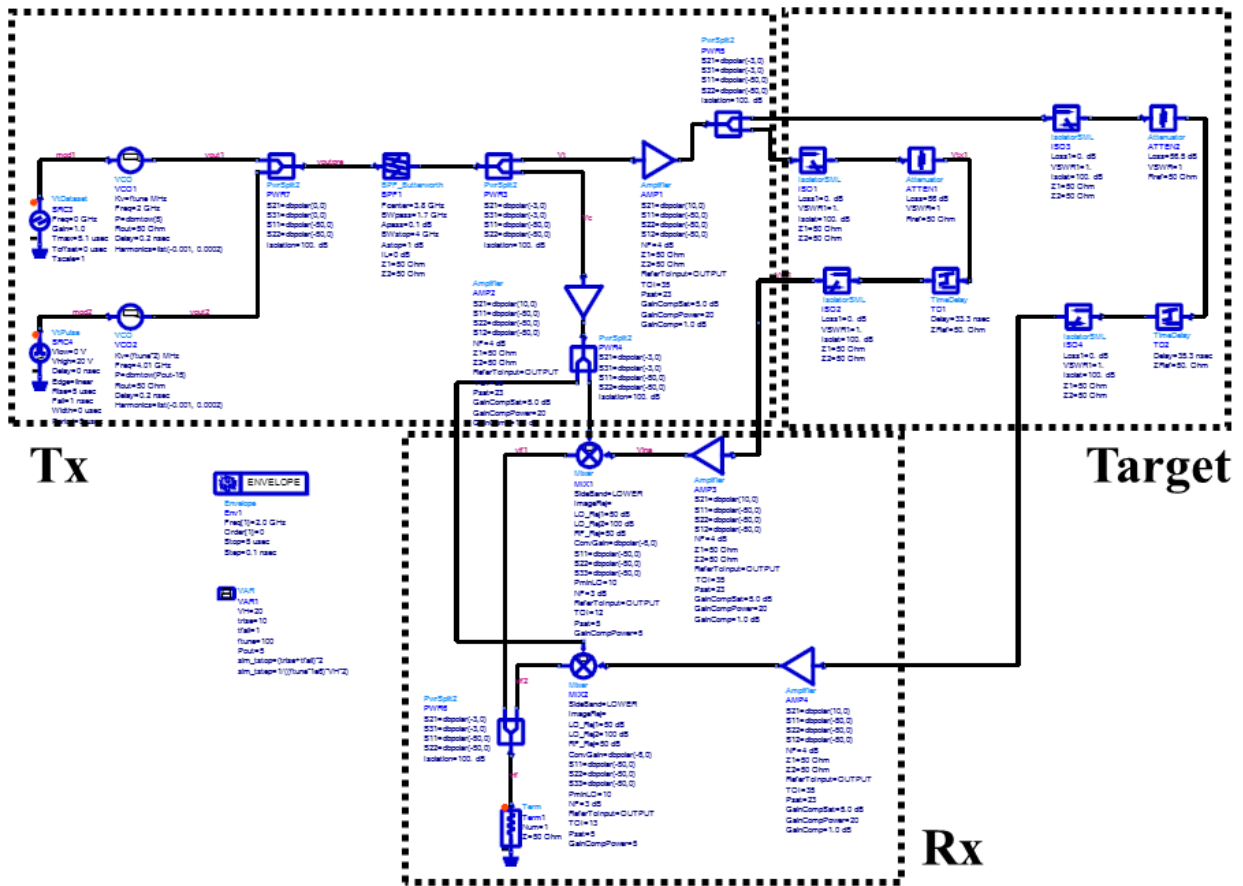


Figure 2.18: Nonideal FMCW radar simulation: (a) Schematic. (b) Beat spectrum. (c) Beat spectrum with variation in RCS ratio.

# Chapter 3

## Hardware Design

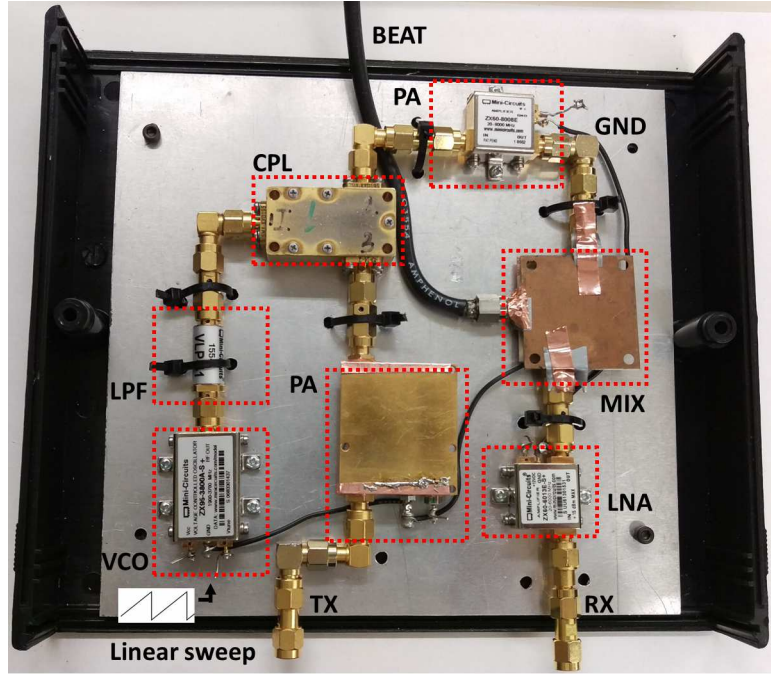
### 3.1 Overview of FMCW Radar System

An S-band homodyne FMCW radar system, using off-the-shelf components, is designed for near distance target imaging. A photograph and block diagram of the FMCW radar system are shown in Fig. 3.1. The radar system can be categorized into three sub-parts: the Tx signal chain, the Rx signal chain and the baseband signal processing unit. This chapter presents the hardware design, the choice of components and the component measurement results.

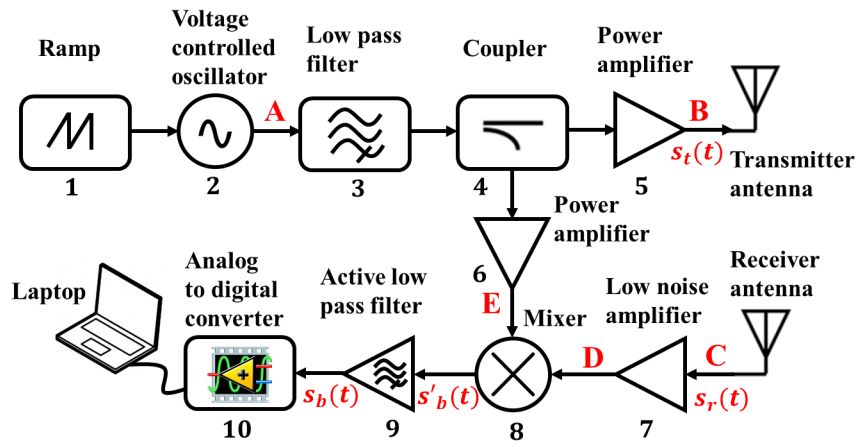
### 3.2 Tx Signal Chain

#### 3.2.1 Ramp Circuit

The ramp circuit provides a linear voltage sweep for the VCO tuning port. A schematic, PCB layout and photograph of the ramp circuit are shown in Fig. 3.2 and 3.3. The main components of the ramp circuit are timer IC, transistor and op-amp. A description of the ramp circuit is as follows: The 555-timer IC is configured in astable mode, which generates a continuous train of pulses without a continuous trigger. Next, the signal is passed to a



(a)



(b)

Figure 3.1: (a) Photograph, and (b) block diagram of the S-band FMCW hardware.

PNP transistor, which controls the period of the sweep by varying the potentiometer at the emitter. Then the signal is passed to an inverting op-amp, which controls the amplitude of the sweep by varying the potentiometer at the output. Finally, the signal is passed to another inverting op-amp, which controls the DC-offset of the sweep by varying the potentiometer at the positive rail. This ramp circuit provides flexibility to adjust the period, amplitude and DC-offset of the sweep, which translates to the control of tuning speed and frequency

Table 3.1: Ramp Signal Measurement Results

<b>Sweep Period</b>	10 $\mu$ s to 35 ms
<b>Amplitude</b>	0 V to 21 V
<b>DC-offset</b>	$\pm 3$ V

range of the VCO output signal. The measured ramp signal is illustrated in Fig. 3.4, while the measurement results are presented in Table. 3.1.

### 3.2.2 VCO

The ramp circuit is used with the VCO to generate a chirp signal. The VCO is an off-the-shelf component selected with main considerations for frequency range, power output, phase noise and cost. The different VCOs capable of S-band operation are presented in Table. 3.2. After a performance comparison, the VCO ROS-3800-119+ from Minicircuits was selected (see Appendix A). Then the VCO performance is characterized with a spectrum analyzer (SA) Agilent 8562EC and the measurement results are shown in Fig. 3.5, in which polynomial interpolation is applied. The SSB phase noise measurement result shown in Fig. 3.5(a) is obtained using the direct spectrum method, in which the VCO is tuned to a single frequency and a correction factor is applied to the amplitude of the SA. The correction factor is applied in two steps: First, normalize the resolution bandwidth (RBW) filter to 1 Hz bandwidth. Second, account for the RBW filter’s noise bandwidth. Consequently, the power level read from the SA can be used to express the phase noise power level represented by [59]

$$\mathcal{L}_{1Hz}(f) (dB) = P_{spectrum} (dB) - 10 \log(RBW_{norm} \cdot 1.0575) \quad (3.1)$$

where  $P_{spectrum}$  is the power level in dB read from the SA and 1.0575 is the RBW filter noise bandwidth specific to the SA. The voltage tuning measurement result is shown in Fig. 3.5(d) and can be curve fitted in MATLAB, using polynomial interpolation, to provide an equation

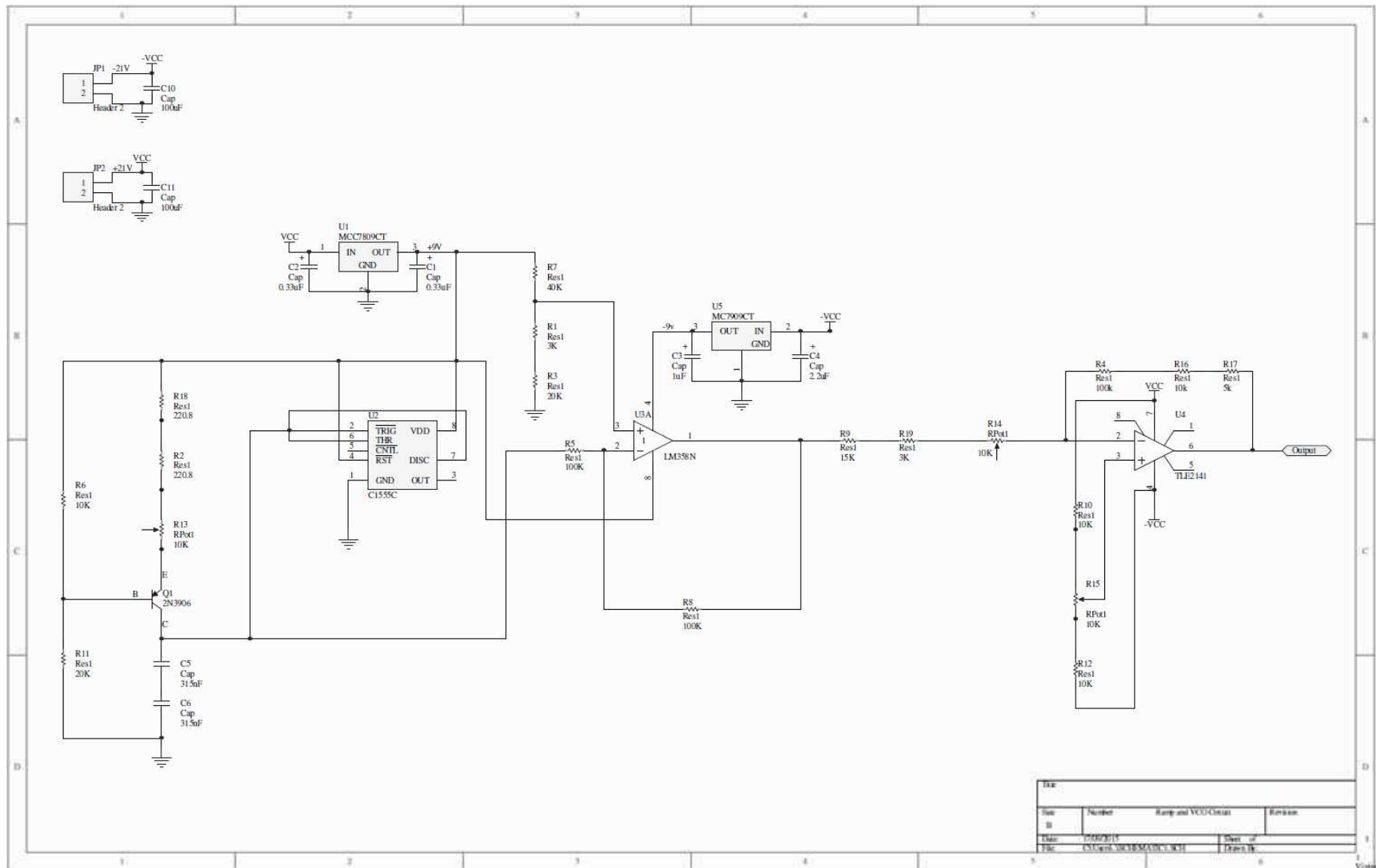


Figure 3.2: Ramp circuit schematic.

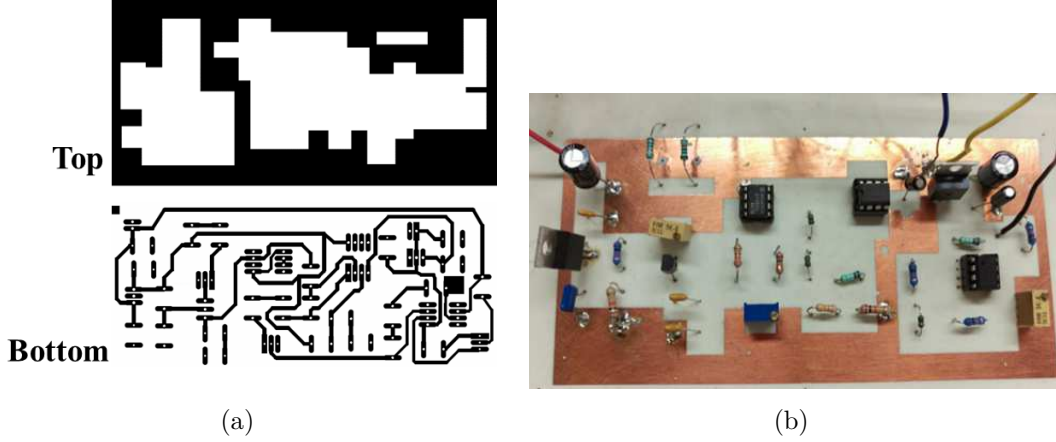


Figure 3.3: Ramp circuit: (a) PCB Layout. (b) Photograph.

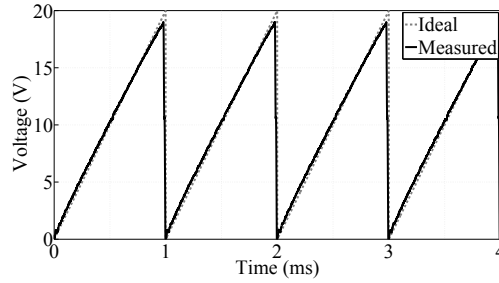


Figure 3.4: Ramp circuit measurement results.

Table 3.2: Comparison of Different VCOs Capable of S-Band Operation.

Manufacturer	Name	Freq. (GHz)	Pout (dBm)	Phase Noise (dBc)	Price
OmniYIG	YOM20	1-4	13	-90 @ 10 kHz	\$1450
Gigatronics	LPO0205	2-5	11	-104 @ 10 kHz	\$1950
Synergy	DCYS2004	2-4	1	-90 @ 10 kHz	\$100
Micronetics	MW500	2-4	5	-82 @ 10 kHz	\$70
Minicircuits	ROS3800	1.9-3.7	5	-89 @ 10 kHz	\$30

for the VCO tuning characteristics, which can be represented by

$$VCO_0(f) = -2.21 \times 10^{-3}V_t^2 + 0.15V_t + 1.73 \quad (3.2)$$

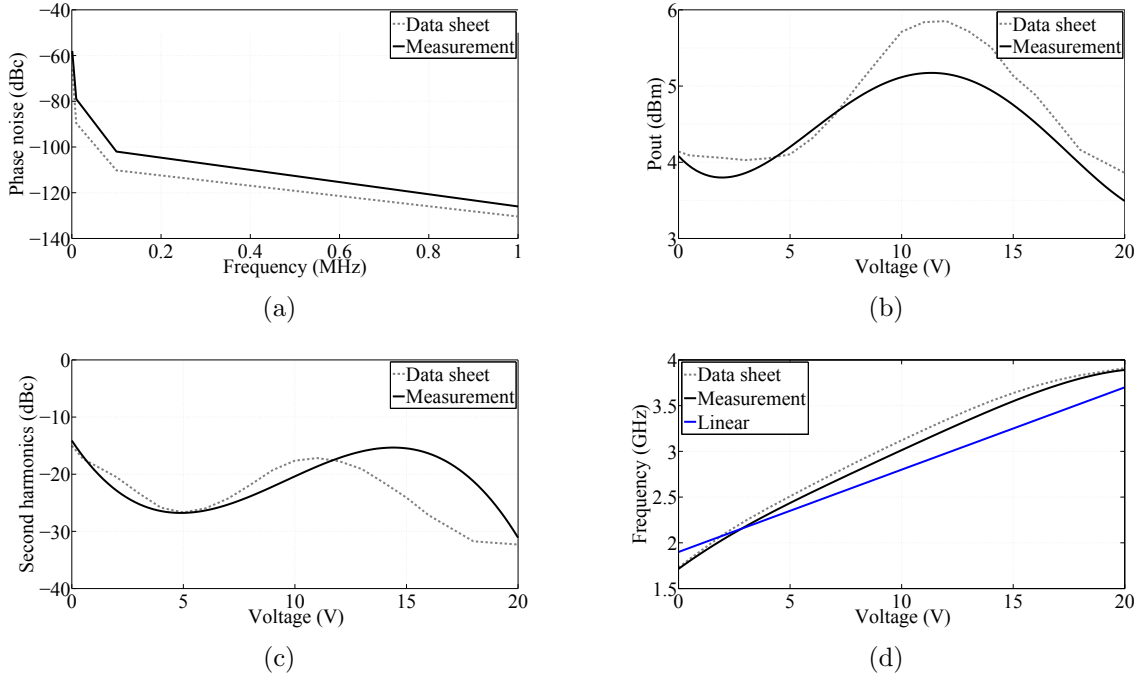


Figure 3.5: VCO measurement results: (a) Phase noise. (b) Power output. (c) Second harmonics. (d) Tuning characteristic.

It can be observed from (Eq. 3.2) that the slope of the VCO tuning curve is not a constant value due to the square term.

### 3.2.3 LPF

The LPF is used to remove the second harmonics generated by a VCO. The main specifications of a LPF are cut-off frequency and insertion loss. A stepped-impedance microstrip LPF is presented, as shown in Fig. 3.6. The LPF design is a three step process: First, select a substrate material (RO4003C:  $\epsilon_r = 3.38$ ,  $h = 0.813$  mm,  $t = 0.038$  mm,  $\sigma = 5.8 \times 10^7$  and  $\tan \delta = 0.0027$ ) and calculate the design dimensions [60]. Second, simulate the design using ADS. Third, check the design with a full-wave simulator such as HFSS. The final LPF dimensions are:  $W_1 = 1.13$  mm,  $W_2 = 3.85$  mm,  $W_3 = 0.39$  mm,  $L_1 = 8$  mm,  $L_2 = 0.64$  mm,  $L_3 = 4.24$  mm,  $L_4 = 4.3$  mm,  $L_5 = 5.48$  mm,  $L_6 = 5.29$  mm,  $L_7 = 5.48$  mm,  $L_8 = 5.65$  mm,  $L_9 = 5$  mm, and  $L_{10} = 3.15$  mm. The LPF performance is shown in Fig. 3.7(a). However, to achieve a more compact design, an off-the-shelf LPF VLP-41 from Minicircuits

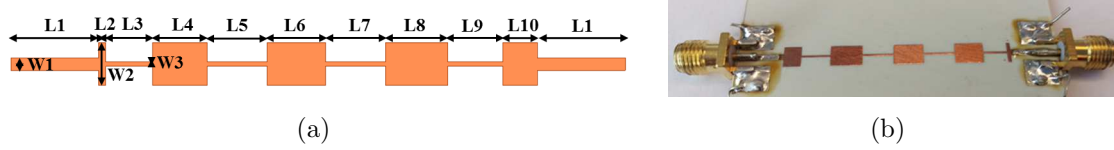


Figure 3.6: Stepped impedance LPF: (a) Schematic. (b) Photograph.

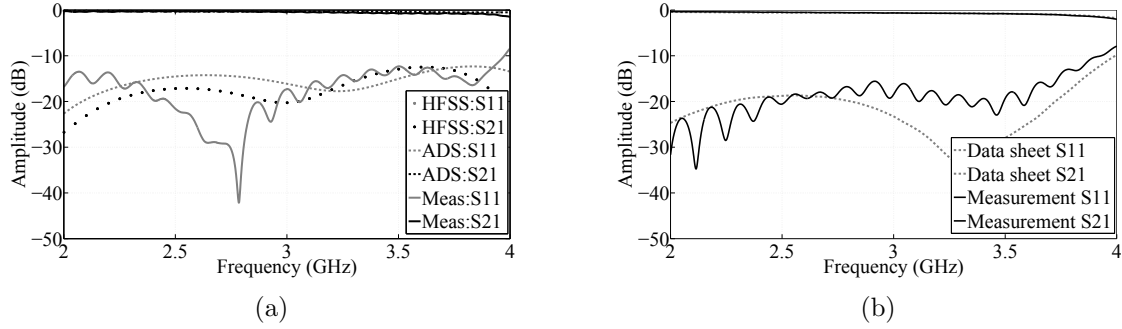


Figure 3.7: LPF results: (a) Stepped impedance. (b) LPF (VLP-41).

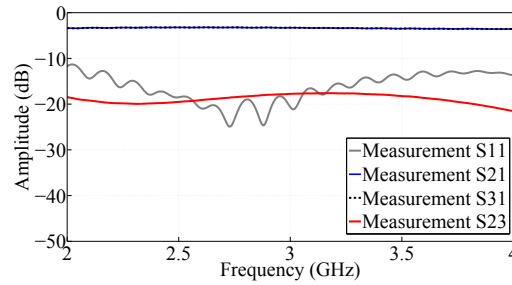


Figure 3.8: Coupler measurement results.

was selected (see Appendix A). The LPF performance is characterized with a vector network analyzer (VNA) Agilent E8362B and the measurement results are shown in Fig. 3.7(b).

### 3.2.4 Coupler

The coupler is used to couple a copy of the VCO output signal to the MIX LO port. The coupler is an off-the-shelf component selected with main considerations for frequency range, coupling and isolation. The measurement results obtained with a VNA is illustrated in Fig. 3.8.

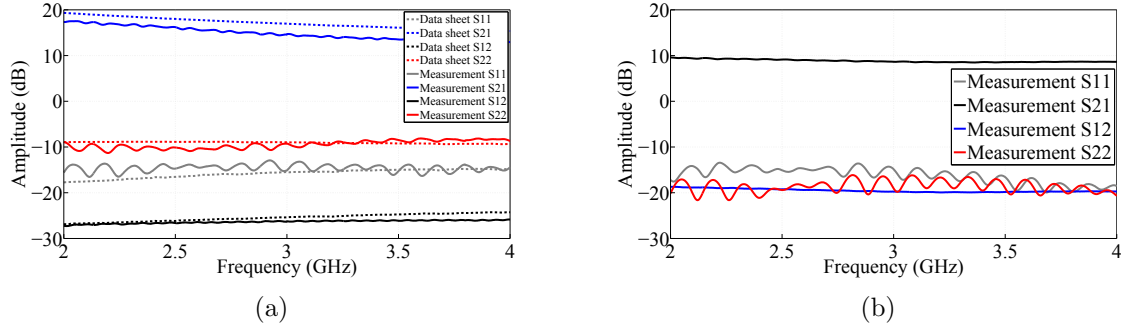


Figure 3.9: PA measurement results: (a) GALI-84+. (b) ZX60-8008E.

### 3.2.5 PA

The PA is used to amplify the signal to provide enough power for transmission, and/or to meet the minimum LO drive level for the MIX. The PA is an off-the-shelf component selected with main considerations for frequency range, gain and P1dB. The PAs GALI-84+ and ZX60-8008E from Minicircuits was selected (see Appendix A). Then the PAs performances are characterized with a VNA and the measurement results are shown in Fig. 3.9. It is worth to note that the manufacturer website did not provide the S-parameter measurements for PA ZX60-8008E. A K-Delta test [42] verifies that both PAs are unconditionally stable across the S-band.

## 3.3 Rx Signal Chain

### 3.3.1 LNA

The LNA is used to amplify the received signal to improve the Rx SNR and sensitivity. The LNA is an off-the-shelf component selected with main considerations for frequency range, gain and NF. The LNA ZX60-6013S from Minicircuits was selected (see Appendix A). Then the LNA performance is characterized with a VNA and the measurement results are shown in Fig. 3.10. The NF measurement is obtained using the gain method, in which the LNA is

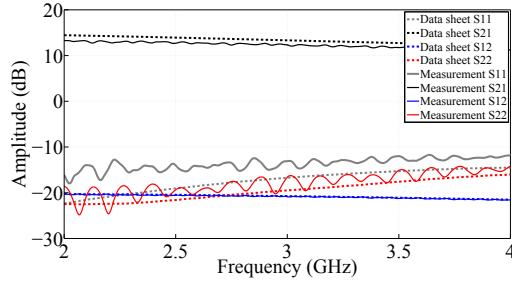


Figure 3.10: LNA measurement result.

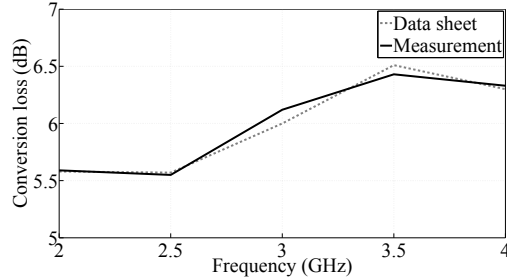


Figure 3.11: MIX measurement result.

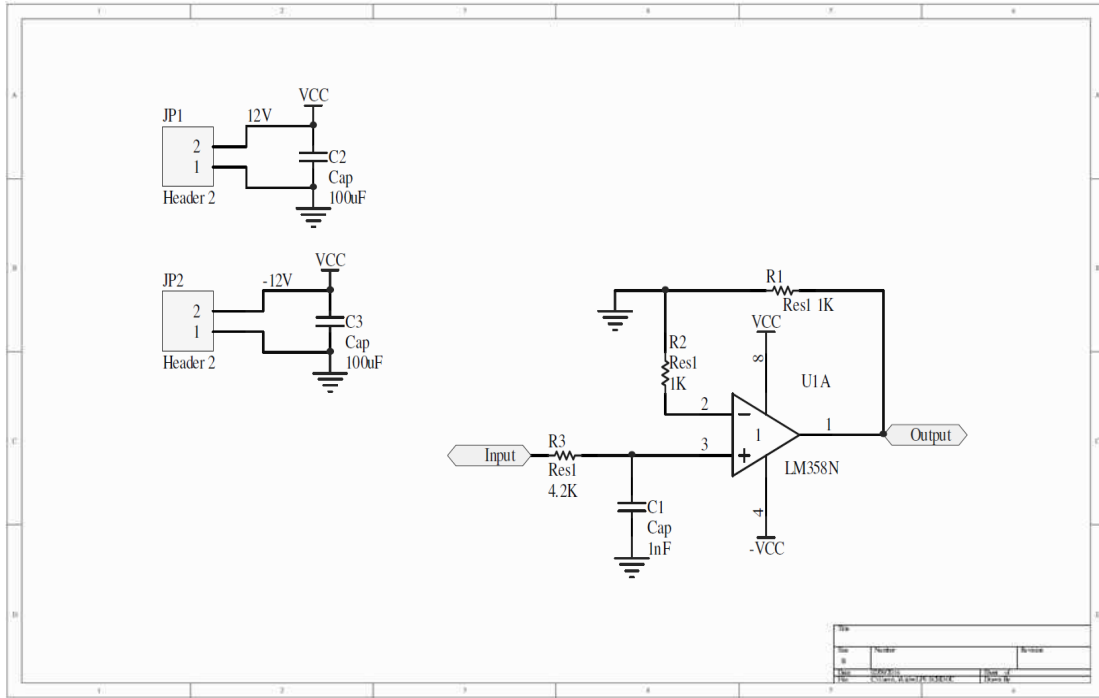
biased to operate in the linear region, the input of the LNA is left open and the output is connected to the SA. A maximum video averaging of 512 is applied to the SA to reduce the NFL. Then the power level read from the SA can be represented by [59]

$$NF (dB) = P_{spectrum} (dB) - (DANL (dB) + 10 \log(RBW) + G_{LNA} (dB)) \quad (3.3)$$

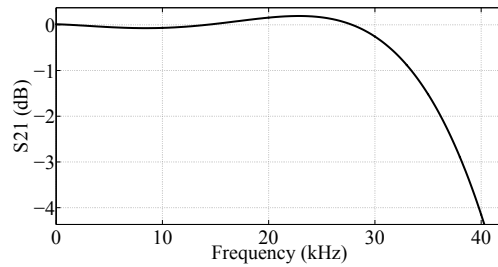
where  $DANL$  is the displayed average noise level in dB of the SA. The NF measured at 2 GHz, 3 GHz and 4 GHz are 3.13 dB, 3.24 dB and 3.18 dB, respectively. A K-Delta test [42] verifies that the LNA is unconditionally stable across the S-band.

### 3.3.2 MIX

The MIX is used to down-convert the received signal to generate a baseband beat signal. The MIX is an off-the-shelf component with main considerations for frequency range, conversion loss and minimum LO drive level. The MIX MCA1T-60LH+ from Minicircuits was



(a)



(b)

Figure 3.12: Active LPF: (a) Schematic. (b) Measurement results.

selected (see Appendix A). Then the MIX performance is characterized with a SA and the measurement result is shown in Fig. 3.11.

### 3.3.3 Active LPF

The MIX IF output is immediately followed by a first-order active LPF to prevent signal aliasing and to increase SNR. The LPF has a cut-off frequency at 38 kHz and a voltage gain of 6 dB. The schematic and measurement result are shown in Fig. 3.12.



Figure 3.13: LabVIEW interface.

## 3.4 Baseband Signal Processing Unit

### 3.4.1 ADC

The ADC National Instrument USB-6351 is used to acquire, digitize and save the beat signal. The main specifications of the ADC are sample rate of 1250 KSPS, 16 bit resolution, input voltage range of  $\pm 10$  V and 24 digital I/O channels. The periodicity of the ramp signal serves as a reference clock for the ADC (at channel AI1) that initializes the recording of the beat signal (at channel AI0); therefore the Tx and Rx are synchronized. Synchronization is necessary to prevent differences in the initial position of record to accumulate that will misalign the timing of the beat signal. Such misalignment translates to frequency shift and target range inaccuracy. An internal timer is used to start the data acquisition after 5 seconds has passed. This avoids the instability during system start-up to skew the measurement. A set number of data points is saved for each data acquisition. This ensures the same file size is saved for each measurement. A time stamp is applied for each data acquisition. This helps to organize the data from each measurement. The LabVIEW interface and schematic are shown in Fig. 3.13 and 3.14.

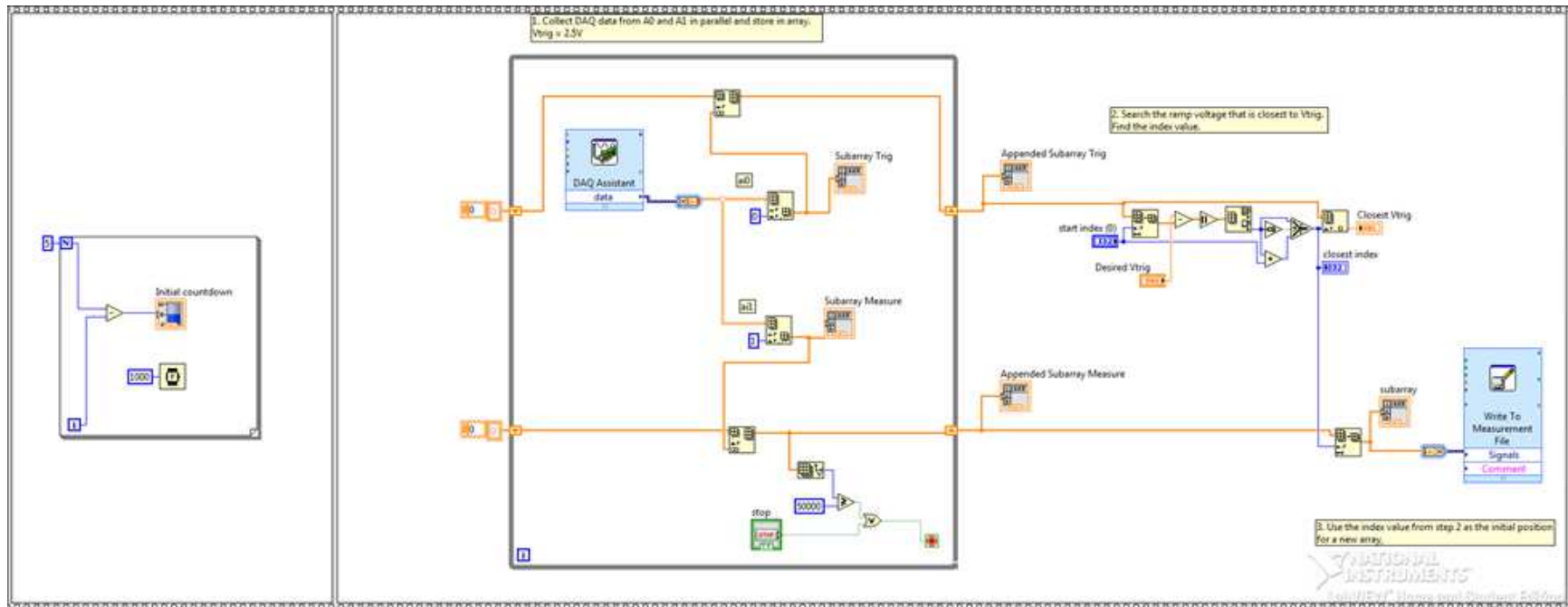


Figure 3.14: LabVIEW schematic.

## 3.5 Overall System Specifications

The designed radar system is shown in Fig. 3.1(a). The components used for the designed S-band FMCW radar are numerically labelled in Fig. 3.1(b), with the corresponding specifications shown in Table. 3.3. The radar system can be divided into three parts: the Tx signal chain, the Rx signal chain and the baseband signal processing unit. The Tx signal chain mainly consists of a linear sweep circuit that generates a continuous ramp signal for the VCO tuning port. The designed radar system has a peak power of 40 mW (16 dBm). The Tx and Rx antennas are Vivaldi antennas [61], for which the antenna group delay is 3 ns. The Rx signal chain mainly consists of a LNA that amplifies the received signals before down-conversion by the mixer. The output of the mixer is a baseband beat signal that is then fed to an active LPF to prevent signal aliasing and to increase Rx sensitivity. For a system NF of 12 dB, the MDS is -116 dBm and the system DR is 111 dB. The baseband signal processing unit consists of an ADC and a PC running LabVIEW that digitizes the beat signal for further signal processing in MATLAB. The periodicity of the ramp signal serves as a reference clock for the ADC that initialize the recording of the beat signal; therefore the Tx and Rx are synchronized. This radar has an alias-free operating range of 0 to 3.17 m, with an ideal range resolution of 8.33 cm. In comparison, an UWB impulse radar will require a pulse width of 0.55 ns and an ADC sampling rate of at least 3.6 GSPS to achieve the same resolution performance as the FMCW radar. The designed system specifications are summarized in Table. 3.4.

### 3.5.1 Time Domain Characterization

A complete system characterization is performed in the time domain with a real time oscilloscope Agilent MSOX-6004A. The chirp signal is acquired at locations A, B, C, D and E, as shown in 3.1(b). Then the signal distortion introduced by each component and relative to the VCO output signal is computed. The main specifications of the oscilloscope

Table 3.3: Specifications of the FMCW Radar Components

Component number	Description	Component specifications
1	Ramp	$T_{ramp} = 1 \text{ ms}$ , $V_{ramp} = 0.5 - 20 \text{ V}$ .
2	VCO	$B = 1.9 - 3.7 \text{ GHz}$ , $\psi_{noise} = \psi_{noise1}^*$ .
3	LPF	$B = 1.5 - 4 \text{ GHz}$ , $S_{21} = -0.5 \text{ dB}$ .
4	Coupler	$B = 1.5 - 4 \text{ GHz}$ , $S_{21} = S_{31} = -3 \text{ dB}$ , $S_{23} = -20 \text{ dB}$ .
5	Amplifier	$B = 0 - 6 \text{ GHz}$ , $S_{21} = 17 \text{ dB}$ , $IP1 = 20 \text{ dBm}$ , $NF = 4.5 \text{ dB}$ .
6	Amplifier	$B = 0 - 8 \text{ GHz}$ , $S_{21} = 10 \text{ dB}$ , $IP1 = 10 \text{ dBm}$ , $NF = 4.1 \text{ dB}$ .
7	LNA	$B = 0 - 6 \text{ GHz}$ , $S_{21} = 14 \text{ dB}$ , $IP1 = 13 \text{ dBm}$ , $NF = 2 \text{ dB}$ .
8	Mixer	$B = 1.7 - 6 \text{ GHz}$ , $Level = +10 \text{ dBm}$ , $ConversionLoss = -6 \text{ dB}$ .
9	Active LPF	$B = 0 - 38 \text{ kHz}$ , $S_{21} = 6 \text{ dB}$ .
10	ADC	$f_{sample} = 1250 \text{ KSPS}$ , $Resolution = 16 \text{ bit}$ .

$\psi_{noise1}^* = -65 \text{ dBc/Hz @ 1 kHz}$ ,  $-89 \text{ dBc/Hz @ 10 kHz}$ ,  $-110 \text{ dBc/Hz @ 100 kHz}$ .

Table 3.4: Specifications of the FMCW Radar System

Operating frequency	1.9 - 3.7 GHz
Modulation period	1 ms
Modulation waveform	Sawtooth
Pulse repetition frequency	1 kHz
Transmitted power	16 dBm
Antenna gain	3.8 dBi
Beamwidth (azimuth/elevation)	80° / 180°
Operating range	0 - 3.17 m
Range resolution	8.33 cm

are maximum bandwidth of 6 GHz, maximum sampling rate of 20 GSPS and maximum waveform memory depth of 4 Mpts. In particular, the bottleneck is the waveform memory of the oscilloscope. Even though the oscilloscope specifies a high maximum sampling rate,

this does not mean that the oscilloscope will always sample at this rate. The oscilloscope's sampling rate is adjusted according to the signal duration and the waveform memory depth, which can be represented by

$$AcquisitionMemory = SignalDuration \times NyquistSamplingRate \quad (3.4)$$

In order to utilize a sampling rate of 20 GSPS, the signal time base is limited to 20  $\mu\text{s}/\text{div}$ , to capture a 200  $\mu\text{s}$  (20  $\mu\text{s}/\text{div} \times 10$  divisions) duration signal. For our radar system, the chirp signal sweeps from 1.8 to 3.7 GHz in 1 ms. Therefore, given the waveform memory depth of 4 Mpts, the oscilloscope's sampling rate needs to be adjusted to 4 GSPS in order to capture the entire chirp signal's duration in one frame. However, this does not satisfy the Nyquist sampling rate and results in signal aliasing. In order to satisfy the Nyquist sampling rate, a sampling rate of at least 7.4 GSPS is required. However, given a waveform memory of 4 Mpts, the chirp signal duration is limited to 0.5 ms. In other words, the ramp sweep period is adjusted to 0.5 ms, the voltage sweep is adjusted to sweep from 0 to 10 V and the new VCO output frequency sweeps from 1.8 to 2.75 GHz. Then the time domain characterization is performed with two steps: First, the chirp signal with duration 0.5 ms is consistently acquired throughout the system at locations shown in Fig. 3.1(b). Fig. 3.15 shows an overview and zoom into the measured time domain chirp signals with a duration of 0.02  $\mu\text{s}$  starting at 60  $\mu\text{s}$ . Fig. 3.16 shows an overview and zoom into the measured time domain chirp signal, which verifies the change in frequency over time. Second, match filtering is applied to find the correlation value, which compares the signal distortion added to the VCO output chirp signal at location A and can be represented by [62]

$$s_m(t) = s_{VCO,A}(t) \otimes s_{loc}(-t)^* \quad (3.5)$$

where  $s_{VCO,A}(t)$  is the pulse measured at location A,  $s_{loc}(t)$  is the pulse measured at various locations throughout the system, and  $\otimes$  and  $*$  are the time-domain convolution and

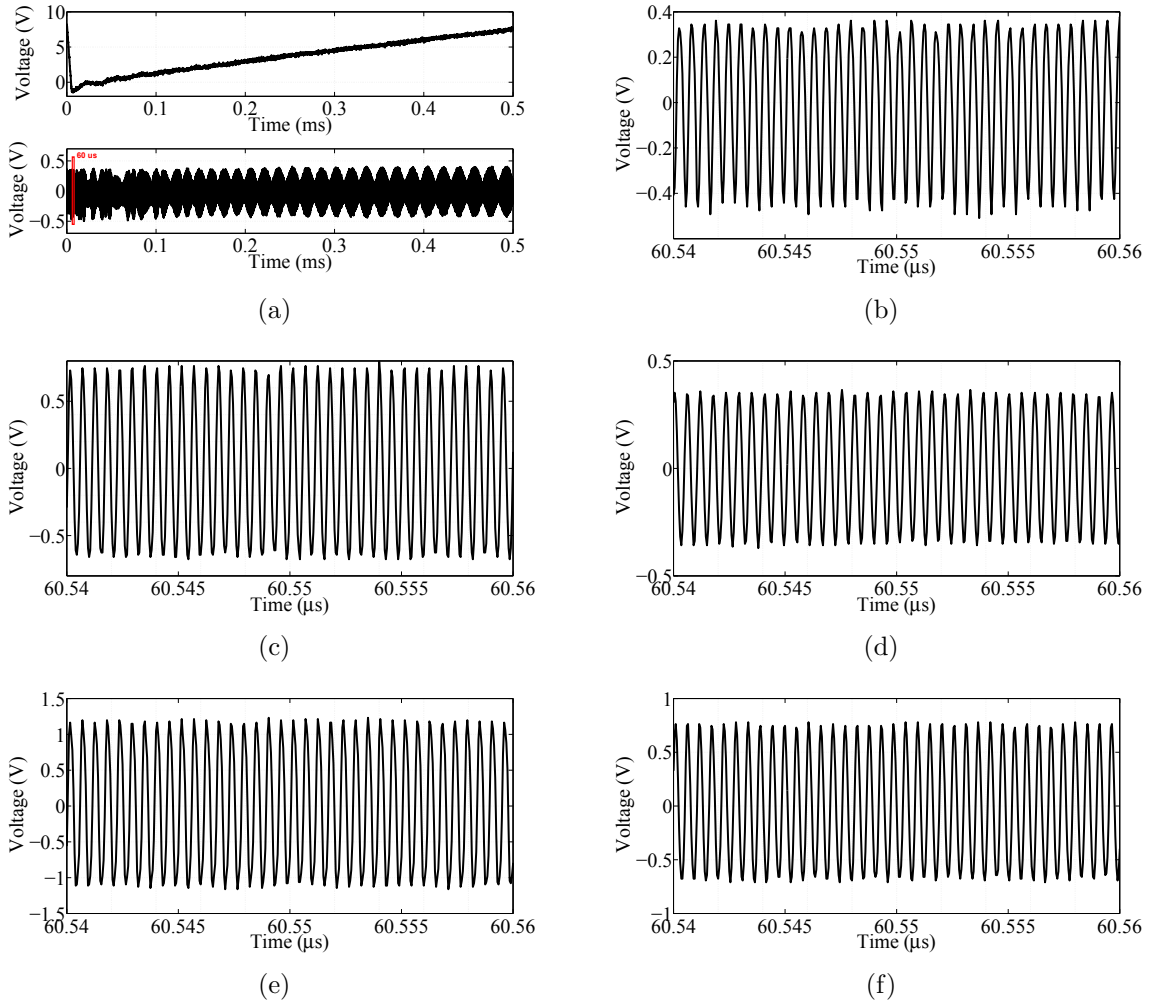


Figure 3.15: Time domain chirp signal: (a) Overview. (b) Location A. (c) Location B. (d) Location C. (e) Location D. (f) Location E.

conjugate operators, respectively. The normalized cross-correlation values at locations B, C, D and E compared to the template signal at location A are 0.91, 0.85, 0.8 and 0.91, respectively. It can be observed that the pulses measured are very much correlated with the VCO output pulse.

The subsystems and system measurements characterized and validated the radar sensor performance.

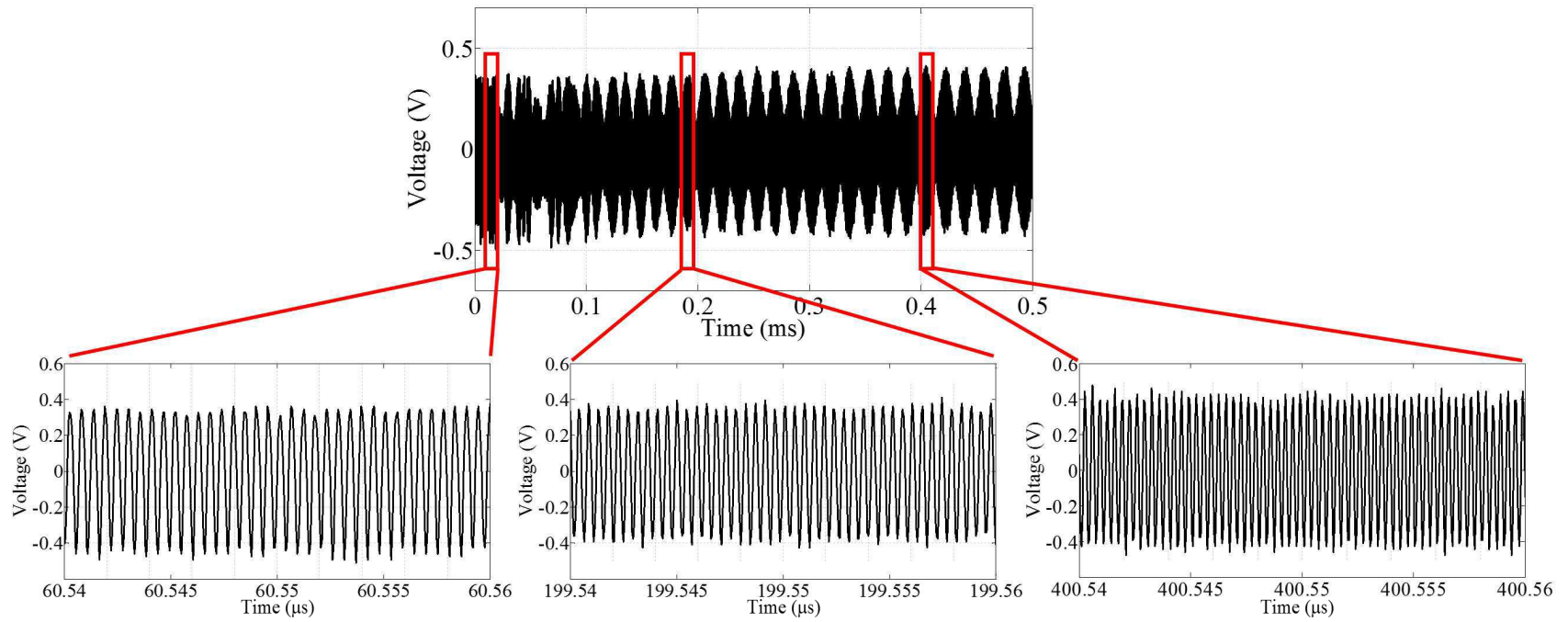


Figure 3.16: Time domain system measurement results to show changing frequency.

# Chapter 4

## Antenna Design

### 4.1 A Miniaturized Broadband Bow-Tie Antenna with Improved XP Performance

In this chapter, a modified broadband bow-tie antenna with low cross-polarization level and miniaturization is presented. The cross-polarization in both E- and H-planes are suppressed by defecting the antenna flares using rectangular slots. The proposed modified antenna demonstrated a cross-polarization improvement over  $\pm 120^\circ$  around the boresight from 2 to 5 GHz. In addition, an overall 23.5% of miniaturization compared to conventional bow-tie antenna is achieved. A tapered feed transition between microstrip-to-parallel stripline is designed to match 50 ohm SMA connector to the antenna flares. A prototype of the modified antenna is fabricated on RO4003 substrate ( $\epsilon_r = 3.38$ ,  $\tan\delta = 0.0027$ ,  $h = 0.813$  mm), and its performance is experimentally studied. The antennas characteristics including return loss, gain and radiation pattern are measured, along with the time domain characteristics, and showed reasonable agreement with the simulated results.

## 4.2 Introduction

In recent years, near-field ultra-wideband (UWB) radar imaging systems have attracted attention from both industry and academia for their advantages, such as excellent spatial resolution, and good penetration into dielectric materials. The non-destructive detection, localization, and imaging of objects can provide critical information for different applications. These applications range from rainfall monitoring [63], and buried object detection [64], to through-wall imaging [65], and breast cancer imaging [66]. An important performance metric for a radar imaging system is its resolution. Radar image resolution depends on both range and cross-range directions [32]. A more accurate measurement of the radar image resolution can be achieved by lowering the cross-polarization (XP) level of the antenna. In other words, suppressing radiation in the orthogonal direction results in cleaner signal and better image resolution [67].

An antenna that operates over 25% of fractional bandwidth is defined as UWB antenna [68]. Aperture antennas such as Vivaldi [69], TEM-Horn [70], and Bow-Tie [71] have shown to be good candidates for UWB radar imaging. Frequency range of the UWB imaging radars varies for application to application. Furthermore, in near-distance UWB imaging, due to the limited space, it often requires the use of miniaturized UWB antennas. The bow-tie antenna is one of the best candidates for UWB applications due to the appealing features such as planar structure, simple feed, low cost, easy-to-integrate, and decent pulse radiation characteristics. However, as the bow-tie antenna is a special class of patch antennas, it inherently exhibits high XP level [72]. In addition, it is well known that antenna miniaturization inherently compromises XP level and gain performance.

A number of bow-tie antennas with different geometries have been studied to reduce the size and lower the XP level for UWB applications. A double-sided bow-tie antenna with rectangular ( $0.92\lambda \times 0.92\lambda$ ) [73], rounded ( $0.91\lambda \times 0.91\lambda$ ) [74] and circular ( $0.65\lambda \times 1.3\lambda$ ) [75]

shaped radiators is used to cover the UWB frequency band. A T-shaped slot loaded bow-tie antenna ( $0.68\lambda \times 0.95\lambda \times 0.52\lambda$ ) fed through a microstrip balun is used to achieve UWB performance in [76]. A folded bow-tie antenna with interconnected arms and self-complementary geometry ( $0.34\lambda \times 0.34\lambda \times 0.61\lambda$ ) is proposed for UWB operation in [77]. A self-grounded bow-tie with seagull-over-sea configuration ( $\lambda \times 1.1\lambda$ ) is developed to obtain UWB performance in [78]. A CPW fed antenna with slots etched on the radiating arm ( $1.3\lambda \times 0.97\lambda$ ) is used for UWB operations in [79]. Although all the reported antennas display UWB performance, the proposed modified bow-tie antenna ( $0.64\lambda \times 0.41\lambda$ ) provides the smallest design, while improving the XP level especially at higher frequencies of the antenna operation. The  $\lambda$  is the effective wavelength, for the given substrate material, at the lowest operating frequency.

In this chapter, a modified bow-tie antenna is designed and its performance in both the frequency and time domains is measured. The geometry and location of rectangular slots have been proposed and optimized to direct the antenna surface currents which resulted in reduced XP level, and to achieve antenna size miniaturization.

### 4.3 Antenna Design

In this section, the configurations and dimensions of the proposed antenna are simulated and optimized using Ansoft HFSS. Since the bow-tie antenna is a derivative of the dipole antenna with broadband characteristics [72], the antenna design begins with the selection of radiating arms length, which is half-wavelength at a design frequency of 3 GHz, and flare angle of  $\theta = 70^\circ$ . Then the dimensions of the radiating arms are optimized using a complete parametric study approach, to satisfy the required UWB characteristics of return loss  $\leq -10$  dB in the band of operation, gain flatness, and constant group delay. A broadband

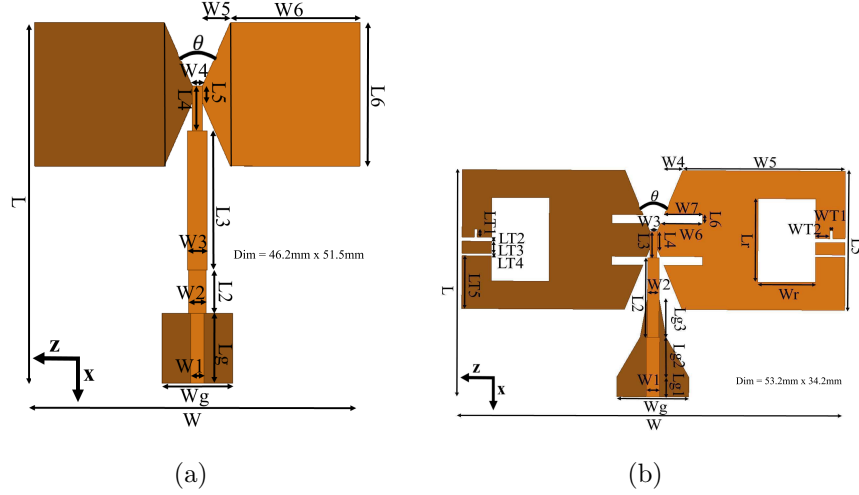


Figure 4.1: Antenna geometry: (a) conventional and (b) modified bow-tie antenna. Note: top layer-light brown and bottom layer-dark brown, and the dimensions are provided as part of the paragraph text.

balun forms the feedline for the radiating arms. The unbalanced end of the tapered balun is connected to a microstrip line with a width of  $W1 = 1.85$  mm, in order to match the  $50 \Omega$  coaxial line. The balanced end consists of a parallel plate transmission line, in which the lengths are determined using cavity model theory [80], and the widths are adjusted to match  $50 \Omega$  at the input port of the antenna. Furthermore, the proposed antenna design is scale-able to other frequency bands when all the dimensions are scaled by the same factor [72].

Fig. 4.1(a) depicts a conventional bow-tie antenna for the frequency range of 2 to 5 GHz with dimensions as follows:  $W = 46.2$  mm,  $L = 51.5$  mm,  $Wg = 10$  mm,  $Lg = 10$  mm,  $W1 = 1.85$  mm,  $W2 = 2.43$  mm,  $W3 = 2.83$  mm,  $W4 = 1.4$  mm,  $W5 = 4$  mm,  $W6 = 18.4$  mm,  $L2 = 6.2$  mm,  $L3 = 19.8$  mm,  $L4 = 6.4$  mm,  $L5 = 2.3$  mm, and  $L6 = 20.5$  mm. The dimensions of the antenna are  $0.57\lambda \times 0.63\lambda$ , with an overall area of  $0.359\lambda^2$ . Unlike the double-sided bow-tie antenna in [74], the proposed conventional antenna shown in Fig. 4.1(a) has a reduced ground plane for the microstrip feed. A ratio for microstrip width to ground plane width has been optimized for XP level improvement. In this approach, the XP level in the H-plane is reduced especially at 4 and 5 GHz, while E-plane maintains its low XP level.

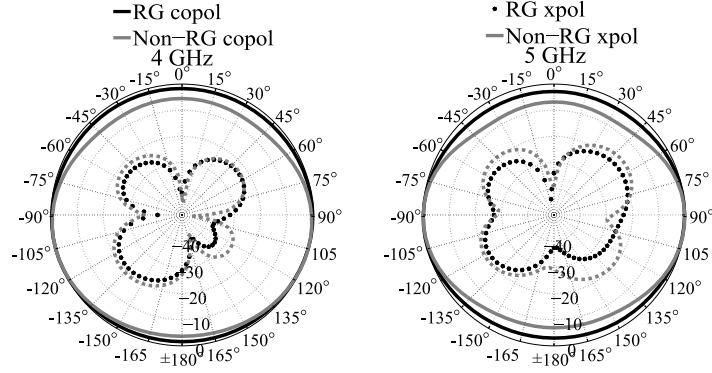


Figure 4.2: H-plane simulated radiation pattern of the conventional bow-tie antenna with reduced and non-reduced ground (RG) planes.

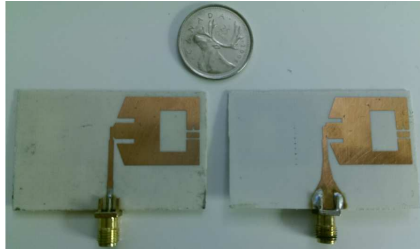


Figure 4.3: Photograph of the fabricated modified bow-tie antenna.

The effect of ground plane dimensions on XP level is demonstrated in Fig. 4.2. As it can be seen, reducing the ground plane maintains the E-plane XP levels, and improves the H-plane XP levels at frequencies 4 and 5 GHz.

Fig. 4.1(b) illustrates the modified bow-tie antenna with dimensions as follows:  $W = 53.2$  mm,  $L = 34.2$  mm,  $Wg = 10$  mm,  $L_{g1} = 3$  mm,  $L_{g2} = 6$  mm,  $L_{g3} = 5.9$  mm,  $W1 = 1.85$  mm,  $W2 = 1.6$  mm,  $W3 = 1$  mm,  $W4 = 3.5$  mm,  $W5 = 22.6$  mm,  $W6 = 5.84$  mm,  $W7 = 5.35$  mm,  $L2 = 12$  mm,  $L3 = 4$  mm,  $L4 = 2.6$  mm,  $L5 = 21$  mm,  $L6 = 1.3$  mm,  $Wr = 8$  mm,  $Lr = 12.6$  mm,  $W_{T1} = 0.4$  mm,  $W_{T2} = 2$  mm,  $L_{T1} = 1.2$  mm,  $L_{T2} = 0.6$  mm,  $L_{T3} = 1.85$  mm,  $L_{T4} = 0.35$  mm, and  $L_{T5} = 8$  mm. The dimensions of the antenna are  $0.64\lambda \times 0.41\lambda$ , with an overall area of  $0.262\lambda^2$ . The focus of this design is to improve the XP performance of the antenna at higher frequencies, along with reduction of the antenna size. The antenna

miniaturization is achieved by modifying the feedline, and the bow-tie arms. An optimized microstrip balun is used as a feedline, with a linear tapered ground plane. The origin of the coordinates is at the top right corner of Fig. 4.1(b), so the linear tapered feedlines can be represented by

$$\begin{aligned} x_1 &= 1.875z - 32.2, & \text{for } 29 \leq z \leq 32.2 \\ x_2 &= 6z - 29, & \text{for } 28 \leq z \leq 29 \end{aligned} \tag{4.1}$$

where  $x_1, x_2$ , and  $z$  are the coordinates of the linear tapered ground curves in millimetres. This offers a more gradual impedance transition than stepped tapering; therefore, it improves impedance matching. Also, large rectangular slots, gaps, and T-shaped slots are optimized and added to each end of the bow-tie arms, to achieve antenna miniaturization. The large rectangular slots force the currents to flow a longer path, which results in an overall 2 dB return loss improvement for the lower frequency band. Then the gaps and T-shaped slots combined creates capacitive coupling that adds another resonance at 2.4 GHz. Furthermore, it is a known fact that currents on the antenna surface are the source of radiation, and radiation pattern depends on current distribution [72]. For bow-tie antenna, the surface currents are concentrated at the feed location and are along a diagonal path, whereas further away from the feed, currents are along a straight path. Surface currents along a diagonal path on the antenna have both vertical and horizontal components, which radiate fields in both vertical and horizontal directions; and the antenna exhibits poor XP performance. Here, we propose to use a pair of slots on each arm of the bow-tie to straighten the currents, to reduce the radiated fields in other directions, and to improve the XP performance. Fig. 4.3 shows the fabricated modified bow-tie antenna.

## 4.4 Results and Discussion

### 4.4.1 Frequency Domain Characteristics

In this section, the measurement results of the frequency domain characteristics are presented and discussed. The measured return loss and realized gain of the modified and conventional bow-tie antennas are shown in Fig. 4.4(a)-(b), respectively. It can be seen that S11 is lower than -10 dB over the frequency band of 2 to 5 GHz for these antennas. The measured gain of the antenna is similar to the simulated gain throughout the operating band. The difference between the simulated and measured gain can be attributed mainly to the losses in the antenna, further material tolerances and characterization of the feed in the simulation, as well as dimension precision of the fabricated antenna, and calibration accuracy of the measurement equipment. Since the antenna gain is directly related to the antenna size [11], the gain of the conventional bow-tie antenna is higher than the modified bow-tie antenna. The overall area ( $L \times W$ ) of the conventional and modified bow-tie antennas are  $2379.3 \text{ mm}^2$  and  $1819.4 \text{ mm}^2$ , respectively. Therefore, the overall miniaturization achieved is 23.5%. Nevertheless, the gain reduction due to a smaller antenna can be compensated by a low noise amplifier in the radar receiver chain. Furthermore, the gain increases with frequency, which can be attributed to the increase in effective area of the antenna with frequency. The simulated radiation efficiency, without losses of the antenna, across the frequency spectrum at 2, 3, 4 and 5 GHz are: 96%, 97%, 98% and 97%, respectively.

To acquire further insight on the antennas performance, current distribution on both conventional and modified bow-tie arms are studied. Fig. 4.5(a)-(b), illustrates the surface current vector distribution on the conventional and modified bow-tie arms at 5 GHz. The inclined current vectors in the conventional structure is aligned in parallel to the E- or H-planes with the modified structure. This confirms that the rectangular slots reduced the inclined vertical

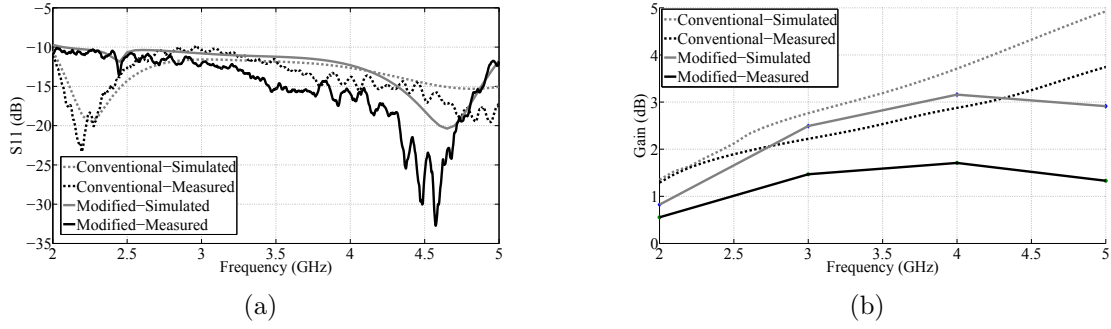


Figure 4.4: Simulated and measured: (a) return loss and (b) realized gain.

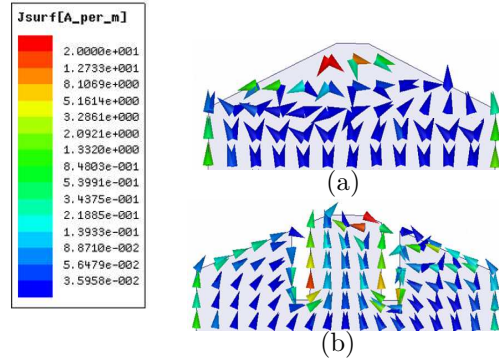


Figure 4.5: Current vector distribution at 5 GHz on: (a) conventional and (b) modified bow-tie antenna.

electrical current in the bow-tie arms, which results in the improvement of the antennas XP level. In addition, Fig. 4.6(a)-(d) illustrates the surface current density distribution on the modified bow-tie arms at 2, 3, 4 and 5 GHz, respectively. It is observed that the current distribution at these frequencies are mainly concentrated at the flare region of the arms, it shows the proposed modification straightens the current path on the antenna.

Fig. 4.7 plots both the measured E- and H-plane normalized radiation patterns of the conventional and modified bow-tie antennas. From the plots, it is shown that both antennas have omnidirectional radiation patterns in the H-plane throughout the operating band. Also, it is observed that the proposed modification is more effective in lowering the XP level in H-plane than in E-plane. This was the intended behaviour as the XP of the conventional antenna

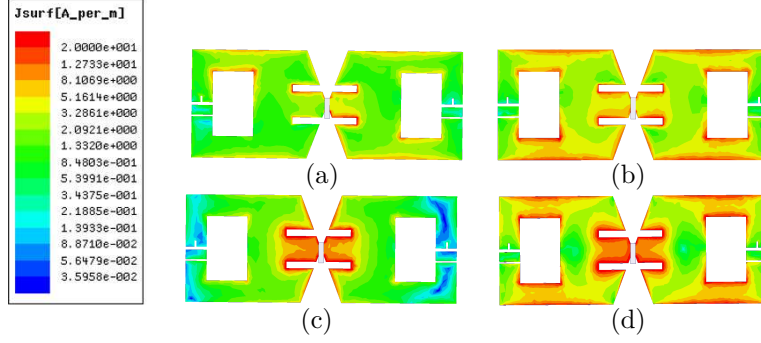


Figure 4.6: Current density distribution on the modified bow-tie antenna at: (a) 2 GHz, (b) 3 GHz, (c) 4 GHz, and (d) 5 GHz.

in the E-plane was already sufficiently low with an average of -30 dB over 2 to 5 GHz. In the H-plane at 2 GHz, the modified antenna has similar performance as the conventional one. For frequencies between 3 to 5 GHz, the modified antenna shows a good improvement in XP level compared to the conventional antenna, which indicates the modified antenna is more effective at higher frequencies. In addition, the effect of the slots can be observed from the simulated radiation patterns as shown in Fig. 4.8, while the XP levels at boresight direction are recorded in Table. 4.1. From the table, it is observed that the XP levels are well maintained at lower frequencies, and improved at higher frequencies in spite of miniaturization of the antenna. Furthermore, the modified bow-tie antenna with an improved XP level is suitable for radar imaging applications such as through-wall imaging, and breast cancer imaging. In [3], a 20 dB XP level in the E- and H-plane has shown to be effective in the detection, localization, and imaging of targets behind a brick wall. In [66], a 15 dB XP level in the E- and H-plane has demonstrated successful detection, localization, and imaging of breast tumours. Finally, the simulated and measurement results of the modified bow-tie antenna are in agreement, as depicted in Fig. 4.9.

Table 4.1: E- and H-planes XP level

E-plane XP level at:	Without slot (dB)	With slot (dB)
2 GHz	33.9	36.8
3 GHz	27.2	28.6
4 GHz	34.4	39.7
5 GHz	23.5	29.3
H-plane XP level at:	Without slot (dB)	With slot (dB)
2 GHz	14.9	15.2
3 GHz	20.3	21.9
4 GHz	19.1	27
5 GHz	17.1	24.4

#### 4.4.2 Time Domain Characteristics

In this section, the measurement results of the time domain characteristics are presented and discussed. In UWB radar imaging, the transmitted and received pulse parameters are important in the development of post processing algorithms for extracting the information of interest. Therefore, the time domain impulse response of the proposed antenna is investigated, and its measurement results are presented. The time domain impulse response is equivalent to the transfer function in frequency domain, where transfer function for UWB antennas have been investigated in [81–83]. The photograph and block diagram of the time domain measurement setup are shown in Fig. 4.10, which consists of a VNA, and two identical modified bow-tie antennas placed with boresight configuration. The UWB pulse  $x(t)$  generated by a VNA with  $50 \Omega$  source impedance, is fed into the transmitter antenna. Then the received pulse  $y(t)$  picked up by a  $50 \Omega$  terminated receiver antenna, is digitized by the VNA for post-processing; to determine the transfer functions.  $X(\omega)$  and  $Y(\omega)$  are the Fourier transforms of  $x(t)$  and  $y(t)$ , respectively. The excitation pulse and its frequency spectrum are shown in Fig. 4.11(a)-(b), respectively. The distance between the antennas (R) is 30 cm. While the distance between the antennas and ground is 1 m, to ensure that reflections from the ground can be time-gated. The antenna transfer function in transmission and reception

can be represented by [81]

$$H_T(\omega) = \frac{E^i(\omega, R)}{X(\omega)} \cdot R \cdot e^{jkR} \quad (4.2)$$

$$H_R(\omega) = \frac{Y(\omega)}{E^i(\omega, R)} \quad (4.3)$$

where  $k$  is the wave number in free space and  $E^i(\omega, R)$  is the incident electric field on the aperture of the Rx antenna. Then the transfer function of the antenna measurement system can be found by relating the Tx and Rx signals from Eq.(4.2-4.3) given by [81]

$$H(\omega, R) = \frac{Y(\omega)}{X(\omega)} = H_T(\omega) \cdot H_R(\omega) \cdot \frac{e^{-jkR}}{R} \quad (4.4)$$

The relationship between  $H_T(\omega)$  and  $H_R(\omega)$  can be represented by [81]

$$H_T(\omega) = \frac{j\omega}{2\pi c} \cdot H_R(\omega) \quad (4.5)$$

Then from Eq.(4.4-4.5),  $H_T(\omega)$  and  $H_R(\omega)$  can be re-represented by [81]

$$H_T(\omega) = \sqrt{\frac{j\omega}{2\pi c} \cdot H(\omega, R) \cdot R \cdot e^{jkR}} \quad (4.6)$$

$$H_R(\omega) = \sqrt{\frac{2\pi c}{j\omega} \cdot H(\omega, R) \cdot R \cdot e^{jkR}} \quad (4.7)$$

Once measurements of the excitation and received pulses are acquired, the transfer function of the antenna measurement system, as well as the transfer function of the antennas in Tx and Rx modes can be estimated. An inverse Fourier transform of the transfer functions gives the impulse response of the antenna for transmitting  $h_t(t)$  and receiving modes  $h_r(t)$ ,

represented by [81]

$$h_t(t) = \frac{1}{2\pi} \int_{-\infty}^{\infty} H_T(\omega) \cdot e^{j\omega t} d\omega \quad (4.8)$$

$$h_r(t) = \frac{1}{2\pi} \int_{-\infty}^{\infty} H_R(\omega) \cdot e^{j\omega t} d\omega \quad (4.9)$$

Fig. 4.11(c) plots the measured received pulse  $y(t)$  at boresight. Fig. 4.12(a)-(b) plots the transfer function of the antenna measurement system  $H(\omega)$  at boresight, and impulse response of the antenna transmitting mode  $h_t(t)$  along an arc of  $-60^\circ$  to  $60^\circ$  with  $20^\circ$  separation, respectively. It is observed that the pulse intensity of the transmitting mode  $h_t(t)$  is halved at  $\pm 56.2^\circ$ , which corresponds to an E-plane half power beamwidth of  $112.4^\circ$ . Fig. 4.12(c)-(d) plots the impulse response of the antenna for transmitting  $h_t(t)$  and receiving  $h_r(t)$  modes at boresight, respectively. In order to compare the antenna impulse responses, the fidelity factor is computed [82]. The fidelity factor ( $F$ ) between two signals  $a(t)$  and  $b(t)$  is represented by

$$F[a(t), b(t)] = \max \int_{-\infty}^{\infty} a_n(t) \cdot b_n(t + \tau) dt \quad (4.10)$$

where  $a_n(t)$  and  $b_n(t)$  are the normalized  $a(t)$  and  $b(t)$  are represented by

$$a_n(t) = \frac{a(t)}{\sqrt{\int_{-\infty}^{\infty} |a(t)|^2 dt}} \quad (4.11)$$

$$b_n(t) = \frac{b(t)}{\sqrt{\int_{-\infty}^{\infty} |b(t)|^2 dt}} \quad (4.12)$$

The fidelity factor is computed for the time derivative of the impulse response for receiving mode with the impulse response for transmitting mode at boresight, e.g.,  $F[h'_r(t), h_t(t)]$ . The result of the cross-correlation is as high as 0.78, which shows good fidelity between  $h'_r(t)$  and  $h_t(t)$ . Furthermore, this confirms the result shown in [83], where for most antennas,

especially aperture antennas, the transmitting impulse response  $h_t(t)$  is the time derivative of the receiving impulse response  $h_r(t)$ .

For some UWB radars, the excitation pulse is a chirp pulse. Therefore, a time domain impulse response simulation using a full wave simulator, CST Microwave studio is presented. A chirp pulse with 2 to 5 GHz spectral coverage is fed to the antenna, and ideal voltage probes placed in the far field region are used to collect the chirp pulse. The antenna input and output pulses are shown in Fig. 4.13(a), while the match filtered result of the input and output chirp pulses are shown in Fig. 4.13(b). The radiated pulse is very much correlated (70%) with the input pulse.

## 4.5 Conclusion

In this chapter, a modified bow-tie antenna using slots on the radiating arms is presented. Compared with the conventional bow-tie antenna, the modified antenna achieves XP improvement and miniaturization. By optimizing the geometry and location of the rectangular slots on the radiating arms, the current vectors can be aligned vertically or horizontally to effectively reduce the XP level. Simultaneously, a miniaturized antenna design is obtained from optimization of the feedline, and of the bow-tie arms. Simulation and measurement results in both the frequency and time domains are presented with good agreement. Based on these characteristics, the antenna is a good candidate for UWB radar imaging systems.

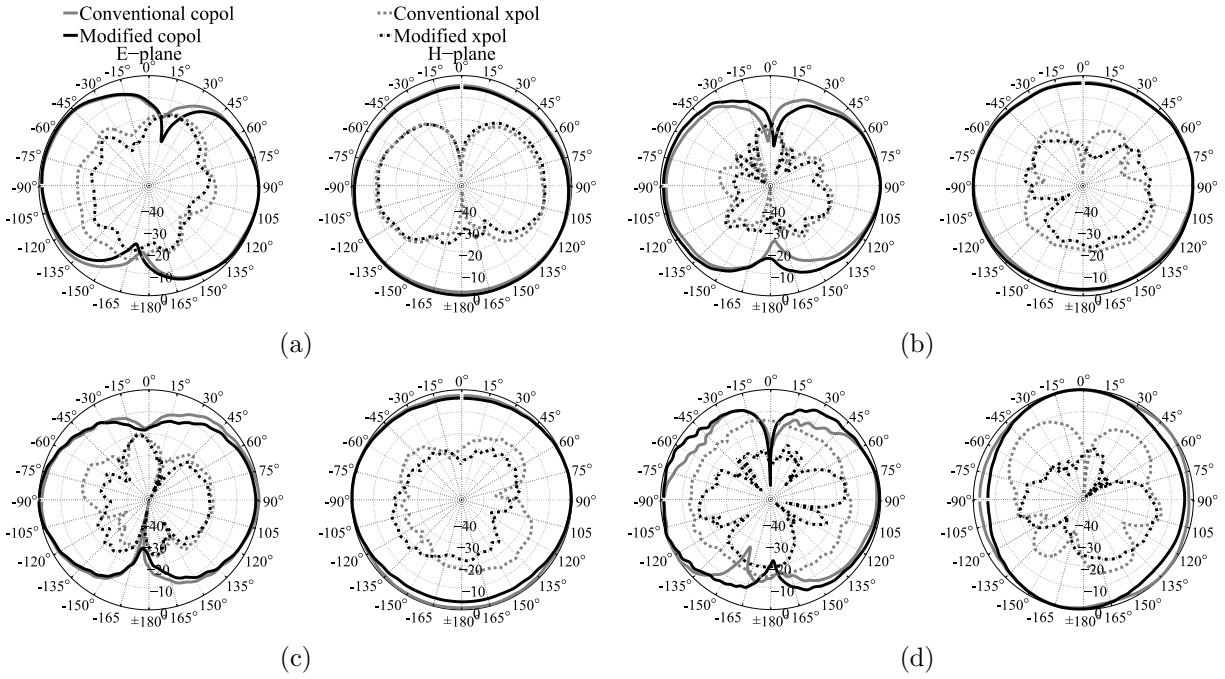


Figure 4.7: E- and H-plane normalized measured radiation patterns of the conventional and modified bow-tie antennas at: (a) 2 GHz, (b) 3 GHz, (c) 4 GHz, and (d) 5 GHz.

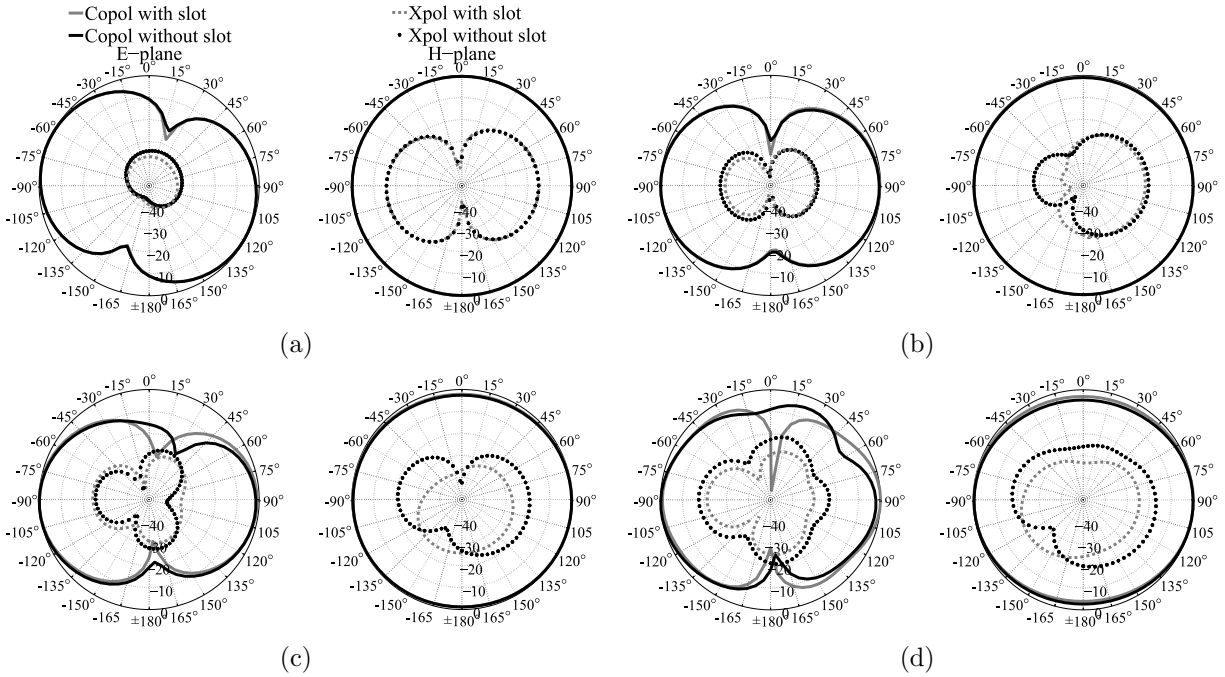


Figure 4.8: E- and H-plane normalized simulated radiation patterns of the modified bow-tie antenna with and without slots at: (a) 2 GHz, (b) 3 GHz, (c) 4 GHz, and (d) 5 GHz.

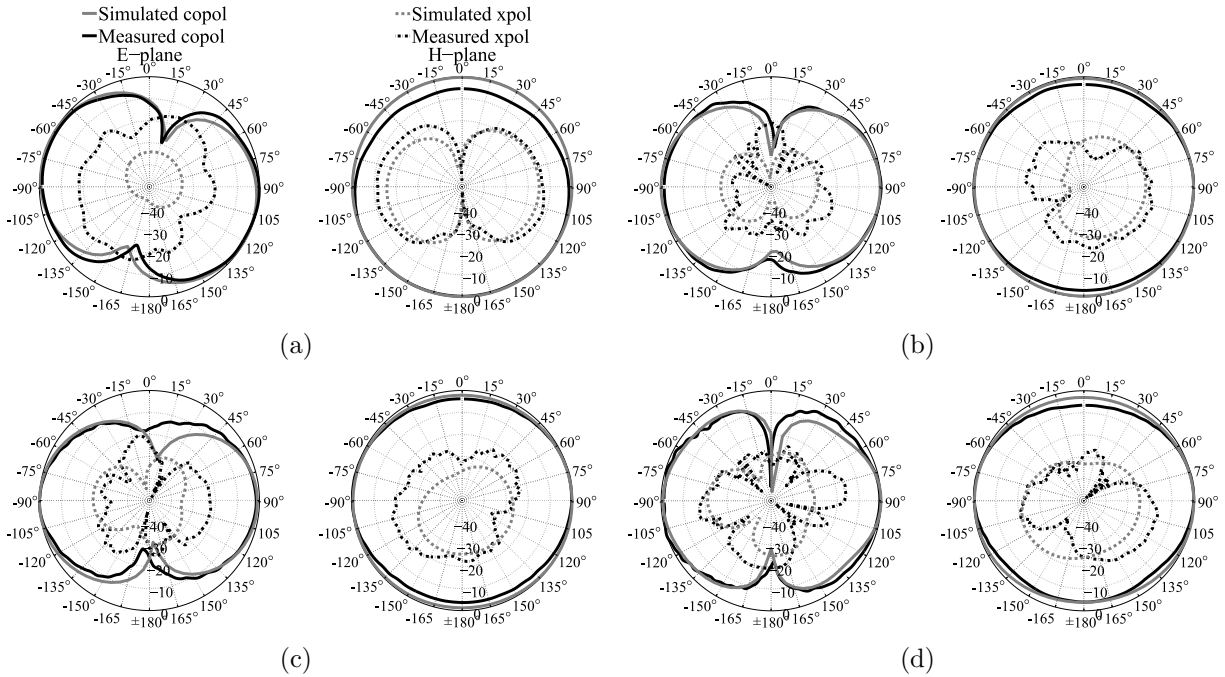


Figure 4.9: E- and H-plane normalized simulated and measured radiation patterns of the modified antenna at: (a) 2 GHz, (b) 3 GHz, (c) 4 GHz, and (d) 5 GHz.

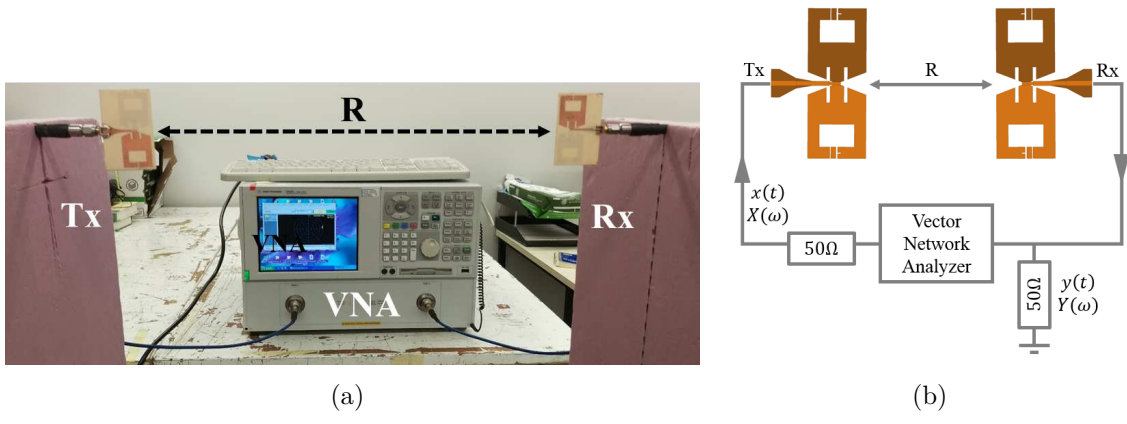


Figure 4.10: (a) Photograph, and (b) block diagram of the time domain measurement setup.

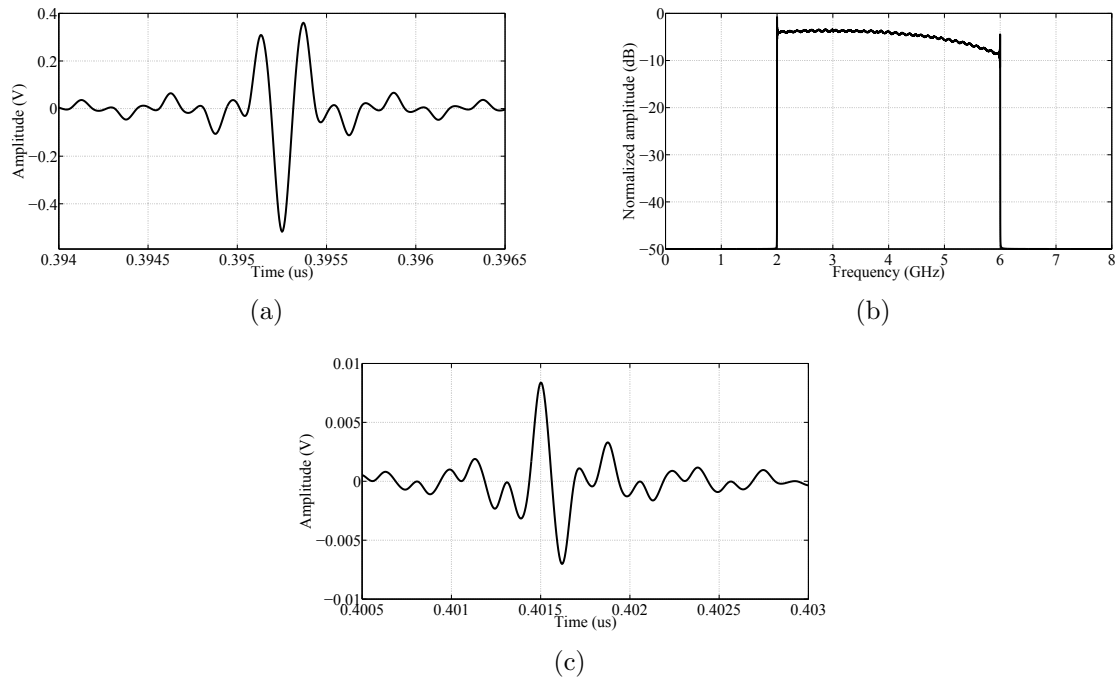


Figure 4.11: Measured: (a) time domain excitation pulse  $x(t)$ , (b) frequency domain excitation pulse  $X(\omega)$ , and (c) time domain received pulse  $y(t)$  at boresight.

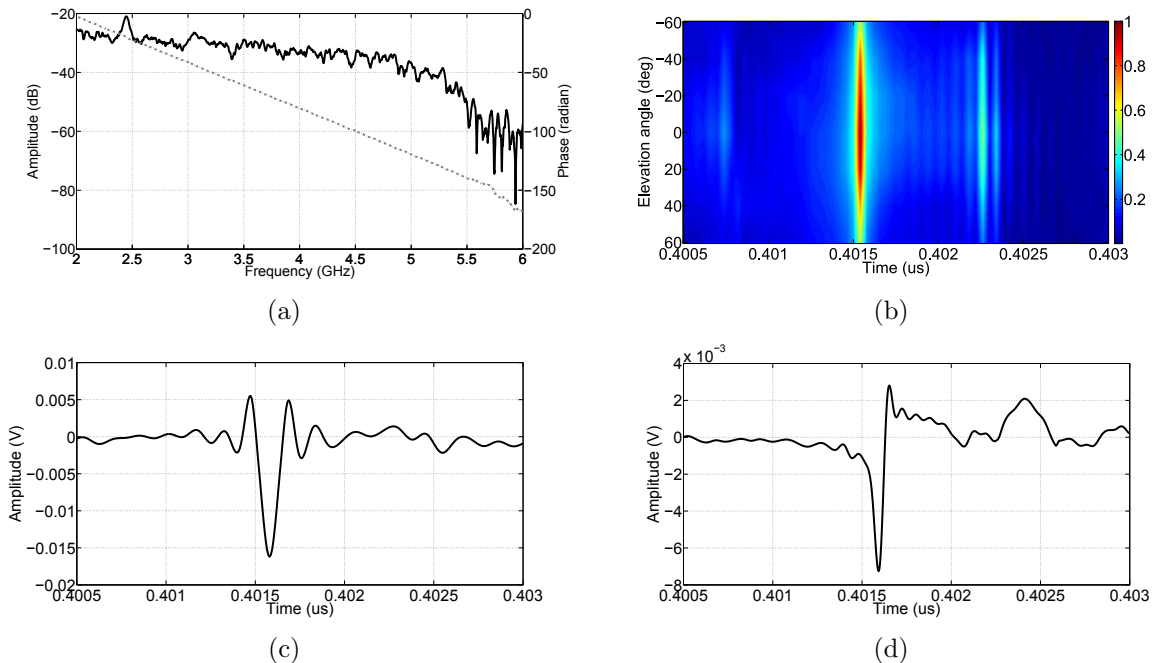
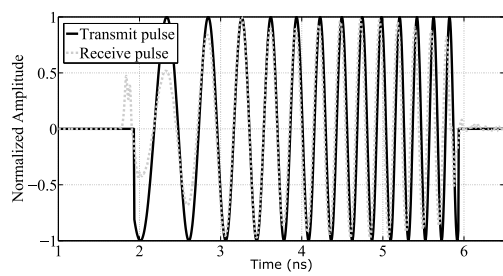
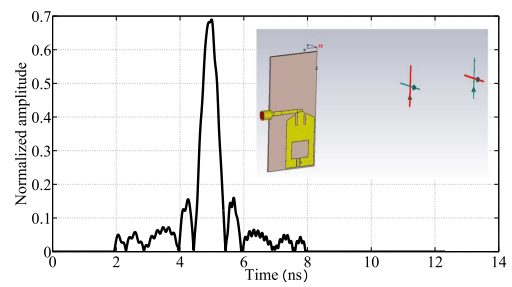


Figure 4.12: Measured: (a) transfer function of the antenna measurement system  $H(\omega)$  at boresight, (b) impulse response of the antenna transmitting mode  $h_t(t)$  at different elevation angles, (c) impulse response of the antenna transmitting mode  $h_t(t)$  at boresight, and (d) impulse response of the antenna receiving mode  $h_r(t)$  at boresight.



(a)



(b)

Figure 4.13: CST simulation: (a) antenna input and output pulses, and (b) match filtered pulse.

# Chapter 5

## Software Simulation

### 5.1 Overview of Software Simulation

Software simulations using CST Microwave Studio and MATLAB are presented. Then a signal processing procedure is proposed, as shown in Fig. 5.1. The signal processing procedure can be categorized into two parts: pre-processing and post-processing. The pre-processing stage consists of four steps, in which the data is first multiplied by a Hamming window to reduce the spectral leakage, followed by calibration to remove background noise and propagation delay. Then the proposed spectral envelope and impulsization method is applied to remove the effect of ramp modulation. The post-processing consists of either LSAR or CSAR processing, with a modified frequency domain GBP algorithm for image reconstruction. The calibration techniques will be presented as part of Chapter 6, since its formulation requires measurement data (see section 6.1).

This chapter presents the software simulations for the spectral estimation, the effect of ramp modulation on the beat spectrum and its mitigation methods, the LSAR and CSAR image reconstruction, as well as the effect of phase noise on SAR image resolution.

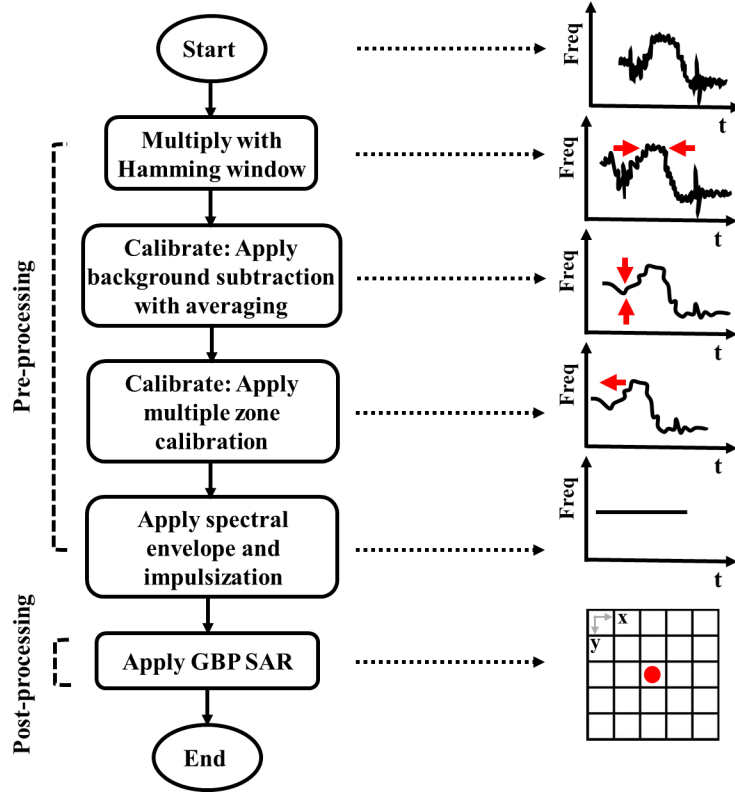


Figure 5.1: Signal processing procedure.

## 5.2 Pre-processing

### 5.2.1 Spectral Estimation

The collected beat signals can be in the form of A-scan, B-scan or C-scan. The collection of A-scans along a line on the surface forms a B-scan, while the C-scan is represented by a collection of B-scans to form a 3-D radargram of the target scene. This study focuses on the fast Fourier transform (FFT) spectral estimation for A-scan beat signals, which is a two-step process: First, the A-scan signal is generated in MATLAB, with independent and identically distributed (IID) Gaussian noise included and can be represented by (see section 1.2.3)

$$s_b^{ideal}(t) = \cos(2\pi c_r \tau_{d1} t) + s_{noise}(t) \quad (5.1)$$

where  $c_r = 200$  GHz/s and  $\tau_{d1} = 10$  ns. Second, FFT is applied to represent the signal in the

frequency spectrum. FFT is a fast and efficient algorithm for computation of the discrete Fourier transform [84]. Furthermore, FFT operates on the assumption that the time domain signal is continuous with  $N$  integer number of periods, in which the two ends have the same amplitude values. However, in real world signal acquisition the length of the measured signal is often not an integer multiple of the period. This results in spectral leakage that smears the spectrum, degrades the resolution and the detection of weak signals. To illustrate, the FFT for a beat signal with  $N = 1000$  ( $\Delta f = 2$  Hz) and  $N = 1011$  ( $\Delta f = 1.9978$  Hz) are shown in Fig. 5.2(b). It is observed for  $N = 1011$ , the energy in the 2 kHz spectrum is leaked to nearby frequencies and the spectrum has a wider mainlobe width. Nevertheless, the spectral leakage can be reduced with the use of the windowing technique [84].

The windowing technique is a two step process: First, multiply the time domain beat signal by a finite length window function. The window function has an amplitude that varies smoothly and gradually towards zero at the edges, which reshape the signal and make the two ends meet without sharp transitions. The window functions such as, Hamming and Blackman-Harris are applied to the FFT signals shown in Fig. 5.2(b). In general, for each window function, there exists an inherent compromise between the choice of improving the frequency resolution (main lobe width), or the detection of weak signals in the presence of nearby strong signals (side lobe level) [84]. As it can be seen, the Hamming window has decent frequency resolution and SNR. Second, since MATLAB employs a radix-2 FFT, the length of the signal should be  $2^N$  (where  $N$  is an integer value) before applying the FFT, to achieve a faster computational time.

### 5.2.2 Effect of Deramp Processing on Beat Spectrum

This study focuses on understanding the effect of deramp processing, with phase noise included in the transmitted signal, on the beat spectrum. A simulation model for the deramp processing using full wave simulator CST Microwave Studio and MATLAB is presented. The

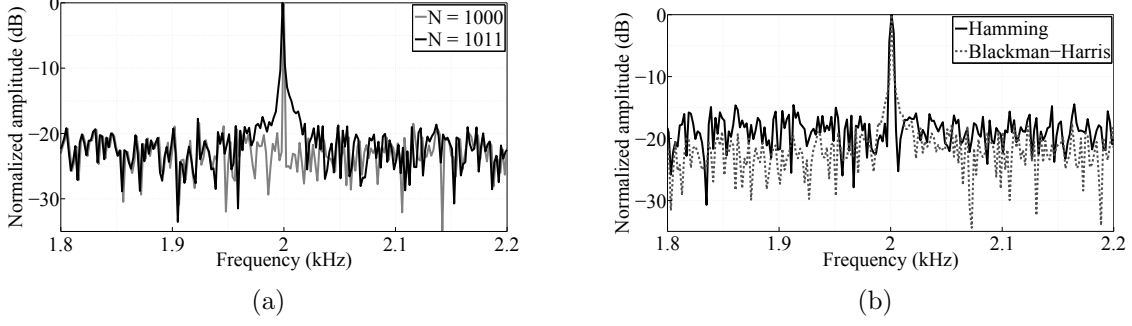


Figure 5.2: MATLAB simulation: (a) FFT with integer and non-integer multiples of the period. (b) Window functions applied to the FFT signals with non-integer multiples of the period.

system parameters for the simulation are  $T_{ramp} = 4$  ns,  $f_s = 2$  GHz,  $B = 2$  GHz,  $c_r = 5 \times 10^{17}$  Hz/s,  $\psi_{noise} = -65$  dBc/Hz at 1 kHz,  $-89$  dBc/Hz at 10 kHz and  $-110$  dBc/Hz at 100 kHz and  $\varsigma = 0.1$  %. Where  $\varsigma$  is the frequency sweep nonlinearity, which can be represented by [40]

$$\varsigma = \frac{\max|f_t^{lin}(t) - f_t^{nlin}(t)|}{B} \quad (5.2)$$

where  $f_t^{lin}(t)$  and  $f_t^{nlin}(t)$  are the instantaneous linear and nonlinear transmitting frequencies respectively. Where  $\psi_{noise}$  is the phase noise modelled as time jitter. The relation between phase noise and time jitter can be represented by [53]

$$J_{RMS}(t) = \frac{\sqrt{2 \int_{f_1}^{f_2} L_\psi(f) df}}{2\pi f_c} \quad (5.3)$$

where  $f_c$  is the center frequency,  $f_1$  is the initial offset frequency,  $f_2$  is the cut-off offset frequency and  $L_\psi(f)$  is the single sideband phase noise spectrum, which can be represented by

$$L_\psi(f) = 10^{\frac{\chi}{10}} \quad (5.4)$$

where  $\chi$  is the phase noise power in dB relative to the carrier frequency. For the given VCO phase noise parameters, the time jitter is 1.5 ps. In this study, jitter is included to the time

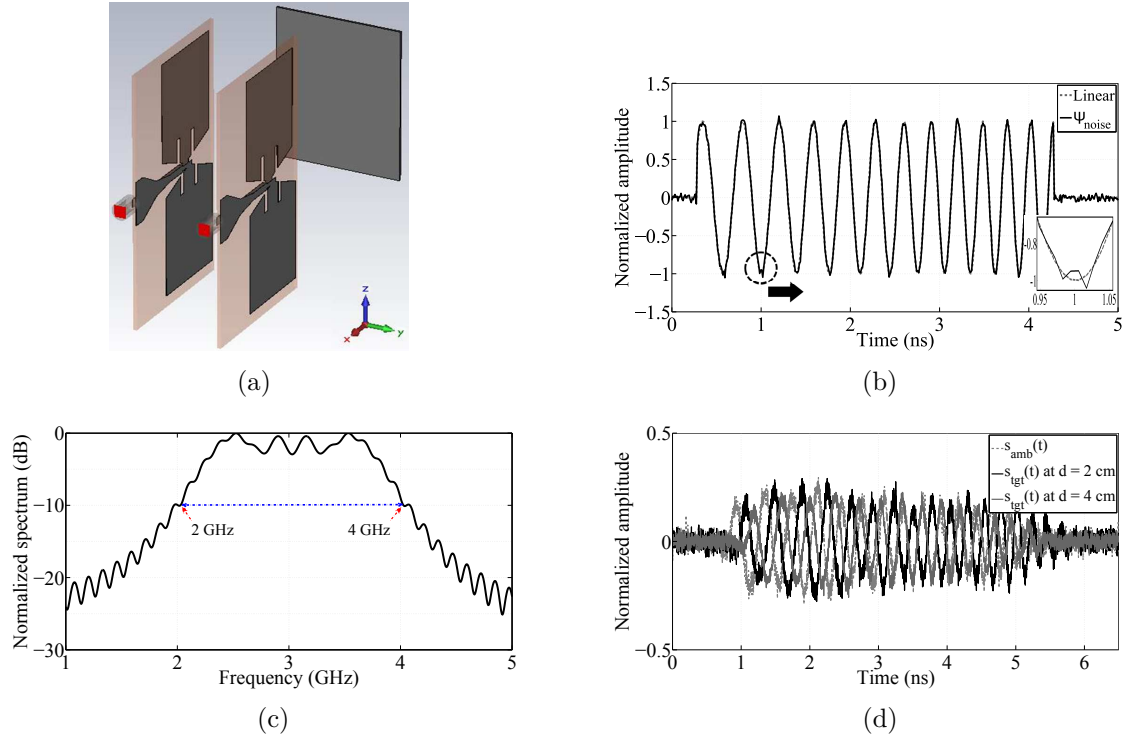


Figure 5.3: CST Simulation: (a) antenna configuration, (b) time domain input pulse, (c) spectrum of the input pulse, and (d) time domain received pulse. Note:  $\psi_{noise} = -65$  dBc/Hz @ 1 kHz,  $-89$  dBc/Hz @ 10 kHz,  $-110$  dBc/Hz @ 100 kHz.

of the transmitter signal as a random noise of peak 1.5 ps, and is evaluated by computing the standard deviation of the average oscillator period [85].

In the full wave simulation, a set of bow-tie antennas with frequency bandwidth from 2 to 5 GHz is used. The antennas are placed in quasi-monostatic configuration, as shown in Fig. 5.3(a). A generated chirp pulse is fed to the Tx antenna. Its time domain pulse and frequency spectrum, for the above system parameters, are shown in Fig. 5.3(b) and 5.3(c) respectively. At first glance, the linear and phase noise added time domain input pulses appear the same. However, a zoom into the plot shows the variation due to phase noise. The reflected pulses from a metal plate placed in front of the antenna aperture at 2 cm and 4 cm are measured. Since the antennas are placed in close proximity, 1 cm, antenna mutual coupling has to be accounted for in the Rx pulse. This effect is significant for near distance

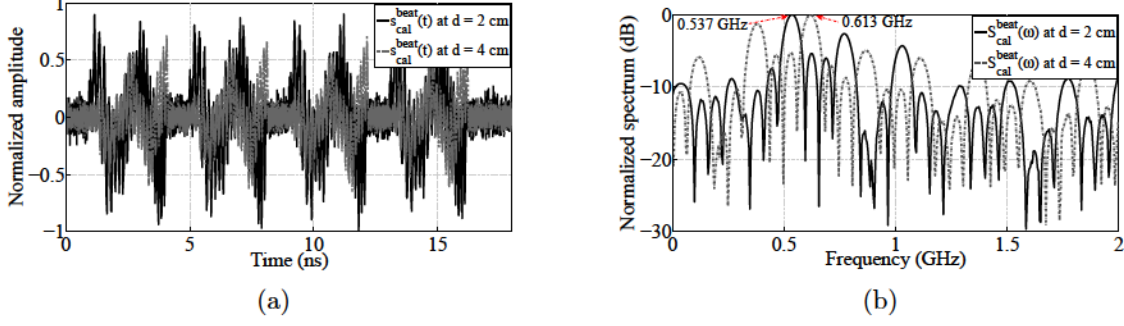


Figure 5.4: MATLAB Simulation: (a) time domain calibrated beat signal, and (b) spectrum of the calibrated beat signal.

imaging systems. The effect of antenna mutual coupling can be eliminated by calibration. Therefore, simulations with and without target are performed, in which the measured Rx pulses are denoted as  $s_{tgt}(t)$  and  $s_{amb}(t)$  respectively, and are shown in Fig. 5.3(d). The amplitude of the Rx pulse is normalized to the amplitude of the Tx pulse.

In this simulation, four periods of the signal are considered. The delayed target signal  $s_{tgt}(t)$  is fed into the RF port of the mixer, while the input signal  $s_{in}(t)$  is fed into the LO port of the mixer, which can be represented by

$$s_{tgt}^{beat}(t) = s_{in}(t) \cdot s_{tgt}(t) \quad (5.5)$$

Similarly, for the ambient case, which can be represented by

$$s_{amb}^{beat}(t) = s_{in}(t) \cdot s_{amb}(t) \quad (5.6)$$

Then the calibrated beat signal, cf. Fig. 5.4(a), can be represented by

$$s_{cal}^{beat}(t) = s_{tgt}^{beat}(t) - s_{amb}^{beat}(t) \quad (5.7)$$

For the given system parameters and (2.3), the expected ideal beat frequencies for the targets at 2 cm and 4 cm are 0.067 GHz and 0.133 GHz, respectively. However, it is observed

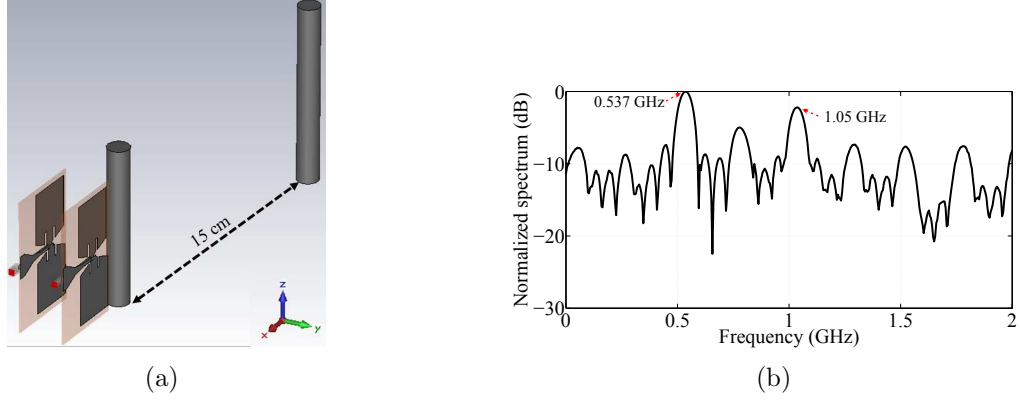


Figure 5.5: Two targets simulation: (a) antenna configuration, and (b) spectrum of the calibrated beat signal.

that  $S_{cal}^{beat}(\omega)$ , cf. Fig. 5.4(b), shows the beat frequencies at 0.537 GHz and 0.613 GHz. The measured beat frequency is about 0.475 GHz higher than the ideal beat frequency. This increase in beat frequency is mainly due to the group delay of the transceiver antennas, which is 0.95 ns.

In addition, a two target case is also considered as shown in Fig. 5.5(a). The reflected pulses from two metal targets placed in front of the antenna aperture at 2 cm and 17 cm are measured at the Rx antenna. Antenna mutual coupling and mixer operation are also considered as discussed above. For the given system parameters, the expected ideal beat frequencies are 0.067 GHz and 0.567 GHz respectively. However, it is observed that  $S_{cal}^{beat}(\omega)$ , cf. Fig. 5.5(b), shows the beat frequencies at 0.537 GHz and 1.05 GHz respectively. For a target separation of 15 cm the measured beat frequency difference is 0.513 GHz, which is higher than the ideal beat frequency difference of 0.5 GHz. This could also be due to the group delay of the transceiver antennas.

It is observed that  $S_{cal}^{beat}(\omega)$ , cf. Fig. 5.4(b) and 5.5(b), has many sidelobes with peaks separated by a constant frequency, which is inversely proportional to the period of the ramp. Therefore, the frequency resolution is approximately  $1/T_{ramp}$ . In other words, the ramp sig-

nal is convolved with the Rx pulse and appears modulated with frequency peaks separated by  $1/T_{ramp}$ . This modulation effect is undesired as it limits the minimum achievable resolution, degrades the Rx SNR and creates false alarms. To mitigate these sidelobes, two methods are proposed: the deconvolution method, and the spectral envelope and impulsization method.

### 5.2.3 Deconvolution Method

The analytical approach of the proposed deconvolution method is presented in Fig. 5.6. The beat signal can be expressed as a convolution of the ramp signal with the Rx pulse represented by

$$s_{cal}^{beat}(t) = s_{caltgt}^{beat}(t) \otimes r(t) \quad (5.8)$$

where  $r(t)$  is the ramp signal. The deconvolution can be performed in frequency domain as a simple division represented by

$$S_{caltgt}^{beat}(\omega) = \frac{S_{cal}^{beat}(\omega)}{S_{ra}(\omega)} \quad (5.9)$$

where  $S_{ra}(\omega)$  is the convolution of the ramp signal with the transmitted pulse. The above two cases are considered to examine the deconvolution effect on the beat spectrum. The frequency domain representation of the beat signal  $S_{caltgt}^{beat}(\omega)$  after deconvolution is shown in Fig. 5.7. As it can be seen after deconvolution, the two targets are detected and sidelobe levels are suppressed; however, the mainlobe width has increased. This could be due to the noise of the transmitted signal, and the estimate of the transfer function.

### 5.2.4 Spectral Envelope and Impulsization Method

The analytical approach of the proposed spectral envelope and impulsization method is presented in Fig. 5.8. The linear prediction coefficient (LPC) technique is applied to detect the envelope of the calibrated beat pulse [86]. The pulse envelope, cf. Fig. 5.9(a), can be

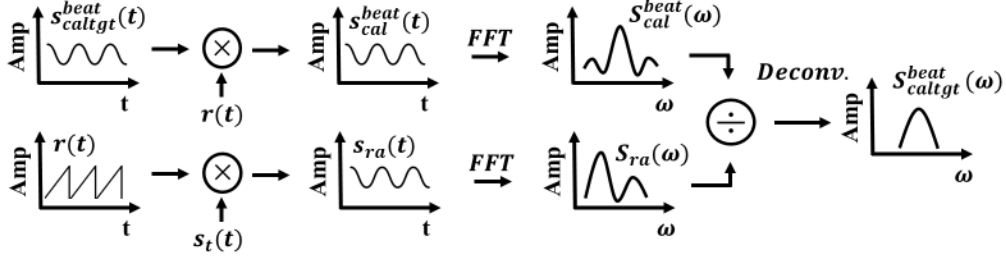


Figure 5.6: Block diagram of the deconvolution method.

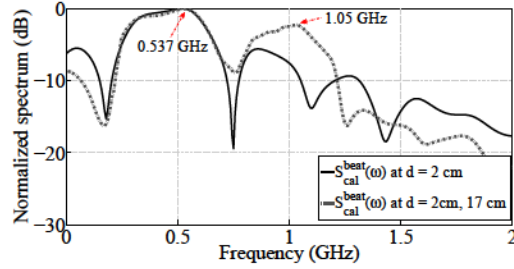


Figure 5.7: Calibrated beat spectrum after deconvolution method.

represented by

$$S_{ev}(\omega) = \left| \mathcal{F} \left\{ \sum_{i=1}^p a_i s_{tgt}^{beat}(n - i) \right\} \right| \quad (5.10)$$

where  $n$  is the discrete time index,  $p$  is the order of prediction and  $a_i$  is the LPC. Next, an amplitude threshold level is set to identify the number of peaks, which corresponds to the number of targets. This threshold level will depend on system parameters and target scene setup. Then impulsization is applied to improve the SNR. The impulsization can be represented by

$$\delta \left( S_{caltgt}^{beat}(\omega) \right) = \begin{cases} P_{amp}, & \text{if } \omega = \omega_{peak} \\ \min(P_{amp}), & \text{otherwise} \end{cases} \quad (5.11)$$

where  $P_{amp}$  is the amplitude of the beat signal. The above two cases are also considered to examine this method. The frequency domain representation of the beat signal  $S_{caltgt}^{beat}(\omega)$

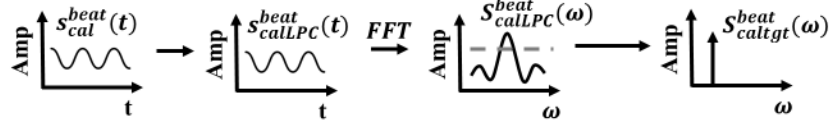


Figure 5.8: Block diagram of the spectral envelope and impulsization method.

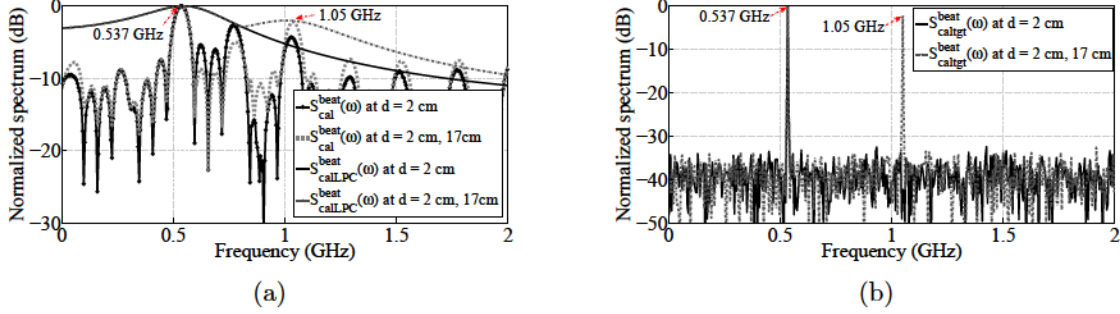


Figure 5.9: (a) Envelope of the calibrated beat spectrum. (b) Calibrated beat spectrum after spectral envelope and impulsization method.

after spectral envelope and impulsization method is shown in Fig. 5.9(b). As it can be seen, a better signal detection is realized where the overall SNR is improved, the sidelobes are effectively removed, and the frequency resolution is also improved. Overall, this method outperforms the deconvolution method.

## 5.3 Post-processing

### 5.3.1 LSAR Image Reconstruction

The LSAR image is reconstructed by applying a modified frequency domain GBP technique [3]. In LSAR, the radar system is moved in a Cartesian coordinate system to illuminate the target scene for raw data collection, as shown in Fig. 5.10. The reconstructed image  $I$  can be represented by [3]

$$I(m, n, k) = \sum_{l=1}^L s(l, idx(m, n, k)) \quad (5.12)$$

where  $(m, n, k)$  is the image pixel,  $l$  is the aperture position, and  $idx(m, n, k)$  is the signal index position represented by

$$idx(m, n, k) = \frac{f_b(m, n, k)}{\Delta f} \quad (5.13)$$

where  $\Delta f$  is the sampling frequency, and  $f_b(m, n, k)$  is the beat frequency represented by

$$f_b(m, n, k) = c_r \tau_d(m, n, k) \quad (5.14)$$

where  $\tau_d(m, n, k)$  is the target delay time represented by

$$\tau_d(m, n, k) = \frac{2R(m, n, k)}{c} \quad (5.15)$$

where  $R(m, n, k)$  is the distance between antenna to image pixel represented by

$$R(m, n, k) = \sqrt{(x_{ap} - x_m)^2 + (y_{ap} - y_n)^2 + (z_{ap} - z_k)^2} \quad (5.16)$$

where  $x_{ap}$ ,  $y_{ap}$ , and  $z_{ap}$  are the antenna aperture positions, and  $x_m$ ,  $y_n$ , and  $z_k$  are the image pixel locations. The SAR image reconstruction simulation with GBP technique is a five step process: First, define and grid an empty 2-D SAR image ( $M \times N$ ). Second, place a point like scatterer target in the SAR scene. Third, calculate  $R_p$  for each aperture position and pixel location. Then based on  $R_p$ , the time delay can be determined by  $\tau_d = 2R_p/c$  and the beat frequency can be determined by  $f_b = c_r \tau_d$ . Fourth, calculate the vector index corresponding to each beat frequency. The index is determined by  $idx = f_b/\Delta f$ . Fifth, extract the amplitude value associated with the calculated index and assign it to the corresponding pixel location. Repeat steps three to five for all aperture positions.

A pseudo-code for the simulation of LSAR with GBP is as follows:

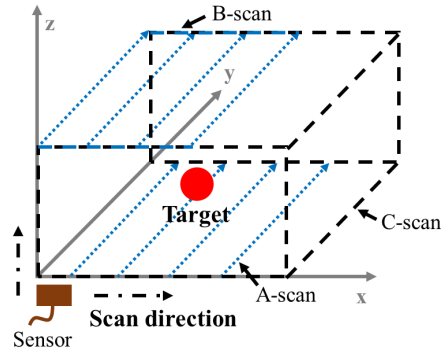


Figure 5.10: LSAR cartesian coordinates system.

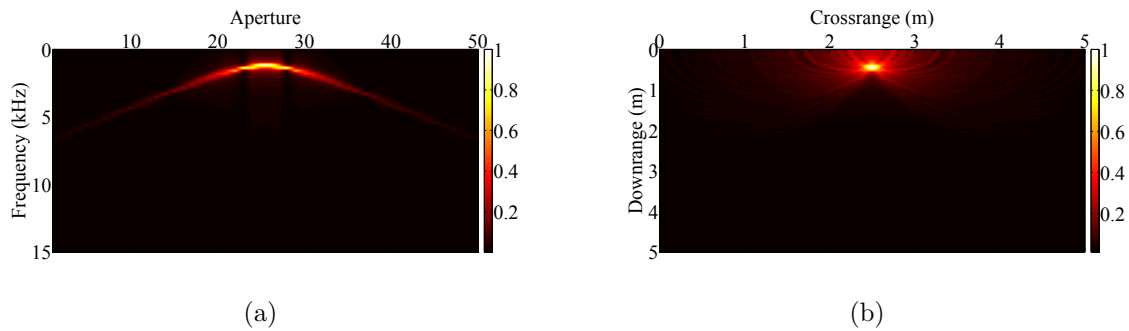


Figure 5.11: MATLAB simulation: (a) raw data, and (b) SAR image.

**Do loop**  $i = 1$  to Number of aperture positions

**Do loop** from  $j = 1$  to Number of grids in X-direction

**Do loop** from  $k = 1$  to Number of grids in Y-direction

**R(i,j,k)** = calculate the distance between aperture position and pixel location

**Beatf(i,j,k)** = calculate corresponding beat frequency for each  $R(i,j,k)$

**Idx(i,j,k)** = calculate corresponding index position for each beat  $Beatf(i,j,k)$

**Amp(i,j,k)** = extract the amplitude value associated with each  $Idx(i,j,k)$

**End loop**

**End loop**

Sum the values at each pixel location from each aperture position

**End loop**

The dimensions of the SAR target scene is 5 m of aperture length and 5 m of depth. The

point like scatterer target is placed in the target scene with coordinates of  $(x_1, y_1) = (2.5 \text{ m}, 0.5 \text{ m})$ . The total number of antenna aperture positions is 50, where each position is equally spaced at 10 cm apart. Then the Rx signals are collected by moving the antenna to each aperture position. A total of 50 A-scan 1-D signals in the form of signal strength versus beat frequency are collected, to form 1 B-scan 2-D matrix in the form of aperture position versus beat frequency. Since the antenna moves over the aperture, the distance between the antenna and the target will change such that the intensity of the Rx amplitude will display a hyperbola response, as shown in Fig. 5.11(a). Finally, GBP is applied to focus the energy of the hyperbola into a single point (at the center of hyperbola), as shown in Fig 5.11(b).

### 5.3.2 CSAR Image Reconstruction

The CSAR image reconstruction technique [11] is also adapted here for beat frequencies. In CSAR, the radar system is moved in a cylindrical coordinate system to illuminate the target scene for raw data collection, as shown in Fig. 5.12. Similar to LSAR, the image  $I$  can also be represented by (5.12), the  $idx(m, n, k)$  can also be represented by (5.13) and the  $R(m, n, k)$  can also be represented by (5.16). However, the antenna aperture position terms are represented differently in terms of cylindrical coordinates, which can be represented by [11]

$$\begin{aligned} x_{ap} &= r \cos \theta \\ y_{ap} &= r \sin \theta \end{aligned} \tag{5.17}$$

where  $r$  is the radius of the circular path and  $\theta$  is the antenna aperture position angle. The dimensions of the SAR target scene is 5 m of aperture length and 5 m of depth. The point like scatterer target is placed in the target scene with coordinates of  $(x_1, y_1) = (2.5 \text{ m}, 2 \text{ m})$ . The total number of aperture positions is 36, where each position is equally spaced at 10 degrees apart. A total of 36 A-scan 1-D signals are received at the Rx antenna, to form 1 B-scan 2-D matrix. The CSAR target scene of the raw data appears as a sinusoidal curve

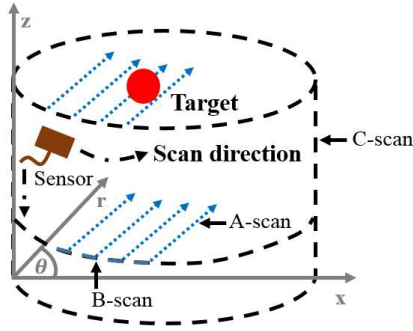


Figure 5.12: CSAR cylindrical coordinate system.

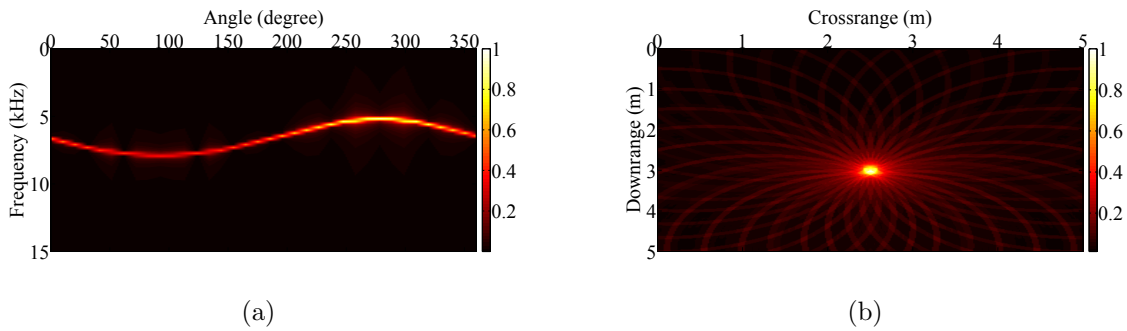


Figure 5.13: MATLAB Simulation: (a) raw data. (b) SAR image.

shown in Fig. 5.13(a). Finally, GBP is applied to focus the energy of the hyperbola into a single point, as shown in Fig. 5.13(b).

## 5.4 FMCW Radar Resolution

An important performance metric for an imaging radar is its resolution. Radar resolution in range and cross-range directions have been defined differently [32]. Furthermore, radar resolution has been shown to depend upon pulse characteristics, preprocessing of the raw data, and aperture length of the measurements [87]. In the next subsections, the relation between radar resolution, frequency bandwidth, phase noise, and aperture length are studied.

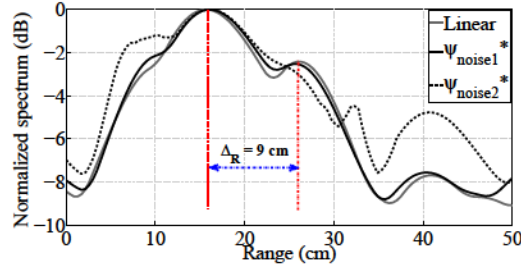


Figure 5.14: Beat signal range profile for a linear and phase noise added VCO, for a target separation of 9 cm and with a Tx pulse of  $B = 2$  GHz. Note:  $\psi_{noise1}^* = -65$  dBc/Hz @ 1 kHz,  $-89$  dBc/Hz @ 10 kHz,  $-110$  dBc/Hz @ 100 kHz.  $\psi_{noise2}^* = -55$  dBc/Hz @ 1 kHz,  $-75$  dBc/Hz @ 10 kHz,  $-95$  dBc/Hz @ 100 kHz.

### 5.4.1 Range Resolution

The criterion for range resolution is that the peaks of the overlapped beat frequencies should be separated by at least half of their peak values [39]. For a homodyne FMCW radar, the range resolution can be represented by [45]

$$\Delta_R = \frac{T_{ramp}c}{2B} \Delta f_b \quad (5.18)$$

where  $c$  is the speed of the pulse in the medium and  $\Delta f_b$  is the beat frequency resolution. In addition to frequency bandwidth, the effect of VCO phase noise on range resolution is also considered here. Phase noise is inherent to a VCO, and has shown to increase overall NFL, decrease Rx sensitivity and degrade resolution [48, 49]. Therefore, VCO phase noise has a prominent effect on the beat frequency resolution. The system parameters for the simulation are  $T_{ramp} = 4$  ns,  $f_s = 2$  GHz,  $\varsigma = 0.1$  %, here  $B$  and  $\psi_{noise}$  are varied in order to study the relation between range resolution, frequency bandwidth and phase noise. For a target separation of 9 cm, the beat signal range profile for a linear and phase noise added VCO, with a Tx pulse of  $B = 2$  GHz is shown in Fig. 5.14. As it can be seen, the two targets separated by 9 cm is clearly resolved with a linear VCO but becomes unresolvable as the phase noise of the VCO increases. Table. 5.1 summarizes the result. As it can be seen, increasing the phase noise and/or decreasing the bandwidth deteriorates the range resolution.

Table 5.1: Range Resolution for Various Phase Noise and Bandwidth Values

Phase Noise	$B$ (GHz)	$\Delta_R$ (cm)
Linear	2	8
Linear	3	6
Linear	4	4.5
Linear	5	3.5
$\psi_{noise1}^*$	2	9.2
$\psi_{noise1}^*$	3	6.3
$\psi_{noise1}^*$	4	4.8
$\psi_{noise1}^*$	5	3.7
$\psi_{noise2}^*$	2	11.2
$\psi_{noise2}^*$	3	7.6
$\psi_{noise2}^*$	4	5.2
$\psi_{noise2}^*$	5	4

$\psi_{noise1}^* = -65$  dBc/Hz @ 1 kHz,  $-89$  dBc/Hz @ 10 kHz,  $-110$  dBc/Hz @ 100 kHz.  
 $\psi_{noise2}^* = -55$  dBc/Hz @ 1 kHz,  $-75$  dBc/Hz @ 10 kHz,  $-95$  dBc/Hz @ 100 kHz.

### 5.4.2 Cross-Range Resolution

The relation between cross-range resolution, phase noise and aperture length is studied here. The quality of a radar image depends on both range and cross-range resolutions. The criterion for cross-range resolution is that two side-by-side targets should be distinguished. For a narrow-band SAR, the cross-range resolution can be represented by [11]

$$\Delta_{CR} = \frac{H\lambda}{L} \quad (5.19)$$

where  $H$  is the altitude,  $L$  is the aperture length and  $\lambda$  is the wavelength of the radiated signal. Furthermore, the integration angle can be used to represent the ratio of the altitude

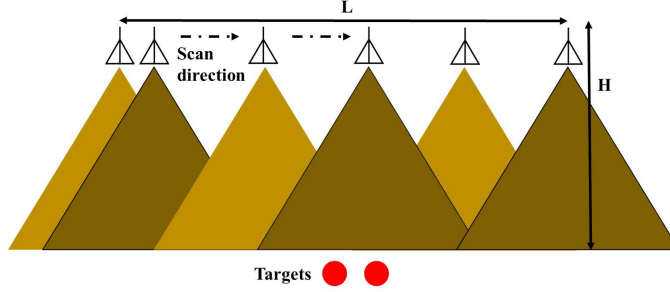


Figure 5.15: LSAR measurement setup.

Table 5.2: Cross-Range Resolution for Various Phase Noise and Integration Angle Values

Phase Noise	$\theta_{IA}$ (deg)	$L$ (cm)	$\Delta_{CR}$ (cm)
Linear	60	40.4	8.5
Linear	70	49	6.9
Linear	80	58.7	5.8
Linear	90	70	5.1
$\psi_{noise1}^*$	60	40.4	8.7
$\psi_{noise1}^*$	70	49	7.3
$\psi_{noise1}^*$	80	58.7	6.1
$\psi_{noise1}^*$	90	70	5.3
$\psi_{noise2}^*$	60	40.4	9.7
$\psi_{noise2}^*$	70	49	8.1
$\psi_{noise2}^*$	80	58.7	7.3
$\psi_{noise2}^*$	90	70	6.2

$\psi_{noise1}^* = -65$  dBc/Hz @ 1 kHz,  $-89$  dBc/Hz @ 10 kHz,  $-110$  dBc/Hz @ 100 kHz.  
 $\psi_{noise2}^* = -55$  dBc/Hz @ 1 kHz,  $-75$  dBc/Hz @ 10 kHz,  $-95$  dBc/Hz @ 100 kHz.

to the aperture length of the measurement, which can be represented by

$$\theta_{IA} = 2 \left( \tan^{-1} \left( \frac{L}{2H} \right) \right) \quad (5.20)$$

However, the cross-range resolution for UWB SAR does not strictly follow (5.19). For UWB radar systems, the cross-range resolution can depend on phase noise. Here, the cross-range

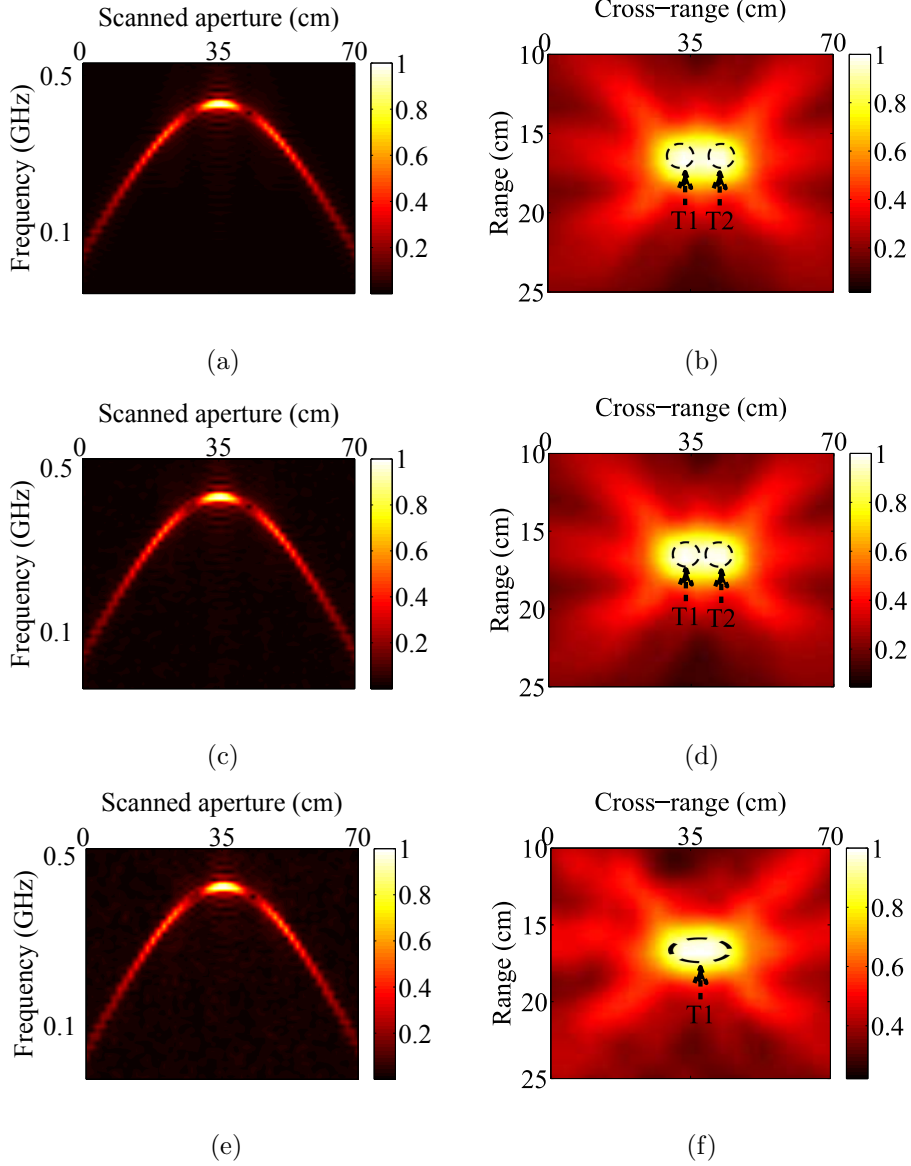


Figure 5.16: Beat signals for a Tx pulse of  $B = 2$  GHz, target separation of 8 cm and  $\theta_{IA}$  of  $70^\circ$ : (a) Raw data, and (b) SAR image for a linear VCO. (c) Raw data, and (d) SAR image for a  $\psi_{noise1}$ \* VCO. (e) Raw data, and (f) SAR image for a  $\psi_{noise2}$ \* VCO.

resolution is studied from the reconstructed SAR images in two steps: First, raw data is generated by moving the radar across the aperture length and scanning a target scene that contains two targets placed side-by-side, as shown in Fig. 5.15. Next, SAR image is reconstructed by applying a modified frequency domain GBP technique [3]. The system parameters for the simulation are  $T_{ramp} = 4$  ns,  $f_s = 2$  GHz,  $\zeta = 0.1$  %,  $B = 2$  GHz,  $H = 35$  cm, in which  $\theta_{IA}$  and  $\psi_{noise}$  are varied in order to study the relation. Table. 5.2 summarizes

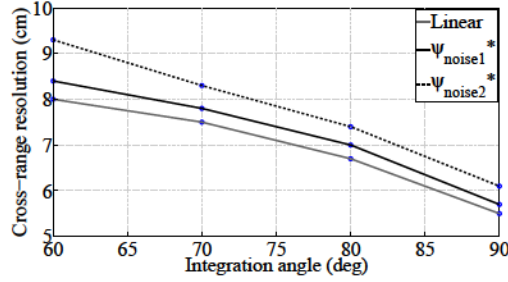


Figure 5.17: Cross-range resolution for various phase noise and integration angle values.

the result. The raw data and SAR images of a linear and phase noise added VCO, with a Tx pulse of  $B = 2$  GHz, target separation of 8 cm and  $\theta_{IA}$  of  $70^\circ$  are shown in Fig. 5.16. As it can be seen, the target signature appears as a hyperbola in the raw data and becomes cluttered as phase noise increases. It can also be seen that the targets are clearly resolved in the linear case and just resolved in the  $\psi_{noise1}^*$  case. However, the targets are not resolved in the  $\psi_{noise2}^*$  case.

In addition, based on the results from Table. 5.2, Fig. 5.17 can be plotted. Then a closed-form expression (5.21) can be empirically derived to establish a relation among achievable cross-range resolution, phase noise and integration angle, represented by

$$\Delta_{CR}(\theta) = p_1\theta^3 + p_2\theta^2 + p_3\theta + p_4 \quad (5.21)$$

where  $p$  are the coefficients described in Table. 5.3. This relation is valid for a pulse bandwidth of 2 GHz, specific phase noise performance (e.g.,  $\psi_{noise1}^*$  and  $\psi_{noise2}^*$ ) and integration angles between  $60^\circ$  to  $90^\circ$ .

The pre-processing simulation led to the formulation of the signal processing procedure, while the post-processing simulation provided an understanding between the radar resolution, frequency bandwidth, phase noise and integration angle.

Table 5.3: Cross-Range Resolution Equation

Coefficients	Linear	$\psi_{noise1}^*$	$\psi_{noise2}^*$
$p_1$	$-1.67 \times 10^{-5}$	$-5 \times 10^{-5}$	$-8.33 \times 10^{-5}$
$p_2$	$-2 \times 10^{-3}$	$9.5 \times 10^{-3}$	0.018
$p_3$	-0.098	-0.66	-1.38
$p_4$	10.3	24.6	45.4

$\psi_{noise1}^* = -65$  dBc/Hz @ 1 kHz,  $-89$  dBc/Hz @ 10 kHz,  $-110$  dBc/Hz @ 100 kHz.

$\psi_{noise2}^* = -55$  dBc/Hz @ 1 kHz,  $-75$  dBc/Hz @ 10 kHz,  $-95$  dBc/Hz @ 100 kHz.

# Chapter 6

## Measurement Results

### 6.1 Calibration Of Target Location

The Rx is affected by scattering from the target(s) and nearby object(s), propagation delay due to the radar components, as well as mutual coupling between the antennas, especially when the antennas are placed in quasi-monostatic configuration. These effects will degrade overall target detection and range accuracy. Therefore, in order to estimate the accurate target location such effects have to be eliminated from the received pulse.

The measurement setup for the range calibration is as follows. A copper rod of 1 cm diameter is used as a calibration target, which is positioned at ranges from 20 cm to 80 cm, with 10 cm increments. Then range profiles ( $S_{rod}^{beat}(x_i, \omega)$ ) are measured for each range position. The range profiles for the calibration target at 20 cm and 30 cm are shown in Fig. 6.1. In the next subsections, the calibration procedure to remove the effect of scattering due to nearby objects, mutual coupling between the antennas, and propagation delay due to radar components are proposed.

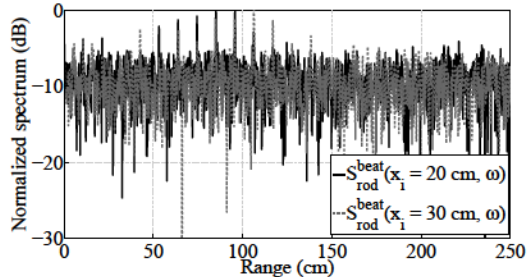


Figure 6.1: Measurement range profiles for the calibration target at 20 cm and 30 cm.

### 6.1.1 Removing Background Noise

The background noise constitutes of scattering from nearby objects, mutual coupling between the antennas, and nonideal behaviour of the radar components. Several background noise removal techniques have been studied under the class of eigenspace methods, such as: singular value decomposition [88], principle component analysis [89], and independent component analysis [90]. However, the eigenspace methods can only be used when certain assumptions are met. For example, the independent component analysis method [90] operates under the assumption that every A-scan signal can be represented by a linear combination of each source. Furthermore, the eigenspace methods require complex statistical calculations in multidimensional spaces. For near real-time imaging, the background subtraction method [91] where two signals are subtracted is more suitable. Two background subtraction methods: ambient subtraction and ambient subtraction with averaging are proposed. Moreover, before calibration is applied, each Rx pulse is multiplied by a Hamming window [62].

In the ambient subtraction method, each A-scan signal is subtracted with the corresponding A-scan signal received without the target, which can be represented by (5.7). Furthermore, in the ambient subtraction with averaging method, a set of A-scan signals are averaged, and are represented by

$$s_{cal}^{beat}(t) = \frac{1}{N} \sum_{i=1}^N \left( s_{tgt}^{beat}(x_i, t) - s_{amb}^{beat}(x_i, t) \right) \quad (6.1)$$

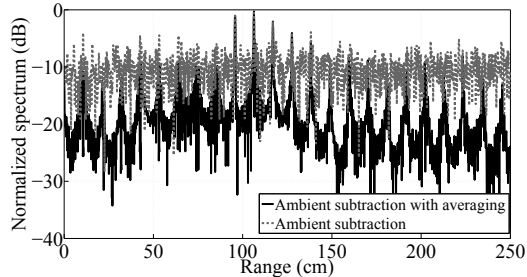


Figure 6.2: Measurement range profiles for the calibration target at 30 cm after: (a) ambient subtraction, and (b) ambient subtraction with averaging.

where  $N$  is the total number of A-scan signals. For a beat signal with SNR of 10 dB, it is observed that increasing the number of pulses for averaging beyond 10 does not provide additional improvements in noise reduction [87]. The range profiles for a target at range 30 cm after ambient subtraction with and without averaging are shown in Fig. 6.2. As it can be seen after ambient subtraction with averaging, a higher SNR is realized. Overall, the background subtraction with averaging method improves the SNR of the received pulse.

### 6.1.2 Removing Propagation Delay

The propagation delay constitutes of radar component delay, signal path length, and VCO sweep nonlinearity. Two propagation delay removal methods: calibration with single zone and multiple zones are proposed. In the calibration with single zone method, each range profile is corrected with a single averaged range error value. Furthermore, in the calibration with multiple zones method, each range profile is corrected with the corresponding range error value of the selected zone. Moreover, before calibration to remove delay is applied, background subtraction with averaging is applied to each received pulse.

The relation between actual and measured range of the calibration target, before and after applying the propagation delay removal methods are shown in Fig. 6.3. Furthermore, interpolation using polynomial functions is used to determine the range values in-between the measurement positions. For the calibration with single zone, an averaged range error value of 102.3 cm is applied to offset all ranges. For the calibration with multiple zones, the

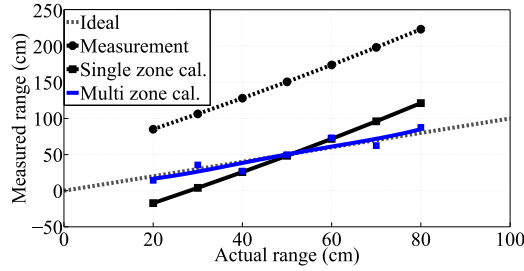


Figure 6.3: The actual vs. measured range for the calibration target, before and after applying the propagation delay removal methods.

averaged range error values of 70.7 cm, 101 cm, and 136 cm are applied to offset the range when the target is positioned in 20 to 40 cm, 40 to 60 cm, and 60 to 80 cm zones respectively. As it can be seen after calibration with multiple zones, the measured range displays a closer match to the ideal range. Moreover, an error analysis is performed, in which the average percentage error between the actual and calibrated target range after calibration with single and multiple zones are  $\pm 38\%$  and  $\pm 8\%$  respectively. Overall, the calibration with multiple zones method provides a more accurate target position.

## 6.2 Reconstruction of SAR Image

The validation of the proposed signal processing procedure using measurement data is presented here. The LSAR measurement setup is as follows. A copper rod of 1 cm diameter is used as a target, which is positioned at  $(x_1, y_1) = (50 \text{ cm}, 40 \text{ cm})$  from the radar system. The radar system is placed on a trolley at a height of 100 cm above the ground. The distance between the antennas and the ground ensure that the reflections from the ground can be frequency-gated. Then the radar is moved along a 100 cm straight path (x-direction) at evenly spaced increments of 10 cm to acquire the raw data  $(S_{tgt}^{beat}(x_i, \omega))$ . The LSAR reconstructed image before and after applying the signal processing procedure is shown in

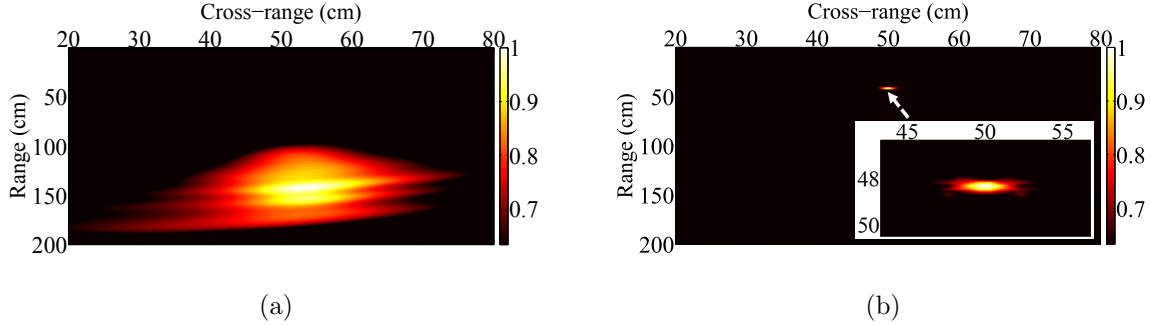


Figure 6.4: LSAR image of a single metal rod: (a) before and (b) after applying the signal processing procedure.

Fig. 6.4. It should be noted that the reconstruction algorithm assumes the target as randomly distributed non-dispersive scatterers. Therefore, the multiple interactions between each scatterer will only be focused if it is present at the same range bin for all the antenna aperture positions in the synthetic aperture. Otherwise, the artifacts associated to the multiple interactions will blur and create inaccurate target detection in the reconstructed SAR image. As it can be seen, only after applying the proposed signal processing procedure can the target be clearly focused and accurately identified in the LSAR image.

### 6.3 LSAR Image Reconstruction

The LSAR image reconstruction using GBP technique [3] is adapted here for beat frequencies. In LSAR, the radar system is moved on a straight line to illuminate the target scene. The received signals are denoted as raw data, and the image is reconstructed. The first target scene consists of three identical metal rods, of diameter 1 cm, positioned at  $(x_1, y_1) = (40 \text{ cm}, 80 \text{ cm})$ ,  $(x_2, y_2) = (50 \text{ cm}, 73 \text{ cm})$ ,  $(x_3, y_3) = (60 \text{ cm}, 80 \text{ cm})$ , as shown in Fig. 6.5(a). The second target scene consists of a metal frame chair ( $60 \times 75 \text{ cm}^2$ ), in which its center is positioned at  $(x_1, y_1, z_1) = (50 \text{ cm}, 40 \text{ cm}, 70 \text{ cm})$ , as shown in Fig. 6.5(b). For the first target scene, the radar system is at a height of 100 cm above the ground, and moved along a

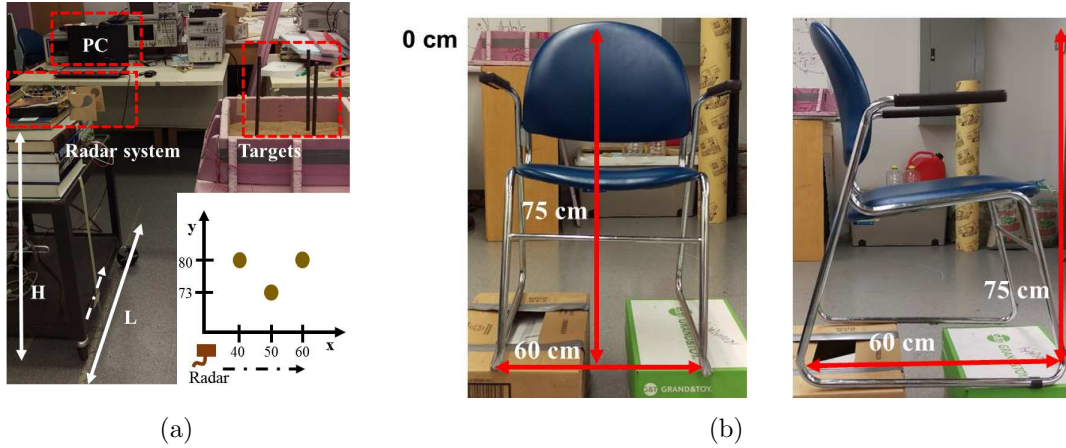


Figure 6.5: LSAR image scene of: (a) three metal rods, and (b) the chair.

100 cm straight path (x-direction) at evenly spaced increments of 10 cm to acquire the raw data. For the second target scene, the radar system is also moved along a 100 cm straight path at evenly spaced increments of 10 cm. To project the chair volume onto two orthogonal planes,  $xz$  and  $yz$  planes, the raw data (B-scan) is collected at four different heights of the target (70 cm, 80 cm, 90 cm, 100 cm). The 2-D front view image in the  $xz$  plane is obtained by a coherent integration of the volumetric data in the  $y$ -direction. Alternatively, the 2-D side view image in the  $yz$  plane is formed by a coherent integration in the  $x$ -direction. The LSAR reconstructed images, with a threshold level of half of the peak amplitude, are shown in Fig. 6.6(a), 6.6(b) and 6.6(c) respectively. As it can be seen after LSAR processing, frequency is translated to depth (range), which localizes the target(s) in the target scene. Also, targets have been clearly identified and accurately positioned, and the 2-D images of the chair are clearly illustrated.

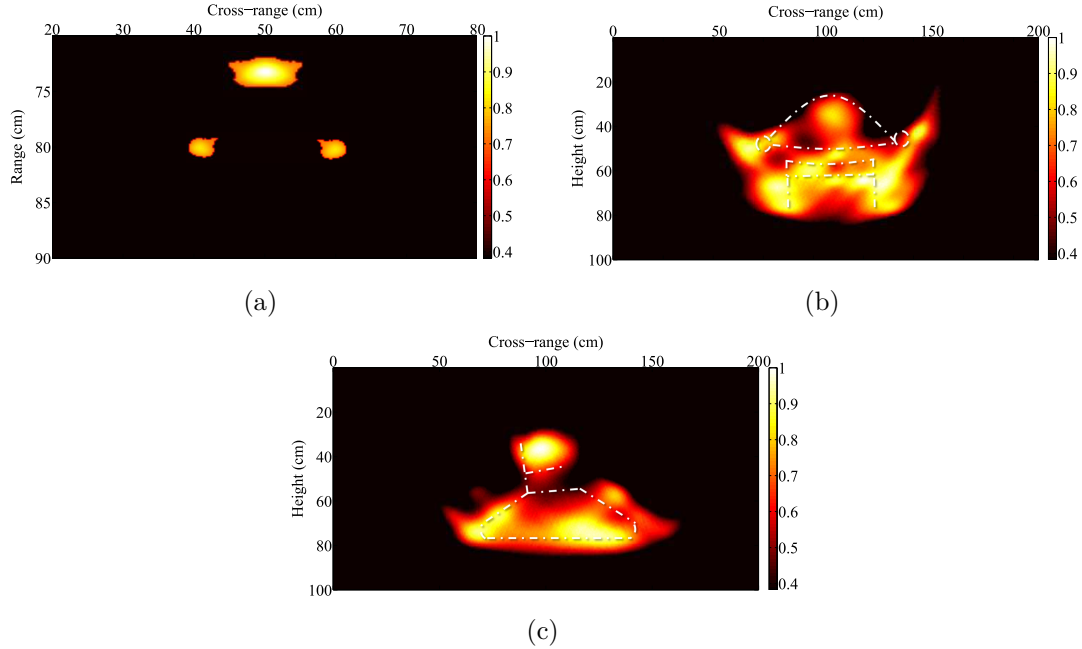


Figure 6.6: LSAR image of: (a) three metal rods, (b) front view and (c) side view of the chair.

## 6.4 CSAR Image Reconstruction

The CSAR image reconstruction technique [11] is also adapted here for beat frequencies. In CSAR, the radar system is moved in a circular path around the target scene. The first target scene consists of three identical metal nails, each of diameter 1 cm, positioned at  $(x_1, y_1) = (0 \text{ cm}, 0 \text{ cm})$ ,  $(x_2, y_2) = (-4.5 \text{ cm}, 4 \text{ cm})$ ,  $(x_3, y_3) = (4.5 \text{ cm}, 4 \text{ cm})$ , as shown in Fig. 6.7(a). The second target scene consists of eleven identical nails, each of diameter 1 cm, arranged to spell out the letters UA, as shown in Fig. 6.7(b). The radar system remains stationary on a trolley at a height of 100 cm above ground. The nails are fixed on a rotating platform, in which the range profiles of the target scene are acquired over the radar trajectory at every 10 degrees. The CSAR reconstructed images, with a threshold level of half of the peak amplitude, are shown in Fig. 6.8(a) and 6.8(b) respectively. As it can be seen after CSAR processing, frequency is translated to depth (range), which localizes the target(s) in the image scene. Likewise, targets have been clearly recognized and accurately located in the CSAR images.

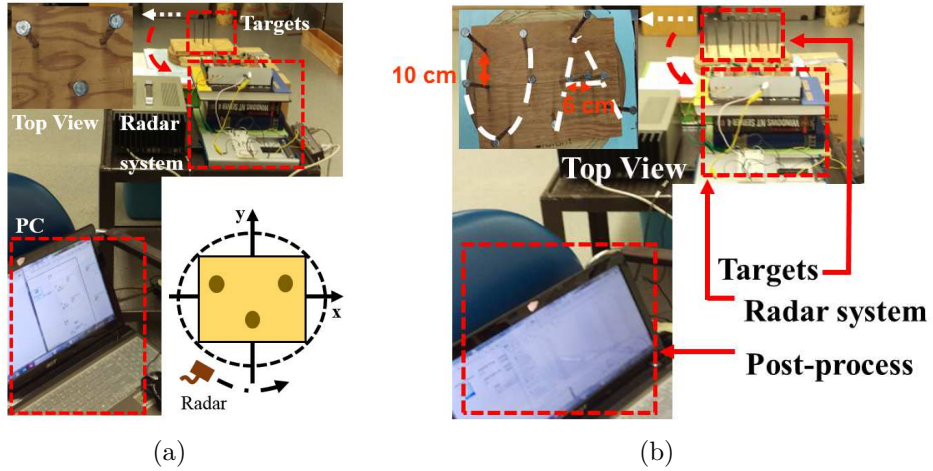


Figure 6.7: CSAR image scene of: (a) three metal nails, and (b) eleven metal nails spelling out UA.

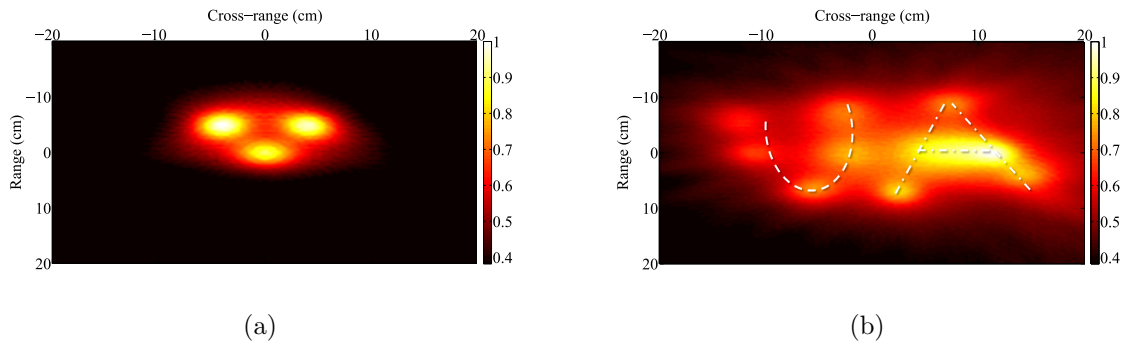


Figure 6.8: CSAR image of: (a) three metal nails, and (b) eleven metal nails spelling out UA.

# Chapter 7

## Conclusion

### 7.1 Summary

The combination of FMCW technology with SAR technique is a highly sought after method as it leads to a compact and cost effective high resolution near distance imaging system. In this thesis, an S-band FMCW SAR system for near distance imaging has been designed, implemented and validated. The ADS system simulation is presented to provide insightful information about the influence of component parameters on the overall system performance. Then the frequency and time domain measurements are performed to characterize and verify the subsystem and system performances. A modified bow-tie antenna with low XP and miniaturization is shown to improve the radar image resolution. Then software simulations are implemented to study the effects of deramp, phase noise of the transmitted signal and its sweep nonlinearity on the beat spectrum, as well as validate the proposed mitigation methods. The effects of frequency bandwidth, phase noise and integration angle on radar resolution have also been verified. System calibration methods have also been developed to improve the range accuracy and the SNR. Finally, a signal processing procedure is proposed, which is validated with the measured FMCW SAR data and is shown to be compatible with both LSAR and CSAR image reconstruction.

## 7.2 Future Work

Possible future work for the S-band FMCW SAR system includes:

1. Demonstrate the working of the S-band FMCW SAR system to detect and image ice-cracks for ice-road applications. The development of this S-band FMCW SAR system enables a simple, low cost and miniaturized system design for a wide range of near distance imaging applications that may not be possible with previous existing architectures.
2. Demonstrate the working of the S-band FMCW SAR system to identify material dielectric constant. Dielectric materials are characterized by their relative permittivity and loss tangent at various frequencies. These parameters can be measured using a non-contact method, for free space material characterization, in which the attenuated Rx signal is measured to determine the attenuation and propagation constants.
3. Modify the S-band FMCW SAR system to integrate hardware range gate capability for through-wall applications. It has been shown in [33-35], that heterodyne transceiver architectures are used to implement range gate based on narrow-band filters, which overcomes the strong scattered signal from the wall that will saturate the Rx, limit the dynamic range and limit the Rx sensitivity. Therefore, the modified FMCW SAR system will be used with the signal processing procedure developed from this thesis, for through-wall imaging applications.

# Bibliography

- [1] N. Galin, A. Worby, T. Markus, C. Leuschen, and P. Gogineni, “Validation of Airborne FMCW Radar Measurements of Snow Thickness Over Sea Ice in Antarctica,” *IEEE Transactions on Geoscience and Remote Sensing*, vol. 50, no. 1, pp. 3–12, Jan 2012.
- [2] R. Iglesias, A. Aguasca, X. Fabregas, J. J. Mallorqui, D. Monells, C. Lopez-Martnez, and L. Pipia, “Ground-Based Polarimetric SAR Interferometry for the Monitoring of Terrain Displacement Phenomena; Part II: Applications,” *IEEE Journal of Selected Topics in Applied Earth Observations and Remote Sensing*, vol. 8, no. 3, pp. 994–1007, March 2015.
- [3] Y. Luo, H. Song, R. Wang, Y. Deng, F. Zhao, and Z. Xu, “Arc FMCW SAR and Applications in Ground Monitoring,” *IEEE Transactions on Geoscience and Remote Sensing*, vol. 52, no. 9, pp. 5989–5998, Sept 2014.
- [4] G. L. Charvat, L. C. Kempell, and C. Coleman, “A Low-Power High-Sensitivity X-Band Rail SAR Imaging System,” *IEEE Antennas and Propagation Magazine*, vol. 50, no. 3, pp. 108–115, June 2008.
- [5] S. Ayhan, S. Scherr, P. Pahl, T. Kayser, M. Pauli, and T. Zwick, “High-Accuracy Range Detection Radar Sensor for Hydraulic Cylinders,” *IEEE Sensors Journal*, vol. 14, no. 3, pp. 734–746, March 2014.
- [6] C. Baer, T. Jaeschke, N. Pohl, and T. Musch, “Contactless Detection of State Parameter Fluctuations of Gaseous Media Based on an mm-Wave FMCW Radar,” *IEEE Transactions on Instrumentation and Measurement*, vol. 64, no. 4, pp. 865–872, April 2015.
- [7] G. Wang, C. Gu, T. Inoue, and C. Li, “A Hybrid FMCW-Interferometry Radar for Indoor Precise Positioning and Versatile Life Activity Monitoring,” *IEEE Transactions on Microwave Theory and Techniques*, vol. 62, no. 11, pp. 2812–2822, Nov 2014.
- [8] B. Boukari, E. Moldovan, S. Affes, K. Wu, R. G. Bosisio, and S. O. Tatu, “Six-Port FMCW Collision Avoidance Radar Sensor Configurations,” in *Electrical and Computer Engineering, 2008. CCECE 2008. Canadian Conference, Niagara Falls, Ont*, May 2008, pp. 000 305–000 308.
- [9] A. Polychronopoulos, A. Amditis, N. Floudas, and H. Lind, “Integrated Object and Road Border Tracking Using 77 GHz Automotive Radars,” *IEE Proceedings - Radar, Sonar and Navigation*, vol. 151, no. 6, pp. 375–381, Dec 2004.

- [10] M. E. Russell, A. Crain, A. Curran, R. A. Campbell, C. A. Drubin, and W. F. Miccili, "Millimeter-Wave Radar Sensor for Automotive Intelligent Cruise Control (ICC)," *IEEE Transactions on Microwave Theory and Techniques*, vol. 45, no. 12, pp. 2444–2453, Dec 1997.
- [11] M. Soumekh, *Synthetic Aperture Radar Signal Processing: With MATLAB Algorithms*. Hoboken, NJ: Wiley, 1999.
- [12] A. Meta, P. Hooeboom, and L. P. Ligthart, "Signal Processing for FMCW SAR," *IEEE Transactions on Geoscience and Remote Sensing*, vol. 45, no. 11, pp. 3519–3532, Nov 2007.
- [13] —, "Non-Linear Frequency Scaling Algorithm for FMCW SAR Data," in *2006 European Radar Conference, Manchester, UK*, Sept 2006, pp. 9–12.
- [14] A. Ribalta, "Time-Domain Reconstruction Algorithms for FMCW-SAR," *IEEE Geoscience and Remote Sensing Letters*, vol. 8, no. 3, pp. 396–400, May 2011.
- [15] W. G. Carrara, R. S. Goodman, and R. M. Majewski, *Spotlight Synthetic Aperture Radar: Signal Processing Algorithms*. Boston, MA: Artech House, 1995.
- [16] E. Hegazi, H. Sjoland, and A. Abidi, "A Filtering Technique to Lower Oscillator Phase Noise," in *Solid-State Circuits Conference, 2001. Digest of Technical Papers. ISSCC. 2001 IEEE International*, Feb 2001, pp. 364–365.
- [17] H. Kim, S. Ryu, Y. Chung, J. Choi, and B. Kim, "A Low Phase-Noise CMOS VCO with Harmonic Tuned LC Tank," *IEEE Transactions on Microwave Theory and Techniques*, vol. 54, no. 7, pp. 2917–2924, July 2006.
- [18] H.-G. Park, B. Kim, and Y.-S. Kim, "VCO Nonlinearity Correction Scheme For A Wideband FMCW Radar," *Microwave and Optical Technology Letters*, vol. 25, no. 4, pp. 266–269, 2000.
- [19] M. El-Shennawy, N. Joram, and F. Ellinger, "Fractional-N PLL Optimization for Highly Linear Wideband Chirp Generation for FMCW Radars," in *2015 German Microwave Conference, Nuremberg, Germany*, March 2015, pp. 248–251.
- [20] A. Meta, "Signal Processing of FMCW Synthetic Aperture Radar Data," Ph.D. dissertation, Delft University of Technology, Dept. Elect. Comput. Eng., Delft, NL, 2006.
- [21] A. Anghel, G. Vasile, R. Cacoveanu, C. Ioana, and S. Ciochina, "Nonlinearity Correction Algorithm for Wideband FMCW Radars," in *21st European Signal Processing Conference (EUSIPCO 2013), Marrakech, Morocco*, Sept 2013, pp. 1–5.
- [22] M. Dudek, D. Kissinger, R. Weigel, and G. Fischer, "A Millimeter-Wave FMCW Radar System Simulator for Automotive Applications Including Nonlinear Component Models," in *Radar Conference (EuRAD), 2011 European*, Oct 2011, pp. 89–92.

- [23] M. Dudek, I. Nasr, D. Kissinger, R. Weigel, and G. Fischer, “The Impact of Phase Noise Parameters on Target Signal Detection in FMCW-Radar System Simulations for Automotive Applications,” in *Proceedings of 2011 IEEE CIE International Conference on Radar*, vol. 1, Oct 2011, pp. 494–497.
- [24] S. Scheiblhofer, M. Treml, S. Schuster, R. Feger, and A. Stelzer, “A Versatile FMCW Radar System Simulator for Millimeter-Wave Applications,” in *Radar Conference, 2008. EuRAD 2008. European*, Oct 2008, pp. 447–450.
- [25] C. Krnfeldt, A. Pden, A. Bazzi, G. E. H. Shhad, M. Abbas, and T. Chonavel, “77 GHz ACC Radar Simulation Platform,” in *Intelligent Transport Systems Telecommunications, (ITST), 2009 9th International Conference on*, Oct 2009, pp. 209–214.
- [26] D. K. Barton, *Modern Radar System Analysis*. Boston, MA: Artech House, 1988.
- [27] S. T. Tseng, Y. H. Kao, C. C. Peng, J. Y. Liu, S. C. Chu, G. F. Hong, C. H. Hsieh, K. T. Hsu, W. T. Liu, Y. H. Huang, S. Y. Huang, and T. S. Chu, “A 65-nm CMOS Low-Power Impulse Radar System for Human Respiratory Feature Extraction and Diagnosis on Respiratory Diseases,” *IEEE Transactions on Microwave Theory and Techniques*, vol. 64, no. 4, pp. 1029–1041, April 2016.
- [28] L. Liu, X. Xia, S. Ye, J. Shao, and G. Fang, “Development of a Novel, Compact, Balanced, Micropower Impulse Radar for Nondestructive Applications,” *IEEE Sensors Journal*, vol. 15, no. 2, pp. 855–863, Feb 2015.
- [29] K. K. M. Chan, A. E. C. Tan, and K. Rambabu, “Circularly Polarized Ultra-Wideband Radar System for Vital Signs Monitoring,” *IEEE Transactions on Microwave Theory and Techniques*, vol. 61, no. 5, pp. 2069–2075, May 2013.
- [30] E. Hyun, Y. S. Jin, and J. Lee, “Development of 24GHz FMCW Level Measurement Radar System,” in *2014 IEEE Radar Conference*, May 2014, pp. 0796–0799.
- [31] G. L. Charvat, *Small and Short-Range Radar Systems*. Boca Raton, FL: CRC Press, 2014.
- [32] M. I. Skolnik, *Radar Handbook 3rd ed.* New York City, NY: McGraw-Hill, 2008.
- [33] G. L. Charvat, L. C. Kempel, E. J. Rothwell, C. M. Coleman, and E. L. Mokole, “A Through-Dielectric Ultrawideband (UWB) Switched-Antenna-Array Radar Imaging System,” *IEEE Transactions on Antennas and Propagation*, vol. 60, no. 11, pp. 5495–5500, Nov 2012.
- [34] —, “A Through-Dielectric Radar Imaging system,” *IEEE Transactions on Antennas and Propagation*, vol. 58, no. 8, pp. 2594–2603, Aug 2010.
- [35] G. Charvat, “A Low-Power Radar Imaging System,” Ph.D. dissertation, Michigan State University, Dept. Elect. Comput. Eng., East Lansing, MI, USA, 2007.

- [36] A. Anghel, G. Vasile, R. Căcoveanu, C. Ioana, and S. Ciochina, "Short-Range FMCW X-Band Radar Platform for Millimetric Displacements Measurement," in *2013 IEEE International Geoscience and Remote Sensing Symposium - IGARSS*, July 2013, pp. 1111–1114.
- [37] G. L. Charvat and L. C. Kempel, "Low-Cost, High Resolution X-Band Laboratory Radar System for Synthetic Aperture Radar Applications," in *2006 IEEE International Conference on Electro/Information Technology, East Lansing, MI*, May 2006, pp. 529–531.
- [38] R. Dahlbck, T. Bryllert, G. Granstrm, M. Ferndahl, V. Drakinskiy, and J. Stake, "Compact 340 GHz Homodyne Transceiver Modules for FMWC Imaging Radar Arrays," in *2016 IEEE MTT-S International Microwave Symposium (IMS)*, May 2016, pp. 1–4.
- [39] M. I. Skolnik, *Introduction to Radar Systems*. New York City, NY: McGraw-Hill, 1980.
- [40] W. Jiang, S. R. Pennock, and P. R. Shepherd, "FMCW Radar Range Performance Improvement with Modified Adaptive Sampling Method," *IEEE Geoscience and Remote Sensing Letters*, vol. 9, no. 4, pp. 668–671, July 2012.
- [41] S. Scheiblhofer, S. Schuster, and A. Stelzer, "Signal Model and Linearization for Nonlinear Chirps in FMCW Radar SAW-ID Tag Request," *IEEE Transactions on Microwave Theory and Techniques*, vol. 54, no. 4, pp. 1477–1483, June 2006.
- [42] D. M. Pozar, *Microwave Engineering*. New York City, NY: John Wiley and Sons Inc, 2005.
- [43] B. R. Mahafza, *Radar Systems Analysis and Design Using MATLAB*. Boca Raton, FL: Chapman and Hall, 2005.
- [44] G. L. Charvat, *Small and Short-Range Radar Systems*. Boca Raton, FL: CRC Press, 2014.
- [45] S. O. Piper, "Receiver Frequency Resolution for Range Resolution in Homodyne FMCW Radar," in *Telesystems Conference, 1993. 'Commercial Applications and Dual-Use Technology', Conference Proceedings., National*, Jun 1993, pp. 169–173.
- [46] S. Piper, "Homodyne FMCW Radar Range Resolution Effects with Sinusoidal Nonlinearities in the Frequency Sweep," in *Radar Conference, 1995., Record of the IEEE 1995 International*, May 1995, pp. 563–567.
- [47] T. Yang, Y. Bayram, and J. L. Volakis, "Hybrid Analysis of Electromagnetic Interference Effects on Microwave Active Circuits Within Cavity Enclosures," *IEEE Transactions on Electromagnetic Compatibility*, vol. 52, no. 3, pp. 745–748, Aug 2010.
- [48] M. Dudek, I. Nasr, D. Kissinger, R. Weigel, and G. Fischer, "The Impact of Phase Noise Parameters on Target Signal Detection in FMCW-Radar System Simulations for Automotive Applications," in *Proceedings of 2011 IEEE CIE International Conference on Radar, Chengdu, China*, vol. 1, Oct 2011, pp. 494–497.

- [49] P. D. L. Beasley, “The Influence of Transmitter Phase Noise on FMCW Radar Performance,” in *2006 European Microwave Conference, Manchester, UK*, Sept 2006, pp. 1810–1813.
- [50] M. Odyniec, *RF and Microwave Oscillator Design*. Boston, MA: Artech House, 2002.
- [51] E. S. Ferre-Pikal, J. R. Vig, J. C. Camparo, L. S. Cutler, L. Maleki, W. J. Riley, S. R. Stein, C. Thomas, F. L. Walls, and J. D. White., “Draft Revision of IEEE Std 1139-1988 Standard Definitions of Physical Quantities for Fundamental, Frequency and Time Metrology-Random Instabilities.” *Frequency Control Symposium, 1997., Proceedings of the 1997 IEEE International*, pp. 338–357, May 1997.
- [52] D. B. Leeson, “A Simple Model of Feedback Oscillator Noise Spectrum,” *Proceedings of the IEEE*, vol. 54, no. 2, pp. 329–330, Feb 1966.
- [53] T. Feng, H. Xianhe, W. Wei, and F. Wei, “Analysis of Phase Noise and Timing Jitter in Crystal Oscillator,” in *Communications, Circuits and Systems, 2007. ICCAS 2007. International Conference on*, July 2007, pp. 1103–1106.
- [54] Industry Canada Telecommunications Policy branch, “Canadian Table of Frequency Allocations 9 kHz to 275 GHz,” pp. 1–113, Jan 2006, <http://www.ic.gc.ca/eic/site/smt-gst.nsf/eng/sf10759.html>.
- [55] Industry Canada Spectrum Engineering branch, “Devices Using Ultra-Wideband (UWB) Technology,” pp. 1–19, Mar 2009, <https://www.ic.gc.ca/eic/site/smt-gst.nsf/eng/sf09347.html>.
- [56] —, “Radio Spectrum Inventory,” pp. 142–149, Sept 2010, <https://www.ic.gc.ca/eic/site/smt-gst.nsf/eng/sf10333.html>.
- [57] R. Undheim, “Design of a Linear FMCW Radar Synthesizer with Focus on Phase Noise,” Master’s thesis, Norwegian University of Science and Technology, Dept. Elect. Comput. Eng., Norway, 2012.
- [58] A. Victor and J. Nath, “An analytic technique for trade-off of noise measure and mismatch loss for low noise amplifier design,” in *2010 IEEE 11th Annual Wireless and Microwave Technology Conference (WAMICON)*, April 2010, pp. 1–4.
- [59] Agilent Technologies, “Spectrum Analysis Basics: Application Note 150,” pp. 1–89, Feb 2014, <http://cp.literature.agilent.com/litweb/pdf/5952-0292.pdf>.
- [60] J. S. Hong, *Microstrip Filters For RF/Microwave Applications 2nd ed.* Hoboken, NJ: Wiley, 2001.
- [61] X. Qing, Z. N. Chen, and M. Y. W. Chia, “Dual Elliptically Tapered Antipodal Slot Antenna Loaded by Curved Terminations for Ultra-Wideband applications,” *Radio Science*, vol. 41, no. 6, pp. 1–14, Dec 2006.

- [62] B. R. Mahafza and A. Z. Elsherbeni, *Simulations for Radar Systems Design*. Boca Raton, FL: Chapman and Hall, 2004.
- [63] J. X. Yeo, Y. H. Lee, and J. T. Ong, "Radar Measured Rain Attenuation With Proposed ZR Relationship At A Tropical Location," *AEU - International Journal of Electronics and Communications*, vol. 69, no. 1, pp. 458–461, October 2014.
- [64] B. Polat and P. Meincke, "A Forward Model for Ground Penetrating Radar Imaging of Buried Perfect Electric Conductors within the Physical Optics Approximation," *AEU - International Journal of Electronics and Communications*, vol. 58, no. 5, pp. 362–366, December 2004.
- [65] M. G. Amin, *Through-The-Wall Radar Imaging*. Boca Raton, FL: CRC Press, 2011.
- [66] H. S. Lui, A. Fhager, and M. Persson, "On the Forward Scattering of Microwave Breast Imaging," *International Journal of Biomedical Imaging*, December 2012.
- [67] A. J. Blanchard and B. R. Jean, "Antenna effects in depolarization measurements," *IEEE Transactions on Geoscience and Remote Sensing*, vol. GE-21, no. 1, pp. 113–117, Jan 1983.
- [68] J. D. Taylor, *Introduction to Ultra-Wideband Radar Systems*. Boca Raton, FL: CRC Press, 1994.
- [69] A. Gorai, A. Karmakar, M. Pal, and R. Ghatak, "A Super Wideband Chebyshev Tapered Antipodal Vivaldi Antenna," *AEU - International Journal of Electronics and Communications*, vol. 69, no. 9, pp. 1328–1333, June 2015.
- [70] M. Khorshidi and M. Kamyab, "New Exponential TEM Horn Antenna With Binomial Impedance Taper," *AEU - International Journal of Electronics and Communications*, vol. 64, no. 11, pp. 1073–1077, December 2010.
- [71] Y. K. Kwag, A. D. Hassanein, and D. J. Edwards, "A High-Directive Bowtie Radar Antenna With A Pyramidal Reflector For Ultra-Wideband Radar Imaging Applications," *Microwave Optical Technology Letters*, vol. 51, no. 2, pp. 389–390, December 2006.
- [72] C. Balanis, *Antenna Theory 3rd ed.* New York City, NY: John Wiley Sons, 2005.
- [73] K. Kiminami, A. Hirata, and T. Shiozawa, "Double-Sided Printed Bow-Tie Antenna for UWB Communications," *IEEE Antennas and Wireless Propagation Letters*, vol. 3, no. 1, pp. 152–153, Dec 2004.
- [74] T. Karacolak and E. Topsakal, "A Double-Sided Rounded Bow-Tie Antenna (DSRBA) for UWB Communication," *IEEE Antennas and Wireless Propagation Letters*, vol. 5, no. 1, pp. 446–449, Dec 2006.
- [75] C. C. Lin, "Compact Bow-Tie Quasi-Self-Complementary Antenna for UWB Applications," *IEEE Antennas and Wireless Propagation Letters*, vol. 11, pp. 987–989, 2012.

- [76] O. Yurduseven, D. Smith, and M. Elsdon, "Printed Slot Loaded Bow-Tie Antenna With Super Wideband Radiation Characteristics for Imaging Applications," *IEEE Transactions on Antennas and Propagation*, vol. 61, no. 12, pp. 6206–6210, Dec 2013.
- [77] M. Jalilvand, X. Li, J. Kowalewski, and T. Zwick, "Broadband Miniaturised Bow-Tie Antenna for 3D Microwave Tomography," *Electronics Letters*, vol. 50, no. 4, pp. 244–246, February 2014.
- [78] J. Yang and A. Kishk, "A Novel Low-Profile Compact Directional Ultra-Wideband Antenna: The Self-Grounded Bow-Tie Antenna," *IEEE Transactions on Antennas and Propagation*, vol. 60, no. 3, pp. 1214–1220, March 2012.
- [79] L. Marantis and P. Brennan, "A CPW-Fed Bow-Tie Slot Antenna With Tuning Stub," in *2008 Loughborough Antennas and Propagation Conference*, March 2008, pp. 389–392.
- [80] J. R. James and P. S. Hall, *Handbook of Microstrip Antennas*. IET, 1989.
- [81] L. Li, A. E. C. Tan, K. Jhamb, and K. Rambabu, "Characteristics of Ultra-Wideband Pulse Scattered From Metal Planar Objects," *IEEE Transactions on Antennas and Propagation*, vol. 61, no. 6, pp. 3197–3206, June 2013.
- [82] G. Quintero, J. F. Zurcher, and A. K. Skrivervik, "System Fidelity Factor: A New Method for Comparing UWB Antennas," *IEEE Transactions on Antennas and Propagation*, vol. 59, no. 7, pp. 2502–2512, July 2011.
- [83] M. Kanda, "Transients In A Resistively Loaded Linear Antenna Compared With Those In A Conical Antenna And A TEM Horn," *IEEE Transactions on Antennas and Propagation*, vol. 28, no. 1, pp. 132–136, Jan 1980.
- [84] V. K. Ingle and J. G. Proakis, *Digital Signal Processing using MATLAB 2nd ed.* Toronto, Ont: Thomson, 2007.
- [85] X. Mao, H. Yang, and H. Wang, "Behavioral Modeling and Simulation of Jitter and Phase Noise in fractional-N PLL Frequency Synthesizer," in *Behavioral Modeling and Simulation Conference, 2004. BMAS 2004. Proceedings of the 2004 IEEE International, San-Jose, CA*, Oct 2004, pp. 25–30.
- [86] P. P. Vaidyanathan, *The Theory of Linear Prediction*. San Rafael, CA: Morgan Claypool, 2008.
- [87] D. Oloumi, J. W. Ting, and K. Rambabu, "Design of Pulse Characteristics for Near-Field UWB-SAR Imaging," *IEEE Transactions on Microwave Theory and Techniques*, vol. 64, no. 8, pp. 2684–2693, Aug 2016.
- [88] F. H. C. Tivive, A. Bouzerdoun, and M. G. Amin, "An SVD-Based Approach for Mitigating Wall Reflections in Through-the-Wall Radar Imaging," in *2011 IEEE RadarCon (RADAR)*, May 2011, pp. 519–524.

- [89] P. Verma and A. Gaikwad, "Analysis of Clutter Reduction Techniques for Through Wall Imaging in UWB Range," *Progress In Electromagnetics Research*, vol. 17, pp. 29–48, 2009.
- [90] A. N. Gaikwad, D. Singh, and M. J. Nigam, "Application of Clutter Reduction Techniques for Detection of Metallic and Low Dielectric Target Behind the Brick Wall by Stepped Frequency Continuous Wave Radar in Ultra-Wideband Range," *IET Radar, Sonar Navigation*, vol. 5, no. 4, pp. 416–425, April 2011.
- [91] D. Oloumi, "Ultra-Wideband Synthetic Aperture Radar Imaging: Theory and Applications," Ph.D. dissertation, University of Alberta, Dept. Elect. Comput. Eng., Alberta, CAN, 2016.

# Appendix A

## Datasheets

### A.1 VCO: ROS-3800-119+

Electrical Specifications

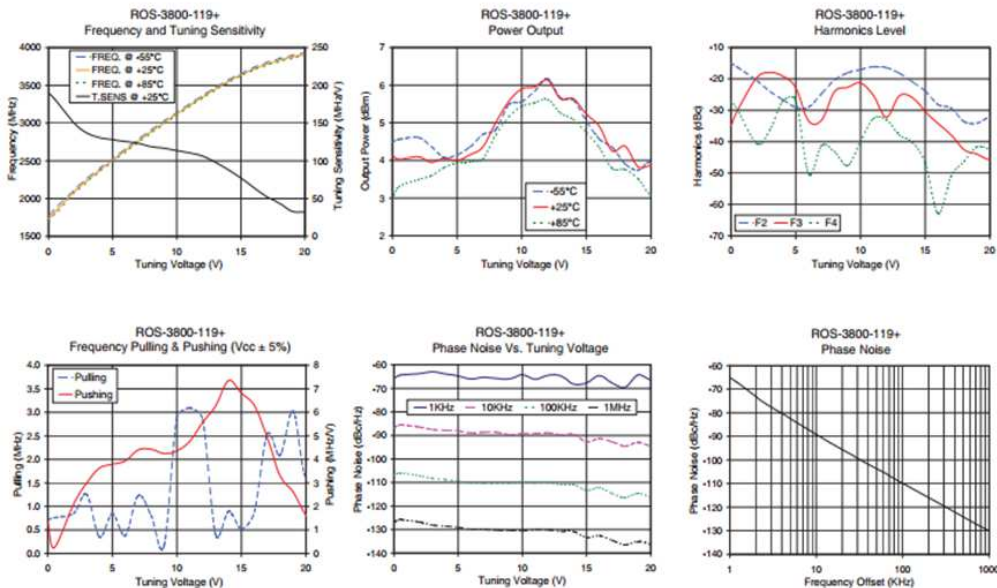
MODEL NO.	FREQ. (MHz)		POWER OUTPUT (dBm)	PHASE NOISE dBc/Hz SSB at offset frequencies, kHz				TUNING				NON HARMONIC SPOURIOUS (dBc)	HARMONICS (dBc)		PULLING pk-pk @ 12 dB (MHz)	PUSHING (MHz/V)	DC OPERATING POWER		
	Min.	Max.		Typ.	1	10	100	1000	VOLTAGE RANGE (V)	SENSITIVITY (MHz/V)	PORT CAP (pF)		3 dB MODULATION BANDWIDTH (MHz)	Typ.			Max.	Typ.	Typ.
ROS-3800-119+	1900	3700	+5	-65	-89	-110	-130	0.5	20	60-150	50	70	-90	-22	-10	2	4.5	6	55

**Pin Connections**

RF OUT	10
VCC	14
V-TUNE	2
GROUND	1, 3, 4, 5, 6, 7, 8, 9, 11, 12, 13, 15, 16

**Maximum Ratings**

Operating Temperature -55°C to 85°C  
 Storage Temperature -55°C to 100°C  
 Absolute Max. Supply Voltage (Vcc) 7V  
 Absolute Max. Tuning Voltage (Vtune) 21V  
 All specifications 50 ohm system  
 Permanent damage may occur if any of these limits are exceeded.



## A.2 PA: GALI-84+

### Electrical Specifications at 25°C and 100mA, unless noted

Parameter		Min.	Typ.	Max.	Units	Cpk
Frequency Range*		DC		6	GHz	
Gain	f=0.1 GHz	24.3	25.6	26.9	dB	≥1.5
	f=1 GHz	—	22.7	—		
	f=2 GHz	18.2	19.2	20.2		
	f=3 GHz	—	16.7	—		
	f=4 GHz	14.3	15.0	15.8		
	f=6 GHz	—	11.8	—		
Magnitude of Gain Variation versus Temperature (values are negative)	f=0.1 GHz	—	0.0025	—	dB/°C	
	f=1 GHz	—	0.0036	—		
	f=2 GHz	—	0.0045	0.0090		
	f=3 GHz	—	0.0057	—		
	f=4 GHz	—	0.0074	—		
	f=6 GHz	—	0.0148	—		
Input Return Loss	f=0.1 GHz	—	25.8	—	dB	
	f=1 GHz	—	21.2	—		
	f=2 GHz	14.0	18.0	—		
	f=3 GHz	—	15.6	—		
	f=4 GHz	—	14.7	—		
	f=6 GHz	—	16.7	—		
Output Return Loss	f=0.1 GHz	—	16.3	—	dB	
	f=1 GHz	—	11.0	—		
	f=2 GHz	6.0	8.9	—		
	f=3 GHz	—	9.0	—		
	f=4 GHz	—	9.7	—		
	f=6 GHz	—	8.4	—		
Reverse Isolation	f=2 GHz	22	26.5	—	dB	
Output Power @ 1 dB compression	f=0.1 GHz	20.8	21.9	—	dBm	≥1.5
	f=1 GHz	20.4	21.5	—		
	f=2 GHz	20.1	21.2	—		
	f=3 GHz	—	20.9	—		
	f=4 GHz	—	19.2	—		
	f=6 GHz	—	15.5	—		
Saturated Output Power (at 3dB compression)	f=0.1 GHz		23.0		dBm	
	f=1 GHz		22.6			
	f=2 GHz		22.1			
	f=3 GHz		21.7			
	f=4 GHz		20.3			
	f=6 GHz		17.1			
Output IP3	f=0.1 GHz	33.8	37.6	—	dBm	≥1.5
	f=1 GHz	34.0	37.8	—		
	f=2 GHz	34.2	38.0	—		
	f=3 GHz	—	37.4	—		
	f=4 GHz	—	34.7	—		
	f=6 GHz	—	32.7	—		
Noise Figure	f=0.1 GHz		4.2		dBm	≥1.5
	f=1 GHz		4.4			
	f=2 GHz		4.4			
	f=3 GHz		4.4			
	f=4 GHz		4.6			
	f=6 GHz		5.3			
Group Delay	f=2 GHz		94		psec	
Recommended Device Operating Current			100		mA	
Device Operating Voltage		5.4	5.8	6.2	V	≥1.5
Device Voltage Variation vs. Temperature at 100mA			-3.6		mV/°C	
Device Voltage Variation vs Current at 25°C			3.3		mV/mA	
Thermal Resistance, junction-to-case <sup>1</sup>			64		°C/W	

\*Guaranteed specification DC-6 GHz. Low frequency cut off determined by external coupling capacitors.

### Absolute Maximum Ratings

Parameter	Ratings
Operating Temperature*	+45°C to 85°C
Storage Temperature	+85°C to 150°C
Operating Current	160mA
Power Dissipation	1W
Input Power	13 dBm

Note: Permanent damage may occur if any of these limits are exceeded.

These ratings are not intended for continuous normal operation.

<sup>1</sup>Case is defined as ground leads.

\*Based on typical case temperature rise 9°C above ambient.

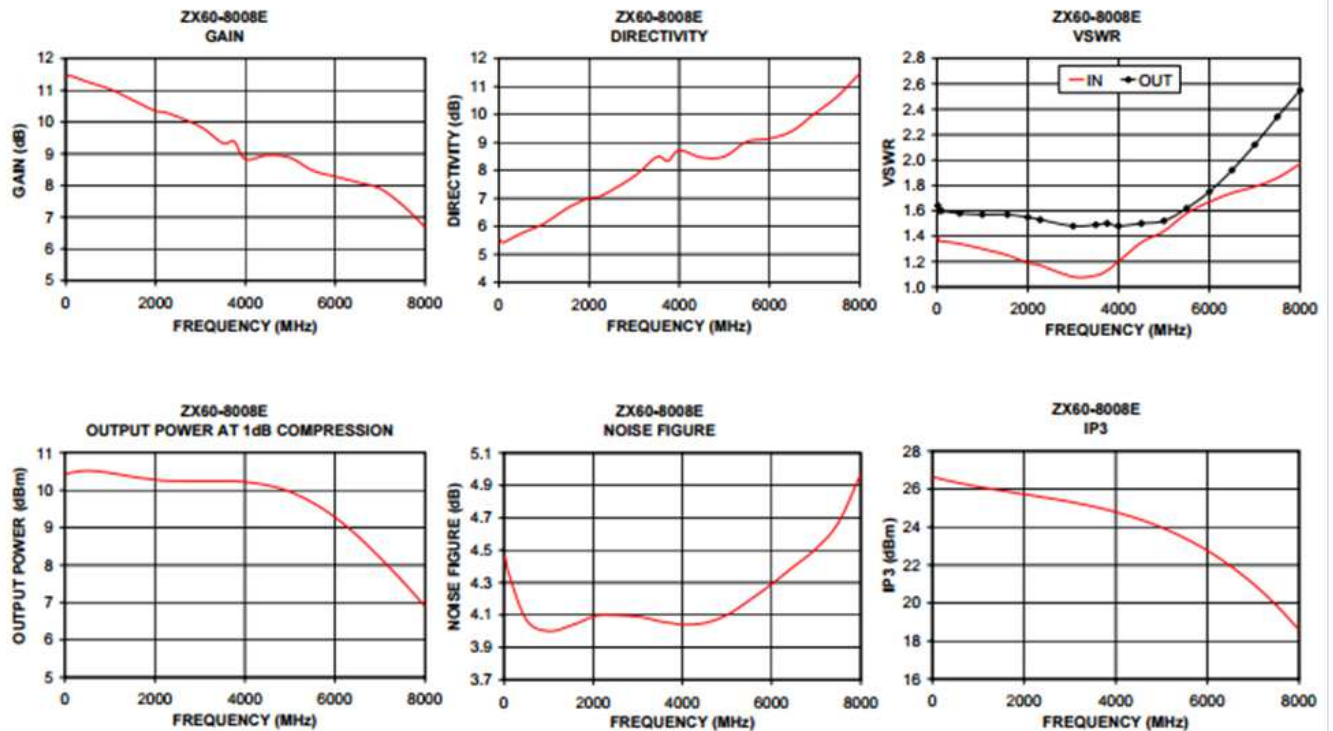
## A.3 PA: ZX60-8008E

Electrical Specifications at  $T_{AMB} = 25^{\circ}\text{C}$

MODEL NO.	FREQ. (GHz) $f_L - f_U$	DC VOLTAGE @ Pin V+ (V)	GAIN over frequency in GHz Typ (dB)								MAXIMUM POWER (dBm) Output (1 dB Comp.) Typ. $f_L - f_U$		DYNAMIC RANGE NF (dB) (dBm) Typ. IP3 (dBm) Typ.		VSWR (:1) Typ.				ACTIVE DIRECTIVITY (dB) Isolation-Gain Typ.	DC OPERATING CURRENT @ Pin V+ (mA) Typ. Max.		
			0.1	1.0	2.0	3.0	4.0	5.0	6.0	8.0	Min.at 2 GHz	8.4	10.8	6.6	4.1	24	$f_L - 3$ GHz	$3 - f_U$ GHz		$f_L - 3$ GHz	$3 - f_U$ GHz	Typ.
ZX60-8008E(*)	0.02-8	12.0	11.5	11.1	10.4	9.9	9.0	9.0	8.5	7.0	8.4	10.8	6.6	4.1	24	1.3	1.5	1.6	1.9	6-11	39	50

### Maximum Ratings

Operating Temperature	-45°C to 80°C case
Storage Temperature	-55°C to 100°C
DC Voltage	12.5V
Input Power(no Damage)	15dBm
Power	650mW



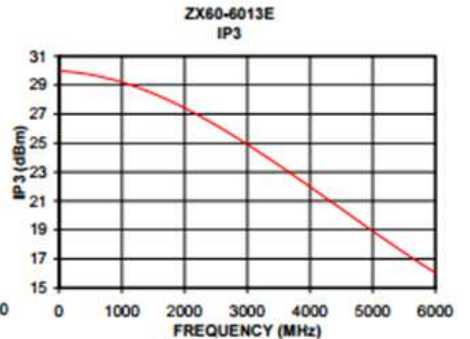
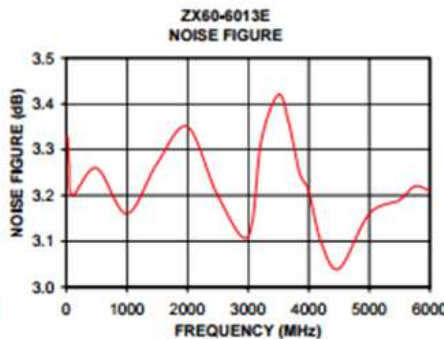
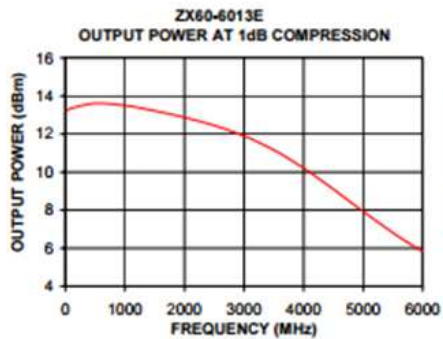
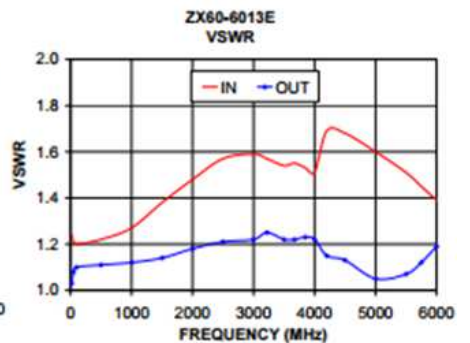
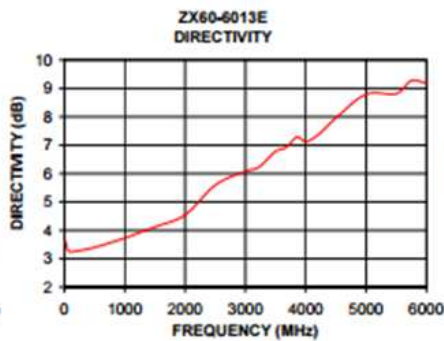
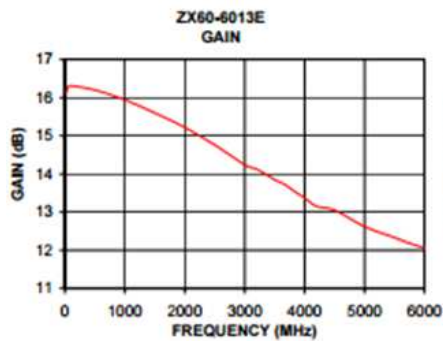
## A.4 LNA: ZX60-6013E

Electrical Specifications at  $T_{AMB} = 25^{\circ}\text{C}$

MODEL NO.	FREQ. (GHz) $f_c - f_u$	DC VOLTAGE @ Pin V+ (V)	GAIN over frequency in GHz Typ (dB)								MAXIMUM POWER (dBm) Output (1 dB Comp.) Typ. $f_c$ $f_u$	DYNAMIC RANGE		VSWR (:1) Typ.				ACTIVE DIRECTIVITY (dB) Isolation-Gain Typ.	DC OPERATING CURRENT @ Pin V+ (mA)		
			0.1	1.0	2.0	3.0	4.0	5.0	6.0	Min. at 2 GHz		NF (dB) Typ.	IP3 (dBm) Typ.	$f_c - 3$ GHz	$3 - f_u$ GHz	$f_c - 3$ GHz	$3 - f_u$ GHz		Typ.	Typ.	Max.
ZX60-6013E(+)	0.02-6	12.0	16.2	15.9	15.2	14.3	13.4	12.7	12.1	13.0	13.4	5.8	3.3	28.7	1.4	1.6	1.2	1.2	3-9	39	50

### Maximum Ratings

Operating Temperature	-45°C to 85°C
Storage Temperature	-55°C to 100°C
DC Voltage	12.5V
Input Power(no Damage)	15dBm
Power	650mW



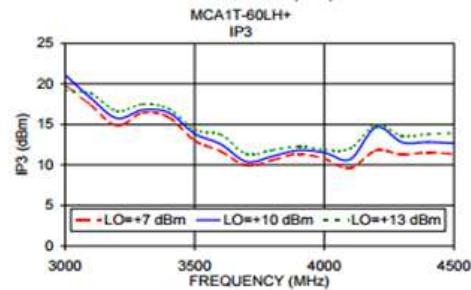
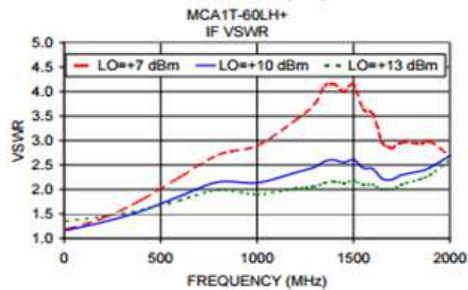
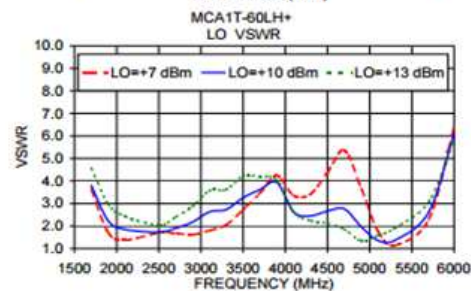
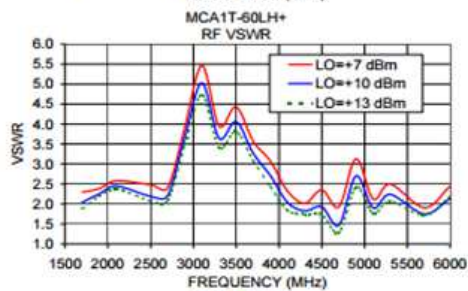
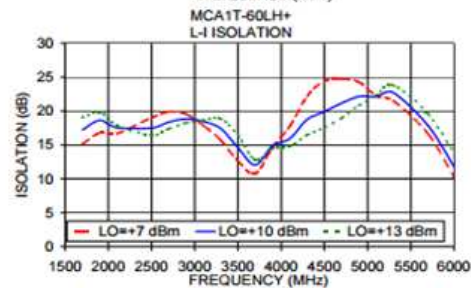
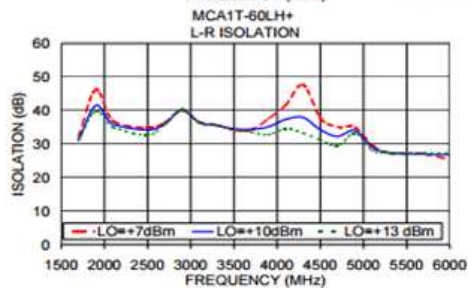
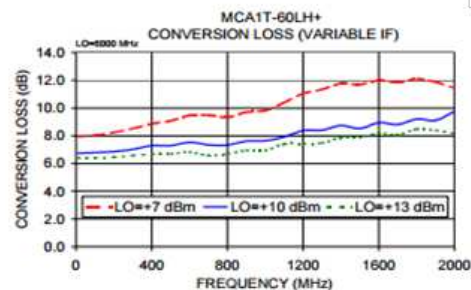
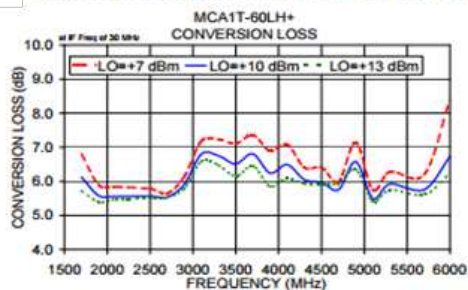
## A.5 MIX: MCA1T-60LH

Electrical Specifications ( $T_{AMB} = -40^{\circ}\text{C}$  to  $85^{\circ}\text{C}$ )

FREQUENCY (MHz)		CONVERSION LOSS (dB)			LO-RF ISOLATION (dB)		LO-IF ISOLATION (dB)		IP3 at center band (dBm)
LO/RF	IF	$\bar{X}$	$\sigma$	Max.	Typ.	Min.	Typ.	Min.	Typ.
1700-4400	DC-2000	6.6	0.1	7.9*	35	23	17	—	13
4400-6000	DC-2000	6.0	0.1	8.3*	27	20	21	—	11

1 dB COMPR. +5 dBm typ.

\*Conversion loss at 30 MHz IF, increases with IF frequency. See Graphs



### Pin Connections

LO	10
RF	5
IF	3
GROUND	1,2,4,6,7,8,9

### Maximum Ratings

Operating Temperature	-40°C to 85°C
Storage Temperature	-40°C to 85°C
RF Power	50 mW
IF Current	40 mA

Permanent damage may occur if any of these limits are exceeded.

## A.6 ADC: USB-6351

### Analog Input

Number of channels	8 differential or 16 single ended
ADC resolution	16 bits
DNL	No missing codes guaranteed
INL	Refer to the <i>AI Absolute Accuracy</i> section.
Sample rate	
Single channel maximum	1.25 MS/s
Multichannel maximum (aggregate)	1.00 MS/s
Minimum	No minimum
Timing resolution	10 ns
Timing accuracy	50 ppm of sample rate
Input coupling	DC
Input range	$\pm 0.1$ V, $\pm 0.2$ V, $\pm 0.5$ V, $\pm 1$ V, $\pm 2$ V, $\pm 5$ V, $\pm 10$ V
Maximum working voltage for analog inputs (signal + common mode)	$\pm 11$ V of AI GND
CMRR (DC to 60 Hz)	100 dB
Input impedance	
Device on	
AI+ to AI GND	$>10$ G $\Omega$ in parallel with 100 pF
AI- to AI GND	$>10$ G $\Omega$ in parallel with 100 pF
Device off	
AI+ to AI GND	820 $\Omega$
AI- to AI GND	820 $\Omega$
Input bias current	$\pm 100$ pA
Crosstalk (at 100 kHz)	
Adjacent channels	-75 dB
Non-adjacent channels	-95 dB
Small signal bandwidth (-3 dB)	1.7 MHz
Input FIFO size	2,047 samples
Scan list memory	4,095 entries
Data transfers	
PCIe	DMA (scatter-gather), programmed I/O
USB	USB Signal Stream, programmed I/O
Overvoltage protection for all analog input and sense channels	
Device on	$\pm 25$ V for up to two AI pins
Device off	$\pm 15$ V for up to two AI pins
Input current during overvoltage condition	$\pm 20$ mA max/AI pin